UNIVERSITY OF CALIFORNIA

Santa Barbara

Stabilized sources in Visible for Atomic, Molecular and Quantum applications

A dissertation submitted in partial satisfaction of the

requirements for the degree Doctor of Philosophy

in Electrical and Computer Engineering

by

Nitesh Chauhan

Committee in charge:

Professor Daniel J. Blumenthal, Chair

Professor Steven P. DenBaars

Professor Galan Moody

Professor Ryan Behunin

March 2024

The dissertation of Nitesh Chauhan is approved.

Steven P. DenBaars

Galan Moody

Ryan Behunin

Daniel J. Blumenthal, Committee Chair

December 2023

Stabilized sources in Visible for Atomic, Molecular and Quantum applications

by

Nitesh Chauhan

ACKNOWLEDGEMENTS

This thesis, which bears my name, has only been made possible by the contributions and guidance of several people throughout my PhD journey, up to the writing of this thesis. This section extends my humble acknowledgement to everyone without whom this thesis would not have been possible.

First, I thank Professor Daniel J. Blumenthal for accepting me in his group and advising, guiding, and motivating me all these years to work on innovative photonic research. His systematic research methodology, dedication to highest-quality work, excellent problem-solving, and management capabilities shaped me not only as a researcher but also as an individual. Professor Blumenthal's vision and foresight identifying the massive impact that photonics can have on atomic and ion-based systems and bringing together the fields of innovative photonics and atomic physics made this thesis possible. I am also thankful to Professor Blumenthal for teaching me how to draft research literature and for the massive time and energy that he dedicated to going over and helping us prepare for publications. I would also like to thank my committee member Prof. Ryan Behunin for his amazing theoretical framework, valuable multiphysics simulations, and advice regarding the setups. I would also like to thank the other committee members, Prof. Steven DenBaars and Prof. Galan Moody, for their helpful advice, discussion, and support.

This thesis would not have been possible without collaborations with multiple research groups and industry which includes Professor Ryan Behunin and Peter Rakich for SBS and coilR discussions, Prof Robert Niffenegger for continued collaboration of implementing our photonic devices with a Sr ion, Prof Jun Ye for implementation of visible stabilized sources for neutral Sr clock. For the industry collaborations I would like to acknowledge support over the years from Dr Karl Nelson from Honeywell for helping with Rb large area gratings and continues support for CMOS fabrication, Matthew Puckett form Honeywell for grating designs, Dr Chad Fertig and Dr Chad Hoyt from Honeywell for useful discussions for early visible SBS discussions, Dr Chris Wood and others from Inflexion for help with building our Rb MOT and useful advice, Dr Mary Rowe and team from Quantinuum for help with testing the 493 nm devices.

At UCSB various people helped and inspired the work. In particular, our OCPI group has provided an excellent collaborative environment in which ideas flow and are freely shared, and everyone is available for support or discussion whenever needed. I would like to thank previous group members Sarat Gundavarapu, Taran Hoffmann and Michael Belt for teaching me general lab experimentation skills for photonics, mask layout and simulations, Grant Brodnik for help and guiding through my first PDH locks and Renan Moreira for useful discussions. I would like to thank current students, Jiawei Wang for his immense help with fabrication of majority of non CMOS devices in this thesis, Debapam Bose for grating fabrication, Andrei Isichenko for bringing our code base from stone age to 21st century, Mark Harrington for discussions on nuances of PDH locks and general help in lab, Kaikai Liu for mask layout, locking and simulation discussions. Outside the group, I am grateful to Akshar Jain, Craig Hollman and Ian Hedgepeth who have helped at various durations during my PhD and all the friends in UCSB and outside UCSB.

Finally, I would extend my gratitude to my parents and sister for always being a pillar of support, encouraging my passions from an early age, and letting me choose my own path for my career in something that I love. It is impossible to acknowledge their contribution in the limited work here, so I would like to dedicate this dissertation to them humbly.

Dedicated to my parents Sanjay Pal Singh Chauhan, Anshu, and my sister

Nupur Chauhan

VITA OF NITESH CHAUAHN
December 2023

EDUCATION

Bachelor of Technology in Electrical Engineering, Indian Institute of Technology, Indore, India, May 2016
Master of Science in Electrical and Computer Engineering, University of California, Santa Barbara, June 2018
Doctor of Philosophy in Electrical and Computer Engineering, University of California, Santa Barbara, December 2023 (expected)

PROFESSIONAL EMPLOYMENT
Graduate Student Researcher, Electrical and Computer Engineering, University of California, Santa Barbara,

PUBLICATIONS

- Isichenko, **N. Chauhan**, J. Wang, D. Bose, K. Liu, M. W. Harrington, and D. J. Blumenthal, "Photonic integrated building-blocks for rubidium cold atom systems," in *2023 IEEE Photonics Society Summer Topicals Meeting Series (SUM)* (2023), pp. 1–2.
- Isichenko, **N. Chauhan**, K. Liu, M. W. Harrington, and D. J. Blumenthal, "Chip-Scale, Sub-Hz Fundamental Sub-kHz Integral Linewidth 780 nm Laser through Self- Injection-Locking a Fabry-Pérot laser to an Ultra-High Q Integrated Resonator," *arXiv* 2307.04947 (n.d.).
- K. Liu, J. Wang, **N. Chauhan**, and D. J. Blumenthal, "Circulator-free photonic integrated Brillouin laser," in *Optica Nonlinear Optics Topical Meeting 2023 (2023),* Paper Tu2A.3 (Optica Publishing Group, 2023), p. Tu2A.3.
- D. J. Blumenthal, **N. Chauhan**, A. Isichenko, J. Wang, D. Bose, K. Liu, and M. W. Harrington, "Visible Light Photonics for Atomic and Quantum Sensing and Computation," in *Optica Quantum 2.0 Conference and Exhibition (2023), Paper QTu4C.1* (Optica Publishing Group, 2023), p. QTu4C.1.
- Isichenko, **N. Chauhan**, D. Bose, J. Wang, P. D. Kunz, and D. J. Blumenthal, "Photonic integrated beam delivery for a rubidium 3D magneto-optical trap," *Nat Communications* **14**, 3080 (2023).
- **N. Chauhan**, A. Isichenko, K. Liu, and D. J. Blumenthal, "Visible 780 nm SBS laser with mW level threshold in an ultra-high 145 million Q integrated waveguide resonator," in *CLEO 2023 (2023),* Paper SF1K.*6* (Optica Publishing Group, 2023), p. SF1K.6.
- K. Liu, J. Wang, A. Isichenko, **N. Chauhan**, and D. J. Blumenthal, "Integrated High-Extinction-Ratio 2.0-Meter Unbalanced MZI for Laser Frequency Noise Measurements," in *CLEO 2023 (2023),* Paper STu4P.5 (Optica Publishing Group, 2023), p. STu4P.5.
- A. Isichenko, **N. Chauhan**, J. Wang, M. W. Harrington, K. Liu, and D. J. Blumenthal, "Tunable Integrated 118 million Q Reference Cavity for 780 nm Laser Stabilization and

Rubidium Spectroscopy," in *CLEO 2023 (2023),* Paper SF3K.4 (Optica Publishing Group, 2023), p. SF3K.4.

- D. J. Blumenthal, **N. Chauhan**, A., Isichenko, K., Liu, J. Wang, "Integrated stabilized lasers and circuits for atom cooling, trapping, and interrogation," in *Quantum Sensing, Imaging, and Precision Metrology*, S. M. Shahriar and J. Scheuer, eds. (SPIE, 2023), p. 71.
- **N. Chauhan**, A. Isichenko, J. Wang, and D. J. Blumenthal, "Sub-dB/m loss integrated 103 and 90 million Q resonators for laser stabilization at rubidium and strontium wavelengths," *2022 IEEE Photonics Conference (IPC),* p. MG4.3, (n.d.).
- **N. Chauhan**, K. Liu, A. Isichenko, J. Wang, H. Timmers, and D. J. Blumenthal, "Integrated 3.0 meter coil resonator for λ = 674 nm laser stabilization," *Conference on Frontiers in Optics and Laser Sciences,* FM1E.1, (n.d.).
- K. Liu, J. H. Dallyn, G. M. Brodnik, A. Isichenko, M. W. Harrington, **N. Chauhan**, D. Bose, P. A. Morton, S. B. Papp, R. O. Behunin, and D. J. Blumenthal, "Photonic circuits for laser stabilization with integrated ultra-high Q and Brillouin laser resonators," *APL Photonics* **7**, 096104 (2022).
- K. Liu, **N. Chauhan**, J. Wang, A. Isichenko, G. M. Brodnik, P. A. Morton, R. O. Behunin, R. O. Behunin, S. B. Papp, S. B. Papp, and D. J. Blumenthal, "36 Hz integral linewidth laser based on a photonic integrated 4.0 m coil resonator," *Optica, OPTICA* **9**, 770–775 (2022).
- A. Isichenko, **N. Chauhan**, D. Bose, P. D. Kunz, and D. J. Blumenthal, "Cooling rubidium atoms with a photonic integrated 3D magneto-optical trap," in *Optical Sensors and Sensing Congress 2022 (AIS, LACSEA, Sensors, ES) (2022),* Paper STu4G.6 (Optica Publishing Group, 2022), p. STu4G.6.
- K. Liu, N. Jin, H. Cheng, **N. Chauhan**, M. W. Puckett, K. D. Nelson, R. O. Behunin, R. O. Behunin, P. T. Rakich, and D. J. Blumenthal, "Ultralow 0.034 dB/m loss wafer-scale integrated photonics realizing 720 million Q and 380 μW threshold Brillouin lasing," *Opt. Lett., OL* **47**, 1855–1858 (2022).
- K. Liu, **N. Chauhan**, J. Wang, A. Isichenko, G. M. Brodnik, P. A. Morton, R. Behunin, S. B. Papp, and D. J. Blumenthal, "Semiconductor laser stabilized by a photonic integrated 4 meter coil-waveguide resonator," in *Optical Fiber Communication Conference (OFC) 2022 (2022),* Paper Tu3D.2 (Optica Publishing Group, 2022), p. Tu3D.2.
- **N. Chauhan**, J. Wang, D. Bose, K. Liu, R. L. Compton, C. Fertig, C. W. Hoyt, and D. J. Blumenthal, "Ultra-low loss visible light waveguides for integrated atomic, molecular, and quantum photonics," *Opt. Express*, OE **30**, 6960–6969 (2022).
- K. Liu, **N. Chauhan**, J. Wang, P. A. Morton, R. Behunin, and D. J. Blumenthal, "Precision Laser Stabilization using Photonic Integrated Coil Resonator," in *Frontiers in Optics + Laser Science 2021 (2021),* Paper FTh2A.1 (Optica Publishing Group, 2021), p. FTh2A.1.
- **N. Chauhan**, A. Isichenko, K. Liu, J. Wang, Q. Zhao, R. O. Behunin, P. T. Rakich, A. M. Jayich, C. Fertig, C. W. Hoyt, and D. J. Blumenthal, "Visible light photonic integrated Brillouin laser," *Nature Communication* 12, 4685 (2021).
- K. Liu, M. W. Puckett, M. W. Harrington, G. M. Brodnik, Q. Zhao, **N. Chauhan**, J. Wang, R. O. Behunin, K. D. Nelson, and D. J. Blumenthal, "Milliwatt Threshold Ultra-Low

Linewidth Photonic Integrated Si3N4 Brillouin Laser," in *Conference on Lasers and Electro-Optics (2021),* Paper SF2O.1 (Optica Publishing Group, 2021), p. SF2O.1.

- M. W. Puckett, K. Liu, **N. Chauhan**, Q. Zhao, N. Jin, H. Cheng, J. Wu, R. O. Behunin, P. T. Rakich, K. D. Nelson, and D. J. Blumenthal, "422 million intrinsic quality factor planar integrated all-waveguide resonator with sub-MHz linewidth," *Nature Communications* 12, 934 (2021).
- Q. Zhao, R. O. Behunin, P. T. Rakich, **N. Chauhan**, A. Isichenko, J. Wang, C. Hoyt, C. Fertig, M. Hong Lin, and D. J. Blumenthal, "Low-loss low thermo-optic coefficient Ta2O5 on crystal quartz planar optical waveguides," *APL Photonics* 5, 116103 (2020).
- **N. Chauhan**, D. Bose, M. Straus, C. A. Holliman, A. M. Jayich, R. O. Behunin, R. O. Behunin, and D. J. Blumenthal, "Evidence of visible wavelength spontaneous Brillouin scattering in Si3N4 waveguides," in *Frontiers in Optics / Laser Science (2020),* Paper FW1D.5 (Optical Society of America, 2020).
- **N. Chauhan**, J. Wang, D. Bose, R. Moreira, and D. J. Blumenthal, "Ultra-Low Loss 698 nm and 450 nm Silicon Nitride Visible Wavelength Waveguides for Strontium Atomic Clock Applications," in *Conference on Lasers and Electro-Optics* (OSA, 2020), p. STh1J.2.
- Q. Zhao, J. Wang, **N. Chauhan**, D. Bose, N. Jin, R. Moreira, R. Behunin, P. Rakich, and D. Blumenthal, "Low-loss D-shape Silicon Nitride Waveguides Using a Dielectric Lift-off Fabrication Process," in *Conference on Lasers and Electro-Optics (2020),* Paper STh1J.3 (Optical Society of America, 2020), p. STh1J.3.
- **N. Chauhan**, D. Bose, M. Puckett, R. Moreira, K. Nelson, and D. J. Blumenthal, "Photonic Integrated Si3N4 Ultra-Large-Area Grating Waveguide MOT Interface for 3D Atomic Clock Laser Cooling," in *Conference on Lasers and Electro-Optics (2019),* Paper STu4O.3 (Optical Society of America, 2019), p. STu4O.3.
- S. Gundavarapu, G. M. Brodnik, M. Puckett, T. Huffman, D. Bose, R. Behunin, J. Wu, T. Qiu, C. Pinho, **N. Chauhan**, J. Nohava, P. T. Rakich, K. D. Nelson, M. Salit, and D. J. Blumenthal, "Sub-hertz fundamental linewidth photonic integrated Brillouin laser," *Nature Photonics* 13, 60–67 (2019).
- **N. Chauhan**, M. Soni, V. Anand, and V. Kanhangad, "Fingerprint classification using crease features," in *2016 IEEE Students' Technology Symposium (TechSym)* (2016), pp. 56–60.
- A. K. Upadhyay, **N. Chauhan**, and S. K. Vishvakarma, "A Compact Electrical Modelling for Top-Gated Doped Graphene Field-Effect Transistor," *IETE Journal of Research* 64, 317–323 (2018).

AWARDS AND HONORS

- Paper: **N. Chauhan**, et. Al., "Ultra-low loss visible light waveguides for integrated atomic, molecular, and quantum photonics," Opt. Express, OE **30**, 6960–6969 (2022) selected **editors' pick.**

- Paper: K. Liu, **N. Chauhan**, et. Al., "36 Hz integral linewidth laser based on a photonic integrated 4.0 m coil resonator," Optica, OPTICA **9**, 770–775 (2022) was one of the **most viewed** of the month.
- Co-authored paper: S. Gundavarapu, G. M. Brodnik, M. Puckett, T. Huffman, D. Bose, R. Behunin, J. Wu, T. Qiu, C. Pinho, **N. Chauhan**, J. Nohava, P. T. Rakich, K. D. Nelson, M. Salit, and D. J. Blumenthal, "Sub-hertz fundamental linewidth photonic integrated Brillouin laser," Nature Photonics **13**, 60–67 (2019) on the **cover of Nature Photonics.**
- Co-authored paper: Q. Zhao, R. O. Behunin, P. T. Rakich, **N. Chauhan**, A. Isichenko, J. Wang, C. Hoyt, C. Fertig, M. Hong Lin, and D. J. Blumenthal, "Low-loss low thermo-optic coefficient Ta2O5 on crystal quartz planar optical waveguides," APL Photonics **5**, 116103 (2020) selected for **editor's pick.**
- Conference proceeding **N. Chauhan**, M. Soni, V. Anand, and V. Kanhangad, "Fingerprint classification using crease features," in *2016 IEEE Students' Technology Symposium (TechSym)* (2016), pp. 56–60, awarded **the Best Paper Award** in the Field**.**
- Certificate for **academic excellence** in year 2012-2013 in IIT Indore.

ABSTRACT

Stabilized sources in Visible for Atomic, Molecular and Quantum applications

By

Nitesh Chauhan

Visible and near-IR low-phase-noise lasers, laser stabilization cavities, and beam manipulation optics are integral components of atomic, ion, and quantum systems. These systems require low-frequency noise at specific frequency offsets, dictated by the applications for trapping, preparation, and manipulation of the atomic and qubit states. Today, these low-noise sources are provided by tabletop lasers locked to the bulk stabilization cavities. Bulk free-space optics are used to route, modulate, and manipulate the necessary beams to realize these systems. The miniaturization and development of portable atomic and quantum systems will benefit from integrated photonic systems for reducing the size, weight, and power budget consumption (SWaP), as well as improving the new low-frequency noise of direct-drive sources at the required transition wavelengths of atoms, ions, and molecules, and potentially improving the performance and sensitivity of these experiments.

Progress towards low loss waveguides and precision lasers at visible wavelengths has been limited because of the high loss introduced by significant scattering in visible waveguides where the loss scales as $1/\lambda^4$. This work demonstrates the lowest waveguide losses at visible and near-IR wavelengths achieved to date by using a dilute mode, weakly confined Si_3N_4 waveguide design fabricated using a CMOS foundry compatible process. This platform offers a wide transparency window of 405 nm – 2350 nm. The demonstrated losses

are 2 dB/m at λ = 493 nm, 0.6 dB/m at λ = 674 nm – 698 nm and 0.36 dB at λ = 789 nm with the highest quality factors (Q) demonstrated to date in visible at 39 million at 493 nm, 90 million at 674 nm and 100 million at 698 nm and 145 million at 780 nm. These losses are summarized in Figure 2.1 and compared with other published state-of-the-art waveguide losses. To achieve these losses using dilute modes, the absorption in both the silicon nitride core and the oxide cladding must be minimized, and nitride sidewall scattering must be reduced.

The low loss and high-Q of the Si_3N_4 resonators in Si_3N_4 enable high precision lasers that utilize the high-Q resonator cavity as to realize a low-phase-noise active laser cavity for mid- to high-offset frequencies and either as an external passive cavity for the reduction of low-frequency phase noise and improved carrier stability or a passive nonlinear cavity for improving high-offset frequency noise. Various metrics are used to characterize the phase or frequency noise of lasers, including fundamental linewidth (FLW), integral linewidth (ILW), and Allan Deviation (ADEV), as discussed in detail in this dissertation. The FLW is due to quantum-driven phase fluctuations (memoryless white noise process) that play a role at high-frequencies, define the ILW and shape the wings of the laser linewidth. The technical noise sources due to both fundamental and environmental fluctuations build up the time-averaged broadened shape, the ILW, and contribute to low-frequency noise, such as flicker noise and fractional frequency noise. Finally, at the longest time intervals, the carrier or line-shape exhibits a long-term drift. These are discussed in detail in Section 1.3. This dissertation focuses on the minimization of these frequency noise contributions and drift over wide ranges of offset frequencies, and various linewidth definitions are employed to summarize the frequency noise characteristics.

This work demonstrates integrated stimulated Brillouin scattering (SBS) lasers [1,2] operating in the visible and near-IR regions for the first time. These demonstrations are at key atomic optical transitions: 674 nm for the $^{88}Sr^{+}$ clock and qubit optical transition, 698 nm for the ^{87}Sr clock transition, and 778/780 nm for the ^{87}Rb two-photon clock and Rydberg applications. These lasers have a 10/6 mW threshold for 674/698 nm and a 0.8 mW threshold at 780 nm wavelength and achieve a factor of 500x - 3500x reduction in fundamental linewidth with a 12 Hz fundamental linewidth at 674 nm, a 7.8 Hz fundamental linewidth at 698 nm, and an 18 Hz fundamental linewidth at 780 nm along with 2-10x reduction in integral linewidth.

To further reduce the integral linewidth of the lasers, we designed and realized integrated stabilization cavity is demonstrated in the form of CMOS foundry-compatible coil resonator (coilR) that operate at visible wavelengths. These coil resonators were 3 m long length on the resonator to establish a low thermo-refractive noise (TRN) [3] floor. Pound-Drever-Hall (PDH) locking [4,5] is a widely used technique to enable the laser to take on the frequency noise properties of an optical reference cavity and is discussed further in Section 1.3 of this dissertation. By locking the SBS laser to these integrated coil cavities, the integral linewidth is further reduced in addition to the fundamental linewidth reduction by the SBS laser. Direct locking of lasers in general (SBS, semiconductor, or any other laser design) to these coilR-integrated stabilization cavities achieves a 2-4 orders of magnitude reduction in frequency noise for frequencies in the lock loop bandwidth and a ~ 20x reduction in integral linewidth at 674 nm. Moreover, these coilRs operate over a wide wavelength range of 670 – 700 nm while maintaining a high Q value, which is required for low noise and strong frequency discrimination.

This dissertation also describes demonstration of these direct drive, stable low phase noise sources in actual atomic systems. The 674 nm coil resonators is used as a stabilization cavity for a 674 nm laser to address a collaborator's $^{88}Sr^{+}$ ion trap [6], enabling key measurements and functions, such as ion spectroscopy, drift measurement, state preparation, rabi oscillations, and Ramsey interferometry, with the use of a traditional tabletop optical reference cavity.

Cold-atom systems use a cloud of atoms or a chain of ions that are cooled and trapped by laser beams along with a magnetic field. These will benefit from integrated photonics is beam delivery and beam shaping for various operations, such as the large-area cooling and trapping beams required for a neutral atom cooling and trapping in a 3D magneto optic trap (MOT). This work demonstrates the largest waveguide emitted beams from photonic waveguide platform, with beam size of 2.5 mm x 3.5 mm flat top beams which represent a 20 million times increase in area over a waveguide mode. Three beams at 54.7 °from the chip normal placed 120 °from each other provided three orthogonally intersecting beams that provided the correct orientation to form an MOT at ~1 cm above the chip surface. The 780 nm gratings were utilized to demonstrate the cooling of over a million ^{87}Rb atoms in a 3D MOT.

TABLE OF CONTENTS

LIST OF FIGURES

LIST OF TABLES

Chapter 1: Introduction to integrated stable sources

1.1 Introduction

Visible and near infrared (IR) narrow linewidth lasers, stabilization cavities, beam manipulation optics, and passive visible components are integral parts of cold atom, ion, and quantum systems [10–14]. These systems require multiple wavelengths that are matched to transitions for specific atomic species for various operations, such as cooling, trapping, repumping, state preparation, readout, and qubit manipulation [15–17]. The wavelengths used in these operations have different frequency noise and linewidth requirements; for example, broad transitions only require kHz or MHz linewidths for spectroscopic locking to the transitions, while simultaneously requiring multiple components for beam splitting, polarization manipulation, modulation, isolation, and setting the beam size and profile. Other optical atomic transitions require low-frequency noise for functions such as state preparation, manipulation, and clock or qubit operations [13,15]. Highly coherent lasers are required for interrogation of atomic transitions to maintain the strong visibility of Rabi flopping [18] or Ramsey interferometry [19], and such measurements are often limited by the coherence of the interrogation lasers [19]. Today, these low noise lasers are provided by tabletop lasers locked to bulk stabilization cavities [20–22]. Moreover, bulk free space optics are used to manipulate and deliver the necessary beams to these atomic systems. The miniaturization, development of portable systems, and improved reliability and scalability will benefit from photonic integration for reducing the size, weight, and power budget (SWaP) and providing modularity, which will ease upgrading specific tasks without bringing down the entire system and enable

more complex, large-scale experiments. Dense photonic integration will also enable new physics by providing a narrow tailorable frequency noise at the required interrogation frequency in a compact system.

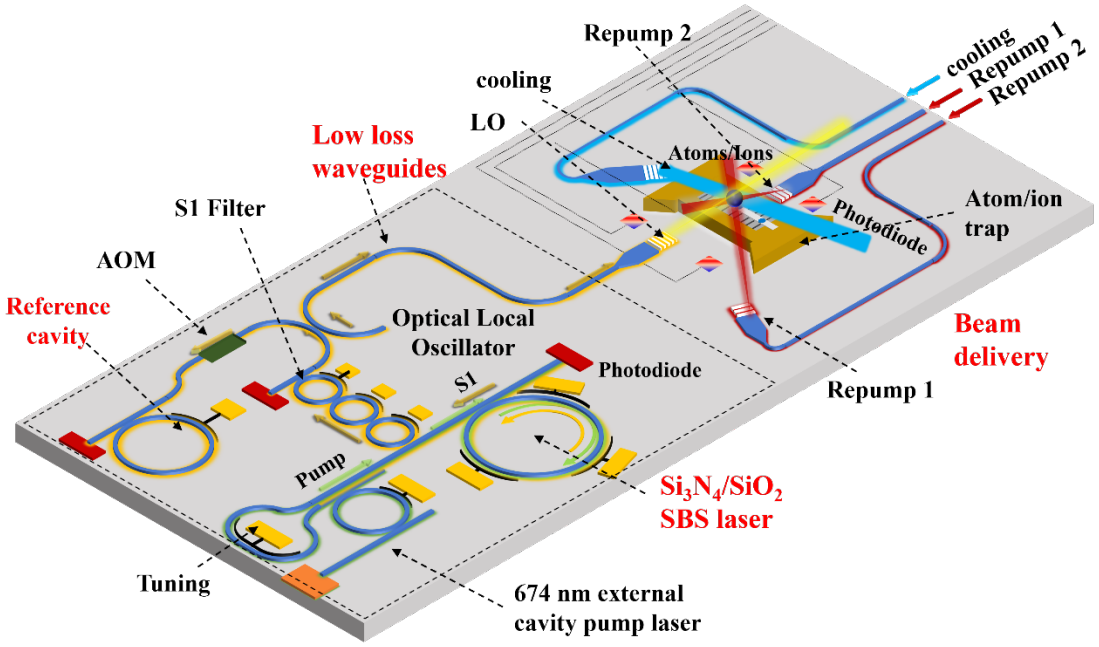

Figure 1.1 Vision of fully integrated trapped ion system: Integrated atom or ion system showing some of the necessary components that will benefit from integration towards a local oscillator (LO) chip providing stabilized source and gratings for beam delivery to the atoms. The components developed for this integrated system in this study are highlighted in red.

Progress towards stabilized integrated sources in the visible wavelengths has been slow, primarily owing to the requirement for very low-loss waveguides and high quality factor (Q) resonators which have been limited because of the high loss from scattering in visible waveguides, where the loss scales as $1/\lambda^4$. In this work, the lowest waveguide losses achieved to date are demonstrated using a weakly confined Si_3N_4 waveguide design in a complementary metal oxide semiconductor (CMOS) foundry compatible fabrication process [11]. This platform offers a wide transparency window of 405 – 2350 nm [10]. High quality factor (Q)

resonators at visible using the weakly confined Si_3N_4 waveguide are also designed in visible for on chip stable laser sources. As such, losses of 2 dB/m at $\lambda = 493$ nm, 0.6 dB/m at $\lambda = 674$ nm and 698 nm and 0.35 dB/m at $\lambda = 780$ nm, with the highest Q factors of 20 million at 493 nm, 90 million at 674nm, 100 million at 698 nm and 145 million at 780 nm are reported. Figure 1.2 below shows a comparison of losses and Qs from this work with the state of the art losses and Qs from the literature at visible wavelengths.

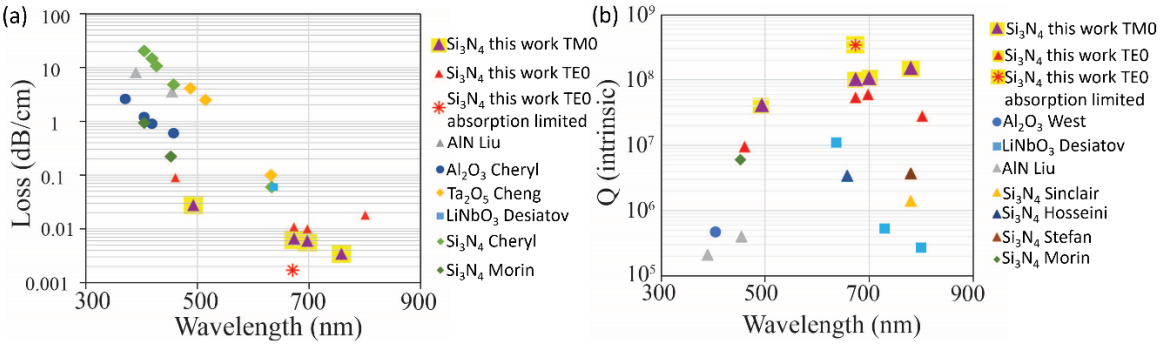

Figure 1.2 Literature Loss and Q comparison: (a) Comparison of losses of our Si_3N_4 waveguides with other state of the art waveguide losses in visible: AlN Liu [25], Al_2O_3 Cheryl [26], $LiNbO_3$ Desiatov [27], Si_3N_4 Cheryl [26], Si_3N_4 Morin [28]. (b) Comparison of intrinsic Q factors of our resonators in visible with literature: Al_2O_3 West [29], $LiNbO_3$ Desiatov [27], AlN Liu [25], Si_3N_4 Sinclair [30], Si_3N_4 Stafan [31], Si_3N_4 Morin [28].

The low loss and high Q of the Si_3N_4 resonators in Si_3N_4 enable high precision lasers that utilize the high Q resonator cavity to realize a low phase noise active laser cavity for mid- to high-offset frequencies and either as an external passive cavity for the reduction of low-frequency phase noise and improved carrier stability or a passive nonlinear cavity for improving high-offset frequency noise. Various metrics are used to characterize the phase or frequency noise of lasers, including fundamental linewidth (FLW), integral linewidth (ILW), and Allan Deviation (ADEV), as discussed in detail in this dissertation. The FLW is due to quantum-driven phase fluctuations (memoryless white noise process) that play a role at high-

frequencies, define the ILW and shape the wings of the laser spectra. The technical noise sources due to both fundamental and environmental fluctuations build up the time-averaged broadened shape, the ILW, and contribute to low-frequency noise, such as flicker noise and fractional frequency noise. Finally, at the longest time intervals, the carrier or line-shape exhibits a long-term drift. This is discussed in detail in Section 1.3 of this chapter. This dissertation focuses on the minimization of these frequency noise contributions over wide ranges of offset frequencies, and various linewidth definitions are employed to summarize the frequency noise characteristics.

This work demonstrates stimulated Brillouin scattering (SBS) lasers at 674 nm for $^{88}Sr^{+}$ clock and qubit transition, at 698 nm for ^{87}Sr clock transition and 778/780 nm for ^{87}Rb two photon clock and Rydberg applications. These lasers have a 10 mW threshold at 674 nm, 6 mW threshold at 698 nm and 0.8 mW threshold at 780 nm wavelength, and demonstrate a factor of 500-3500x reduction in FLW with 12 Hz FLW at 674 nm, 7.8 Hz FLW at 698 nm, and 18 Hz FLW at 780 nm along with a ~2-10x reduction in integral linewidth.

To further reduce the ILW of the lasers, we designed and realized an integrated stabilization cavity in the form of a CMOS foundry-compatible coil resonator (coilR) that operates at visible wavelengths. These coil resonators were 3 m long and were designed to increase the total optical mode volume, thereby reducing the thermo-refractive noise (TRN) [3] floor, which is a fundamental thermal noise limit in stabilization cavities and scales inversely with the optical mode volume, as discussed in detail in Chapter 4. Pound-Drever-Hall (PDH) locking [4,5] is a widely used technique to enable the laser to take on the frequency noise properties of an optical reference cavity and is discussed further in Section 1.3 of this dissertation. By PDH locking the SBS laser to these integrated coil cavities, the

integral linewidth is further reduced, in addition to the fundamental linewidth reduction by the SBS laser. Direct locking of lasers in general (SBS, external cavity tunable laser, or any other laser design) to these coilR integrated stabilization cavities achieves a 2-4 orders of magnitude reduction in frequency noise for frequencies in the lock loop bandwidth and a ~ 20x reduction in integral linewidth at 674 nm. Moreover, these coilRs operate over a wide wavelength range of 670 – 700 nm while maintaining a high Q value, which is required for low noise and strong frequency discrimination.

This dissertation also describes demonstration of these direct drive, stable low phase noise sources in actual atomic systems. The 674 nm coil resonator is used as a stabilization cavity for a 674 nm laser to address the optical clock, or qubit transition in an $^{88}Sr^{+}$ ion trap [6] located in the Niffenegger Lab at University of Massachusetts at Amherst, enabling key measurements and functions such as ion spectroscopy, drift measurement, state preparation, rabi oscillations, and Ramsey interferometry, without the use of a traditional tabletop optical reference cavity [16].

There are two main types of atomics systems: 1. Cold atoms, where neutral atoms are cooled and trapped using optical beams, tweezers, and magnetic fields; and 2. Trapped ions, where neutral atoms are ionized with a laser, are trapped with radio frequency (RF) traps and further cooled and interrogated with optical beams. Photonic integration will benefit beam delivery and beam shaping for both cold neutral atoms and trapped ions, including various operations such as large-area cooling and trapping beams required for neutral atom cooling and trapping of a large number of atoms in a 3D magneto-optic trap (3D-MOT) [32]. This work demonstrates the largest waveguide to collimated emitted beams from a photonic waveguide platform, with beam size of 2.5 mm x 3.5 mm which represent a 20 million times

increase in area over the waveguide mode. Three beams at 54.7° from the chip-normal, placed 120° in-plane from each other, provided three orthogonally intersecting 3D-MOT cooling beams. The 780 nm gratings were utilized to demonstrate the cooling of over a million ^{87}Rb atoms in a 3D MOT.

1.2 Motivation for low loss waveguides

1.2.1 Spectroscopy, frequency metrology, computing, sensing, and quantum applications

An atom, ion, or molecule that is cooled and trapped in its motional ground state is a near-perfect harmonic oscillator. Species that have high Q transitions, that is, long lifetime states, offer a long interrogation of the harmonic oscillator and can be used to transfer the stability of the transition to a local oscillator (LO) [15] and act as a frequency standard. For frequency metrology, the measurement resolution depends on the species used as a measure of time. As a simple analogy, a ruler used for measuring length will have a higher resolution, the higher the number of divisions or ticks on the ruler, with the inaccuracy equal to one tick. Similarly, for an atomic clock that operates by counting time intervals, its resolution will increase with an increase in the number of ticks, that is, a higher carrier frequency. An LO stabilized to such trapped and cooled species provides some of the most stable frequency references and forms the basis for atomic clocks [22,33,34]; however, it needs to be stable itself so as not to limit the performance by its own noise.

Trapped and cooled species are extremely sensitive to external fields, such as electric, magnetic, and gravitational fields, and can be employed as some of the most sensitive sensors. These have been used for inertial sensing with atom interferometry [35], detection of gravitational redshift using clocks with a record fractional frequency uncertainty of 7.6 x 10^{-21} [22], and relative geodesy to map the gravitational potential of earth [36,37]. A space-based clock network can provide a test of fundamental constants, a test of the standard model of physics, and aid in the search for new physics [38,39]. However, this would require the development of compact and robust optical clocks, where each component, including stabilized lasers and beam manipulation and delivery, is compact and has low power consumption. Moreover, their absolute frequency stability makes their use as frequency references possible through spectroscopy [40] and would benefit from compact references for wider deployment.

Quantum computing requires highly coherent state preparation, logic gates, and measurements in a species in which a large ensemble of such states can be entangled and scaled for an increased number of qubits [16,41,42]. Ideally, these quantum computers have higher efficiency than their classical counterparts for certain tasks, but the loss of coherence from various noise sources, such as laser noise, causes them to lose their coherence and hence quantum nature. The five criteria outlined by DiVincenzo [43] are often used to determine the feasibility of a system for use as a quantum processor:

1. A physical system should have well-defined two-level states that can be isolated for use as qubits.
2. The system can be initialized into a well-defined and deterministic initial state.
3. The decoherence time for qubits should be much longer than the gate time.

4. A set of universal quantum gates can be applied to each qubit or pair of qubits for a single qubit and two qubit gates, respectively.
5. Qubits can be read with high accuracy.

Trapped ions and trapped neutral atoms are two of the leading platforms for implementing quantum gates [41,44–46], where motional sidebands can be used to entangle gates in ions and Rydberg circular states can be used to entangle gates in neutral atoms. Both implementations can either be implemented in Zeeman gates, which require stable lasers for implementing steps 2-5 from above, or optical gates using stabilized lasers as the LO, where a highly stable LO is desired to reduce the loss in fidelity from the LO.

1.2.2 Manipulation and interrogation of neutral and trapped atoms and ions

Systems using trapped and cooled ions, atoms, and molecules require several lasers with different wavelengths for various operations cooling (could be multiple stages) of species to a few μK, repumping (could be multiple stages) to ensure that the electrons are not trapped in unwanted states, state preparation (e.g., optical pumping), magic λ lattice trapping, tweezers, qubit manipulation, and fluorescence detection [15,16,41]. The availability of lasers for all the required transitions for the set of functions above for the desired application is one of the primary reasons for the selection of a species for the application. Another factor is the availability of a highly coherent long-lifetime transition for use as a clock/qubit transition. Alkali and Alkaline earth metal ion and atoms like Sr, Yb, Ca, Ba are often used species because of these properties [15]. Figure 1 shows the relevant energy diagram of a popular species for state-of-the-art qubits and atomic clocks: $^{88}Sr^{+}$ for qubit operations [45] and ^{87}Sr for optical lattice clocks [34]. The figure also shows the state lifetime/ Q of the transition,

which sets the coherence requirement to the first order of the laser used for exciting the transition. The presence of nearby electronic or motional states also requires noise spectra of the lasers used. A sequence of steps is typically involved in preparation and interrogation, where at each step, a laser with different wavelength is pulsed for operations such as cooling, repumping, state preparation, and interrogation. Aliasing effects originating from the use of pulsed operation also place a requirement on the noise spectra of the laser used, specifically the LO used, and this is known as the Dick effect [47].

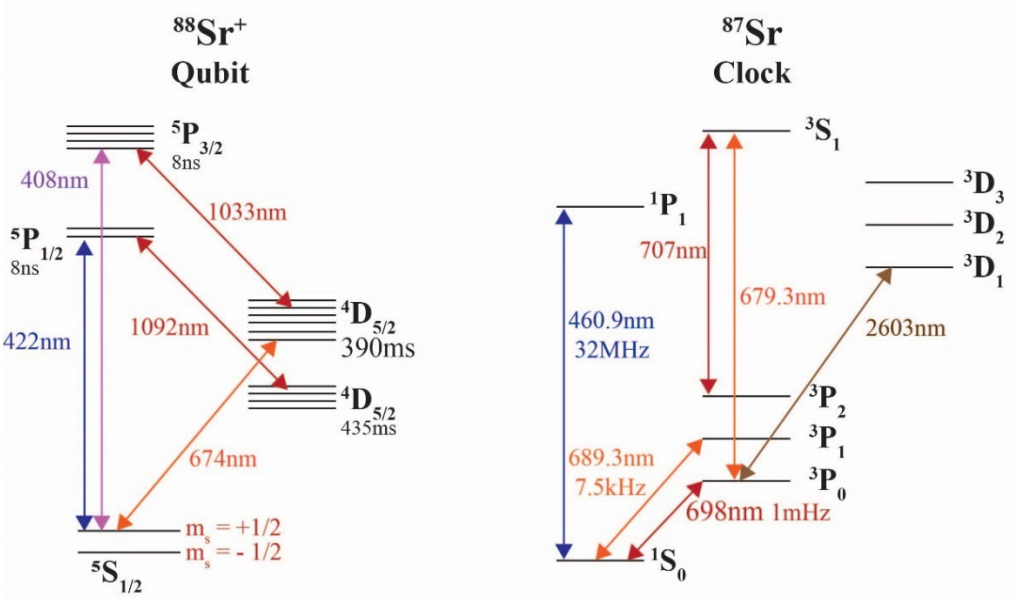

Figure 1.3 Energy level diagrams for $^{88}Sr^{+}$ qubit and ^{87}Sr clock: Relevant energy level diagrams with lifetime/linewidths of transitions.

Along with noise requirements, each wavelength also has different requirements for the beam profile, geometry, polarization, and alignment. Free-space bulk optics are commonly used for routing, beam shaping, polarization correction, alignment, and detection. Power-hungry free-space active components, such as acousto-optic modulators (AOMs) for locking, frequency shifting, and high extinction gating, are needed along with complex control and

radio frequency (RF) circuits for implementing the control sequence, locking, etc. All of these require manual alignment, making the system setup complex, large footprint, and typically occupying tabletops. This limits the scalability of qubits and confines such systems to laboratory environments. Many of these functions can be improved in terms of scalability, power consumption, and ease of alignment using waveguide-based photonic integrated circuits. Scaling to a greater number of qubits would also require modular systems with multiple functionalities integrated on a monolithic chip, as this approach has been immensely successful with traditional semiconductor computing and would require multilayer CMOS foundry compatible waveguide platforms for the generation and handling of lasers that can be co-integrated with CMOS electronics for system control.

For routing, waveguides are required to have small bend radii and wide transparency in the visible region. For qubit operation and optical clock LO, extremely low loss waveguides are needed to make high Q resonators that can provide high extinction for the desired frequency noise characteristics at the required frequency offsets for the LO by acting as external cavities for lasers, self-injection lock cavities, Brillouin lasers, or cold cavities for PDH locks. The loss in waveguides is often dominated by scattering losses [23,24], which scale as $1/\lambda^4$ and are thus a factor of 25-200 higher as compared the C-band (1550 nm) losses. Thus, careful waveguide design in a wide transparency material is required to enable PICs to manipulate and stabilize all wavelengths used for the selected species. Commonly used materials are with low losses reported in visible are 6 dB/m in Si_3N_4 and $LiNbO_3$ at λ = 634 nm and 637 nm respectively [27,48], 22 dB/m at 453 nm and 93 dB/m at 405 nm in Si_3N_4 [28], and 60 dB/m at λ = 458 nm in Al_2O_3 [26,29], but none of these achieve sub-dB/m losses and

have been used for limited beam routing [49] and none have been used for laser stabilization for use as LO.

1.3 Lasers, phase noise, power dependence, intensity, profile

This section briefly discusses the noise spectra in lasers, specifically the definitions used in atomic systems. It then discusses the requirements and limitations imposed on noise by atomic systems as various parts of the noise spectra have different effects on atomic systems, to motivate the development of on-chip stabilization cavities and on-chip Brillouin lasers for reducing the noise in different portions of the spectra of the laser.

1.3.1 Laser spectral noise properties

Laser spectral noise properties determine the coherence of the laser and are often quantified in terms of various definitions of linewidths. Fluctuations in the optical noise of the laser result in laser phase noise and distort the ideal sinusoidal wave, causing the broadening of the laser spectra. Traditionally, the full width at half maximum of the laser spectral profile has been referred to as the linewidth of the laser and is quoted to indicate the spectral purity of the laser source [50–52]; however, it does not provide an easy quantitative visualization of noise at different frequency offsets for which phase noise or frequency noise is often used. The phase noise spectrum is represented by the single-sided phase noise power spectral density (PSD), $S_\varphi(\nu)$ (rad^2/Hz), and is given by the Fourier transform of the autocorrelation function of the phase

$$S\varphi(\nu) = \int_{\tau=-\infty}^{\infty} \langle \varphi(\tau)\varphi(\tau') \rangle d\tau e^{j\omega\tau} \quad 1.1$$

Conventionally, this is also denoted by $\mathscr{L}(\nu)$ (dBc/Hz), which is a single-sideband power in a 1 Hz bandwidth at a frequency offset ν from the carrier frequency ν_0 ($\nu << \nu_0$) and referenced to the carrier frequency power

$$\mathcal{L}(\nu) = 10.log_{10}\left(\frac{S\varphi(\nu)}{2}\right) \quad 1.2$$

The noise can also be represented as a one-sided frequency noise (FN) PSD, which is related to the phase noise PSD as

$$S_f(\nu) = \nu^2.S\varphi(\nu) \quad 1.3$$

In the context of atomic clocks, a more important characterization of laser purity is in terms of fractional frequency stability, which defines the frequency fluctuations y in terms of the deviation from the carrier frequency and its PSD. $S_y(\nu)$ (Hz^{-1}) is related to the FN PSD:

$$S_y(\nu) = \frac{S_f(\nu)}{\nu_0^2} \quad 1.4$$

To characterize the long-term stability of the lasers used as local oscillators and the clock stability, the most often used measurement is Allan variance, also known as Allan deviation (Adev) $\sigma_y(\tau)$, given as

$$\sigma_y^2(\tau) = \frac{1}{2(M-1)} \sum_{i=1}^{M-1} (y_{i+1} - y_i)^2 \quad 1.5$$

Its relation to $S_y(\nu)$ is given as

$$\sigma_y^2(\tau) = 2\int_0^{\nu_h} \mathrm{Sy}(\nu) \frac{sin^4(\pi\nu\tau)}{(\pi\nu\tau)^2} d\nu \quad 1.6$$

where y denotes the i^{th} fractional frequency averaged over the sampling interval τ, and ν_h is the cutoff frequency of the measuring system in Hz. A detailed discussion is given in the seminal papers in the following references [26,50,53–56].

Next, a brief description of the contribution of the different processes to the spectral content of the laser is provided. For a laser limited by purely non-correlated, memoryless, quantum phase noise, that is, white frequency noise only sources, the laser linewidth takes the form of a Lorentzian line-shape and is denoted by the flat slope $1/\nu^0$ in the $S_f(\nu)$ plot and by $1/\tau^{0.5}$ in the Adev plot, as shown in Figure 1.2. The white noise-limited linewidth of the laser is also known as the fundamental linewidth (FLW), Lorentzian linewidth, or intrinsic linewidth, referred to as FLW hereon, and is given as π times $S_f(\nu)$ at the white noise flat floor, as shown in Figure 1.3 (b) [57]. The presence of flicker noise from technical noise sources broadens the line-shape into a Gaussian line-shape and its convolution with the Lorentzian gives a Voigt line-shape, whose linewidth ($\Delta\nu_{LO}$) is referred to as effective linewidth, total linewidth, or integral linewidth (ILW), referred hereon as ILW. The common methods of evaluating ILW in the literature are the integration of the phase noise approach [58], referred to as the $1/\pi$ integral, and the β-separation method [57]. The 1/f slope contribution in the $S_f(\nu)$ plot and $1/\tau^0$ in the Adev plot are referred to as flicker frequency modulation noise, or simply 1/f noise, shown in Figure 1.4. Moreover, the laser can exhibit a slow drift, which can move the center frequency of the Voigt line-shape over time. Such noise present as $1/f^2$ slope contribution in the $S_f(\nu)$ plot and $\tau^{0.5}$ in the Adev plot. The drift affects the capture range during the lock of the LO to the narrow clock transition in atomic clocks as the electronic transitions operate at absolute center frequencies and integral linewidth measurement over a long

observation time and is thus very important for any measurement with atoms, molecules, or ions [56].

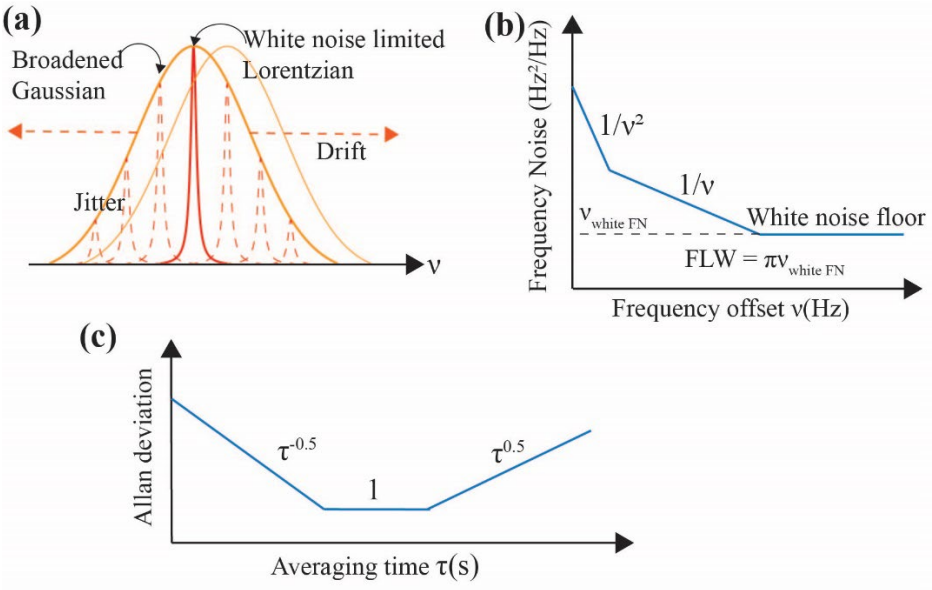

Figure 1.4 Laser noise spectral properties: (a) Laser noise spectra showing white noise limited FLW which is broadened to Voigt line-shape with added technical noise and the drift that moves the entire line-shape over long observation durations. (b) Frequency noise spectra showing the contributions of different noise sources at different frequency offset. (c) Adev plot showing the contributions of different noise sources at different averaging times.

1.3.2 Effect of laser Noise in Qubit and clock operation

Laser Linewidth and coherence:

The process of lasers addressing a narrow atomic transition with photons is a probabilistic absorption process where a stream of photons coherently interacts with the electron to excite it to a long-lifetime state. This is analogous to charging a high Q Fabry-Perot resonator, which depends on the ringdown time (that is, Q) of the resonator. Reducing

the integral linewidth of the laser, thus reducing the power requirement for the lasers, is helpful when using broad linewidth lasers for cooling or for the second stage of cooling using a narrow transition like the 7.5 kHz 689.3 nm transition in Sr. Because the number of cooled atoms scales strongly with the beam diameter and intensity up to saturation, stabilization to a few kHz can be helpful for cooling lasers [34].

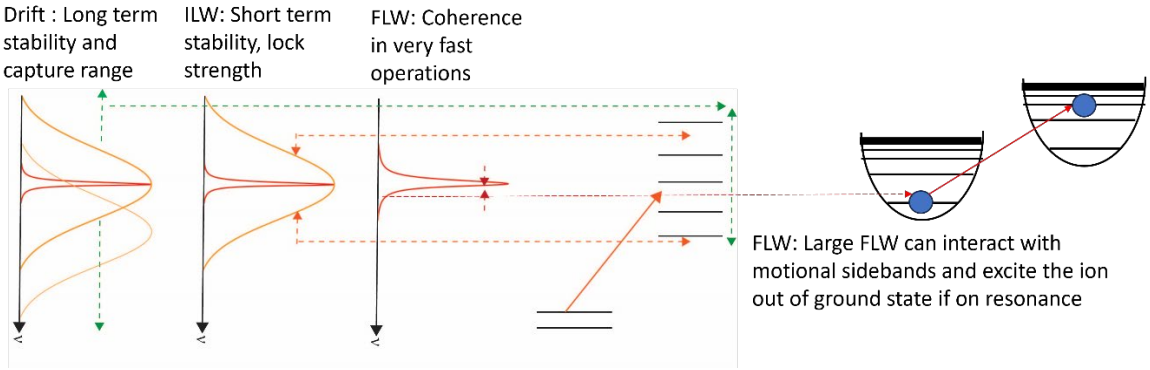

Figure 1.5 Laser noise spectra interaction with cold atoms and ions: Simplified picture of role of various parts of laser's spectrum and how they interact with the atom or ions at a high level.

The linewidth and, more importantly, spectral purity at specific frequency offsets of the lasers in the case of clock transition, the state preparation, and manipulation laser (referred to as LO from hereon) in qubit operation is much more stringent than any other laser used for cooling, trapping, and repumping because the coherence time is directly related to the linewidth of the laser. The coherence time of the species when interrogated in the Rabi process (detailed later), which is a common process used for LO lock to the narrow clock transition, is given by

$$\tau_{coh} = \frac{1}{\pi \Delta \nu_{LO}} \tag{1.7}$$

To achieve this, a certain criterion for frequency or phase noise is needed for a particular atomic system and set of operations and the LO must be locked to a stabilization

cavity using PDH locks. These stabilization cavities are designed to have a high Finesse, as well as high Q, as the discriminant slope in PDH depends on the resonator Q [4,59] or linewidth $\Delta\nu_{cavity}$ and the power in the cavity P_c and power in the sideband P_s as follows

$$D = \frac{8\sqrt{P_c P_s}}{\Delta\nu_{cavity}} \qquad 1.8$$

Moreover, these cavities are designed to have extremely low drift rates and are housed in vacuum to reduce the effects of vibrations [60,61]. Figure 1.6 shows the noise reduction in the laser spectra after locking to the cavity, with the lock to such a cavity reducing the integral linewidth of the laser and giving it the drift rate of the cavity. The PDH servo phase changes to 1 at the servo bandwidth, which adds noise to the laser causing the servo peak, as shown in Figure 1.6 (c). The cavity output can be used instead shown in Figure 1.6 (d). The frequency noise of the locks is shown in Figure 1.6 (e).

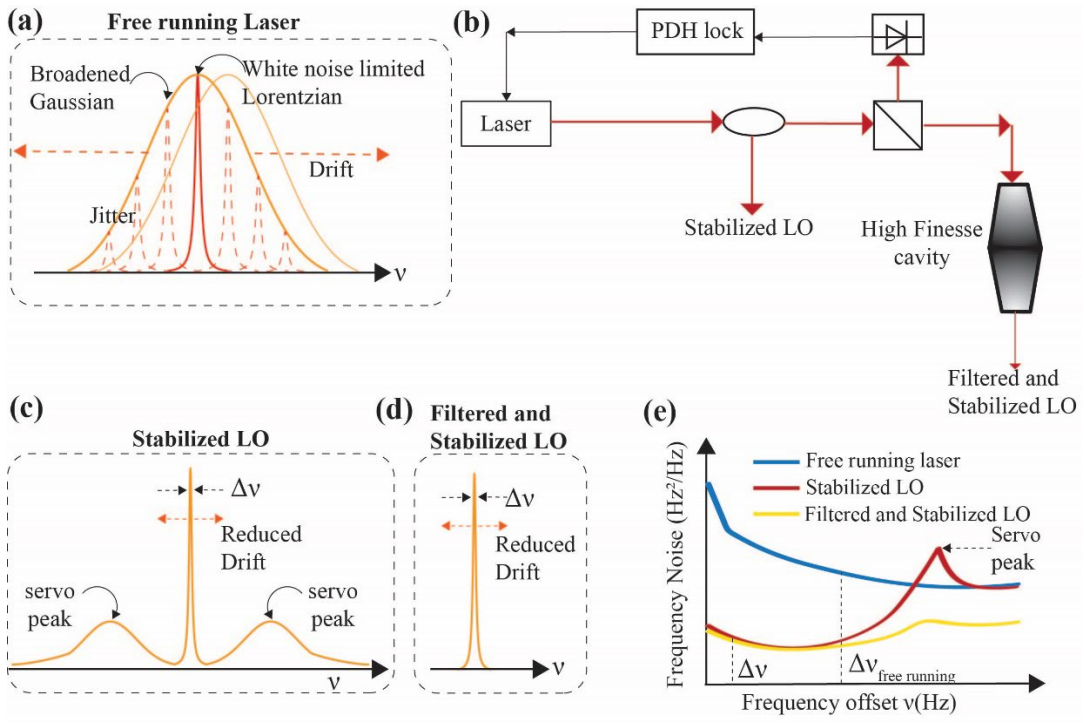

Figure 1.6 Laser Stabilization: (a) Free running laser spectra. (b) Traditional stabilization scheme by Pound-Drever Hall (PDH) lock of laser to a high quality factor, high finesse, low drift stabilization cavity. The output of the laser can be taken from the cavity transmission in which case the cavity acts as a filter and removes the servo peaks added by the PDH lock due to the phase of feedback. (c) PDH stabilized pump laser. (d) Stabilized pump laser with cavity filtered output (e) Effect on frequency noise spectra by locking for the locked laser and locked and filtered laser.

These free-space Fabry–Perot cavities are bulky, free space coupled, and take a large volume and for a significant volume budget in current compact cavities. Waveguide-based stabilization cavities can offer a significant reduction in volume, simplify alignment, and provide more robust operation at the cost of slightly lower performance. To provide frequency noise reduction of multiple orders of magnitude, these will require a high Q factor and critically coupled cavities. Moreover, most state-of-the-art bulk high-finesse cavities are vacuum-spaced and thus do not suffer from thermorefractive noise (TRN) [62], and their performance limitation comes from the thermal noise in the coatings [22]. Thus, waveguide-based stabilization cavities need to provide high Q, low thermorefractive noise, and low drift to be viable compact stabilization cavities for atomic applications.

Dick Effect:

Named after G. John Dick, this effect limits the long-term stability of the atomic clocks from the LO frequency fluctuations (instability) due to a sequential measurement procedure [47]. The LO measurement step is part of several sequential steps, such as cooling, repumping, trapping, state preparation/optical pumping, interrogation using LO, fluorescence detection, and detection to correct for the LO frequency. Every step other than the interrogation and correction is a dead time and results in a limited duty cycle for the correction

of the LO. Meanwhile, the time available for the interrogation and correction steps was limited by the lifetime/Q of the transition. Dick effect is aliasing effect where the high frequency noise related to dead times and duty cycle is aliased into the detection bandwidth. The lock to the atomic transition of the LO cannot distinguish the aliased high-frequency noise from the laser noise in the detection from the LO noise in the detection bandwidth and attempts to correct for it, introducing instability. This effect introduces a sensitivity factor in the fractional stability, which depends on the duty cycle of the detection, dead times, and details of the type of detection involved [47].

There are several ways to reduce the Dick noise, such as reducing the dead time, increasing the probing time, reducing the cycle time while keeping the probe time fixed, changing the probing protocol, and reducing the LO noise further [34]. Reducing the LO noise further also has the advantage of improving the coherence times. Moreover, longer probing times are possible with reduced LO noise. Therefore, a highly coherent source can help reduce the instability caused by the Dick effect.

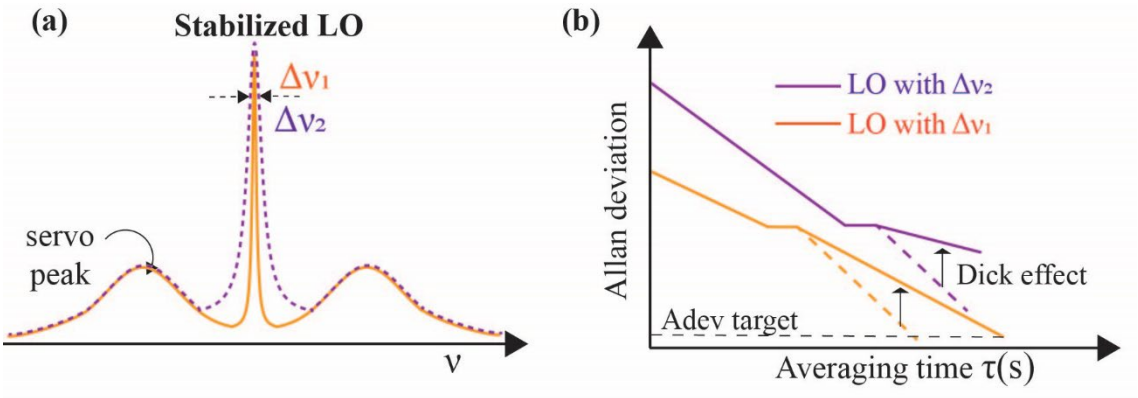

Figure 1.7 Effect of laser coherence and Dick effect on clock stability: (a) Spectra of lasers with different ILW. (b) Adev plot illustrating how the laser coherence and the Dick effect on the stability of an atomic clock. A noisier laser affects the initial stability, and the Dick effect reduces long-term stability.

Effects of far from carrier frequency noise

The process of probing a narrow transition also imparts momentum to the atoms and ions, so the momentum imparted should be small so that it does not increase the motional state of the ions or atoms, which is done in part by confining them in the Lambe-Dicke regime, and it can be reduced by reducing the far from carrier noise that can interact with motional sidebands. In particular, for quantum computing, high-frequency noise can have a significant effect on qubit fidelity [63,64]. One such effect is the high-frequency noise interacting with motional modes or even the magnetically degenerate levels of the ions. This results in the heating of the ions, resulting in a loss of fidelity. It can also cause non-coherent excitations, which also reduce fidelity. The fidelity of a qubit for a sufficiently small noise can be expressed as [63]:

$$F^{(u)} = \frac{1}{2}\left[1 + \exp\left(-X^{(u)}\right)\right] \quad 1.9$$

Where $X^{(u)}$ is the fidelity decay constant and is given by the spectral overlap of the laser noise $S_\varphi(\nu)$ with the filter function of the target operation u of duration τ. The filter functions for a Rabi operation in one qubit gate can take the form of a low-pass filter with cutoff frequency = Rabi frequency times $\nu^2 S\varphi(\nu)$ [64], such that the maximum contribution to noise is from noise around the Rabi frequency and falls off after that. This places a more stringent requirement on laser noise than traditional methods of calculating integral noise, such as the $1/\pi$ integral and β separation. A new method has been recently suggested, named the χ separation line method, which takes into account high-frequency noise, but it has not yet been utilized in other literature.

1.4 Integrated platform requirements

Any integrated platform will need to reduce the high-frequency noise and the servo peak originating from the PDH lock, along with reducing the integral linewidth of the laser for the LO, while spectroscopic stabilization or just a PDH lock might be sufficient for the cooling lasers. Low loss waveguides will be needed for high Q factor of resonators, with > 100 M Q requiring < 0.6 dB/m at 674 nm ($^{88}Sr^{+}$ clock and qubit), 698 nm (^{87}Sr clock) and 778 nm (^{87}Rb 2 photon clock). Moreover, the resonators for locking will require a low thermorefractive noise floor, which is difficult to achieve in waveguides in visible light owing to small mode areas and total length of the cavity (hence the total mode volume). High-frequency offset noise reduction requires the use of nonlinear optical techniques such as self-injection lock (SIL) or stimulated Brillouin scattering (SBS) lasers, as the resonators for PDH locking need to have < 100s of kHz bandwidth if they need to operate as filters for removing servo bumps, which is not possible even with the world's highest Q resonators that have bandwidths of a few MHz to 10 MHz. Ultra-high Q resonators can be used in transmission mode to filter high frequency noise, but locking bandwidth and stability and other factors makes this approach difficult as well as the amount of optical power transmitted is very low, leading to a very low power low noise laser in practice. To address these challenges, this work demonstrates low loss visible waveguides, high Q resonators, SBS lasers, and coil resonators for large-mode-volume stabilization cavities, along with large-area grating emitters for providing cooling beams from the chip.

1.5 Thesis structure and contributions

The structure of this dissertation and contributors to each chapter are as follows, and further listed below: Professor Daniel J. Blumenthal (D. J. B.) is the thesis and research advisor for the full body of the work presented in this thesis. Professor Ryan Behunin (R.B.), Prof. Galan Moody and Prof. Steven DenBaars served as members of the committee and supported the results with helpful discussions and suggestions.

Chapter 2 presents the waveguide loss mechanisms, low loss waveguide design, and high Q resonator design at different visible wavelengths. The measurements of the fabricated waveguides and resonators are presented herein.

Contributors: N.C designed, simulated, built the measurement setup, and measured all the TE0 and TM0 mode devices loss and Q except the 461 nm TE0 Q which was measured by Chad Hoyt (C.H.) at Honeywell and 493 nm TM0 Q which was measured by N.C., Bryan DeBono, and Johanna Zultik at Quantinuum. Naijun Jin and Kaikai Liu (K.L.) did the scattering loss simulations. N.C. performed the absorption loss measurements, and K.L. performed the fitting and simulations for absorption loss. The TE0 mode devices were fabricated by Jiawei Wang (J.W.). The TM0 SBS devices were fabricated in a CMOS foundry under the supervision of Karl Nelson (K.N.). Andrei Isichenko (A.I.) and K.L. wrote the group's common Q-fitting code base.

Chapter 3 presents the design of SBS lasers, spontaneous Brillouin measurements, stimulated Brillouin lasing measurements, and characterization, which includes threshold, efficiency, and frequency noise measurements.

Contributors: R.B. performed the TE0 mode Brillouin gain simulations and helped design the Brillouin gain measurement setup. N.C. designed all the devices for spontaneous Brillouin measurements and all the SBS lasers, measurement setups, and SBS measurements for TE0 674 nm, TM0 698 nm, and TM0 780 nm. A.I. helped with the 780 nm frequency noise (FN) measurements and maintained the F.N code, and Prof. Robert Niffenegger (R.N.) performed 674 nm TM0 SBS measurements in the setup designed by N.C. and K.L. helped with the simulations of TM0 SBS. The TE0 devices were fabricated by J.W. and Debapam Bose (D.B.) while the TM0 SBS devices were fabricated in CMOS foundry under supervision of K.N.

Chapter 4 presents the coil resonator stabilization cavities and their thermorefractive limits, as well as the design and measurements of the laser locked to these cavities.

Contributors: N.C. designed all the devices. N.C. designed the setup and performed the optical frequency discriminator FN for the 698 nm and 674 nm devices. K.L. and N. C. performed measurements on 1319 nm coil resonators together. N.C., K.L., A.I., and Henry Timmers performed the beatnote measurements on a 674 nm coil stabilized laser. The TE0 devices were fabricated by J.W., and the TM0 SBS devices were fabricated in a CMOS foundry under the supervision of K.N.

Chapter 5 discusses the use of a coil stabilized 674 nm laser for various operations with Sr ions, where coil R replaces the bulk free-space Fabry Perot cavity for laser stabilization.

Contributors: N.C. performed the initial setup of the coilR, which was later refined by Prof. R.N. and N.C., R.N. packaged the coils for use with ions. The ion experiments were performed by R.N. and his group members Chris Caron and Nishat Mahzabin Helaly.

Chapter 6 discusses the large-area grating emission photonic integrated circuit (PIC) for generating three orthogonal millimeter-sized beams for generating a 3-D magneto-optic trap (MOT).

Contributors: N.C designed the waveguides and slab expanders, Matthew Puckett (M.P.) and K.N. did the grating emitter design, N.C. performed grating characterizations with some 90 nm core measurements performed by K.N. and some 120 nm core measurements done by A.I., Renan Moreira (R.M.) and N.C did the mask layout and A.I. did the cooling demonstration using the 120 nm core gratings. The fabrication of the 90 nm core gratings was performed by R.M. and D.B., and the fabrication of 120 nm core gratings was performed by D.B.

Chapter 7 summarizes the work in the thesis and discusses the potential future extensions of the work in the thesis, including possible improvements and applications.

Chapter 2: Visible low loss waveguides and high Q resonators

2.1 Introduction

Photonic integration can improve reliability, reduce cost, and size, and enable scalability of traditionally table-top-sized precision lasers and optics for visible light applications, as discussed in Chapter 1. For example, atomic, molecular, and optical (AMO) applications [65] rely on racks of lasers and table-sized optics to perform spectroscopy, trapping and cooling, manipulating, and probing a single atom, ion, molecule, or quantum gate. Today's optics infrastructure presents challenges in scaling the number of atoms, ions, or qubits to improve the sensitivity of a quantum sensor or the computational complexity of a quantum computer. For AMO systems, waveguide loss is paramount to the preservation of photons, and resonator Q plays a critical role in laser linewidth narrowing, phase-noise reduction, and filtering, as discussed in Chapter 1. Photonic integration can address these requirements [66,67] and key functions including photon routing, optical filtering [68], free-space beam formation [49,69–71], and hybrid tunable [72,73] and ultra-low linewidth lasers [7,74]. Realizing a wafer-scale, CMOS compatible, photonic integration platform that delivers ultra-low waveguide losses (< 0.1 dB/cm) and ultra-high Q resonators (> 10 million) across the 400 - 900 nm range is critical to realize these advances.

The choice of waveguide core material, in part, determines the loss and Q in the 400–900 nm wavelength range [10], as well as waveguide design and processing considerations [24]. Wide bandgap waveguide core material choices suited to the visible include silicon nitride (Si_3N_4), aluminum nitride (AlN), alumina (Al_2O_3), tantalum pentoxide

(Ta_2O_5), lithium niobate ($LiNbO_3$), titanium dioxide (TiO_2), silicon dioxide (SiO_2) and diamond [24–31,48,74–83]. In addition to the waveguide core bandgap, nonlinear absorption, intrinsic material absorption in the cladding and substrate, and waveguide side- and top-wall scattering must be addressed when designing this wavelength regime. Because the scattering loss scales as $1/\lambda^4$, it contributes significantly to the shorter end of the visible spectrum. To date, the lowest losses reported are 0.06 dB/cm in Si_3N_4 and $LiNbO_3$ at λ = 634 nm and 637 nm respectively [27,48], 0.22 dB/cm at 453 nm and 0.93 dB/cm at 405 nm in Si_3N_4 [28], and 0.6 dB/cm at λ = 458 nm in Al_2O_3 [26,29]. Resonator Qs in the visible region have mostly been relegated to sub-million [34], with a record-high of 11 million reported at λ = 637 nm in $LiNbO_3$ and recently 6 million at 453 nm in Si_3N_4 [28]. The Q factors used till now has referred to the intrinsic Q factor (Q_i) which depends only on the waveguide loss of the resonator, adding a waveguide for coupling to a resonators adds a coupling factor which is a loss for the energy stored in the resonator and is referred to as loaded Q (Q_l) and is the useful Q of the resonator [84].

This chapter introduces waveguide loss mechanisms and waveguide designs to minimize the loss from each contribution. The waveguide design for low loss is weighed in with the tradeoff of bend radius, and different core geometries are discussed with different losses, multiple or single-mode operation, and dilute or moderately confined modes with different loss and footprint budgets.

This chapter discusses low loss, visible, and single-mode-only waveguides using dilute mode Si_3N_4 fundamental transverse electric (TE0) mode waveguides first. The single-mode waveguides that support only TE0 exhibit losses from 1 to 9 dB/m for wavelengths

ranging from 450 nm to 802 nm and an associated intrinsic resonator Q of 60 Million to 9.5 Million, a decrease in loss by factors of 6x to 2x and an increase in Q by factors of 10x to 1.5 × over this visible wavelength range compared to other low-loss visible waveguides in the literature. Additionally, the absorption limited loss and Q of 0.17 dB/m and 340 million at 674 nm are demonstrated which present a limit to the loss and Q that can be achieved in a regular rectangular waveguide.

This chapter then presents the lowest loss waveguides in visible for any visible integrated platform by reducing the losses further using the fundamental transverse magnetic (TM0) mode in multimode waveguides supporting both TE0 and TM0 modes. This is because the waveguide loss in low-loss dilute-mode waveguides is limited by the top and bottom surface roughness rather than the sidewalls, as shown by simulations, and the TM0 mode exhibits lower scattering loss from the top and bottom scattering [23]. These TM0 waveguides are demonstrated sub 1 dB/m losses at visible wavelengths, fabricated in CMOS foundry process, with losses and associated Qs of 2.11 dB/m, Q_i = 39 x10^6 at λ = 493 nm, 0.6 dB/m and Q_i = 94 x10^6, at λ = 674 nm, 0.51 dB/m, Q_i = 114 x10^6 at λ = 698 nm and 0.36 dB/m, Q_i = 145 x10^6 at λ = 780 nm. These low losses will enable low threshold narrow linewidth stable sources in the visible region, for which Brillouin lasers and stabilization cavities will be discussed later. This chapter concludes by presenting flexible coupling through the use of two-point coupled resonators that allow for tunability of coupling by phase change of the arm of the coupler or by changing the wavelength. Figure 2.1 below shows comparison of our losses and Q with lowest state of the art losses and Q from literature in visible wavelengths. Table 2.1 summarizes the loss results from this chapter at the end of the chapter. Parts of this chapter are adapted with permission form our publications [11,75].

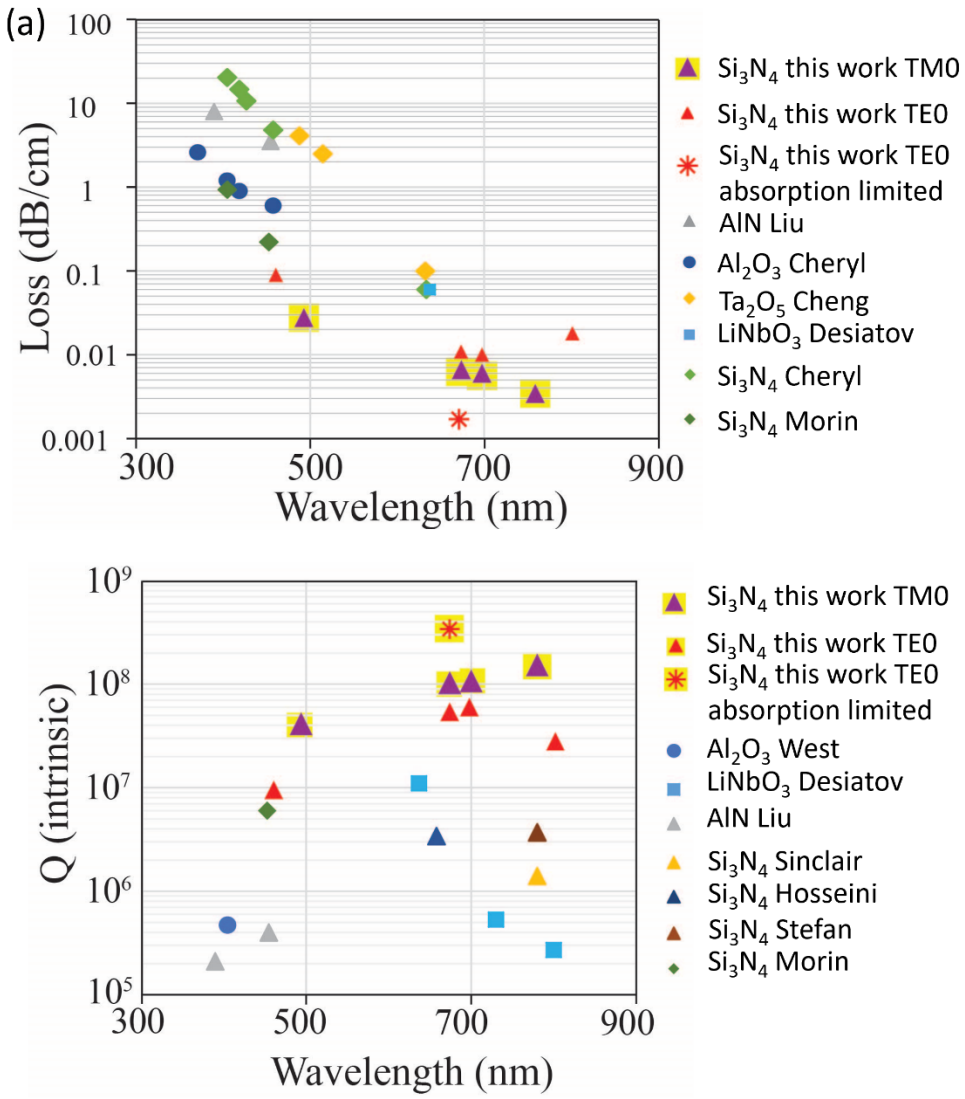

Figure 2.1 Literature Loss and Q comparison: (a) Comparison of losses of our Si_3N_4 waveguides with other state of the art waveguide losses in visible: AlN Liu [25], Al_2O_3 Cheryl [26], $LiNbO_3$ Desiatov [27], Si_3N_4 Cheryl [26], Si_3N_4 Morin [28]. (b) Comparison of intrinsic Q factors of our resonators in visible with literature: Al_2O_3 West [29], $LiNbO_3$ Desiatov [27], AlN Liu [25], Si_3N_4 Sinclair [30], Si_3N_4 Stafan [31], Si_3N_4 Morin [28].

2.2 Loss: mechanisms and mitigation in waveguides

There are three major loss categories in waveguides: absorption, scattering, and radiative losses. Absorption loss results from material absorption, defects, metal impurities, and unfulfilled bonds in waveguides. The choice of waveguide core and cladding material and fabrication have a major impact on this loss. Electronic absorption and bond absorption also set the transparency window of the material. We chose Si_3N_4 core and SiO_2 cladding as they have been demonstrated to have low loss in IR [24,59] with Si_3N_4 having a large transparency window from 405 nm to 2000 nm and SiO_2 having an even larger transparency window with low absorption losses for both visible [85,86] for both materials. Fabrication optimization for visible light was not explored in this thesis.

The second major source of loss is the scattering loss. It can originate either from particles/roughness, which is much smaller than the wavelength, called Rayleigh scattering, or larger particles (wavelength/10 or larger), called Mie scattering. Rayleigh scattering scales as $1/\lambda^4$, is the major contributor to losses in visible wavelengths, and increases as the wavelength is reduced from the red to the blue end of the spectrum. Mie scattering can result from particles in fabrication and can result in split resonances, but is negligible to absent in the CMOS process due to much lower particles than a research cleanroom. Scattering from larger particles is independent of the wavelength. Rayleigh scattering in this work's low loss waveguides is reduced by designing dilute mode waveguides [24,87,88], where the mode area is large and only a small fraction of the mode lies inside the core; thus, only a small fraction of the mode overlaps with the waveguide sides. Furthermore, they are designed as large aspect ratio waveguides with small heights and large widths. This is done to reduce the overlap with

the sidewalls, which are defined by the waveguide etch and are 10-50 times rougher than the top surfaces of the waveguides, which are defined by the deposition process. Figure 2.2 shows the loss mechanisms, dilute-mode waveguide design and loss, Q, and footprint tradeoffs in dilute mode.

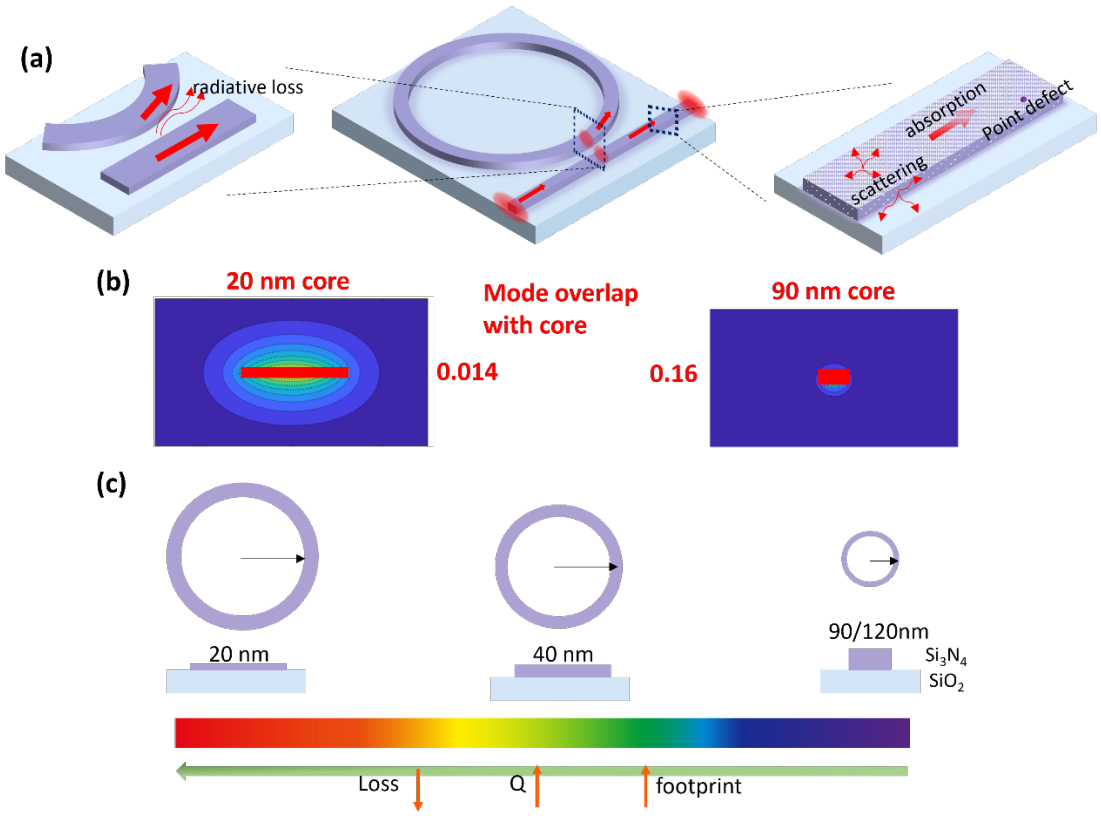

Figure 2.2 Waveguide loss and design: (a) Loss mechanisms in waveguides showing three major loss contributors, absorption, scattering and radiative. (b) Dilute mode large aspect ratio waveguide with extremely low overlap with the core, comparison between 20 nm dilute mode core and 90 nm moderately confining core shows that the overlap is 10x lower in the dilute mode core. (c) Waveguide footprint increases with decreasing mode confinement or with increasing wavelength to avoid radiative losses.

Reducing the radiative losses from the air and substrate requires making the cladding thick such that the evanescent tail of the mode is completely confined in the cladding and does not extend to the substrate or air at the cost of additional fabrication time. Reducing the radiative losses from the bends requires increasing the number of bends. The bend loss scales as $\propto e^{1/R\sqrt{n_{eff}}}$, the dilute mode waveguides have lower n_{eff} and thus need larger bend radius to reduce the radiative losses. Thus, very dilute mode waveguides require larger bends and resonator radii, making the structures large, which is a tradeoff with low loss, as shown in Figure 2.2 (c). Other advantages of low-loss Si_3N_4 waveguides are as follows.

- **CMOS Compatible:** Si_3N_4 waveguides have a wide transparency (405-2350 nm) window and low absorption, and the fabrication process is CMOS-compatible.

- **Simpler and fabrication robust Couplers:** Dilute mode allows strong coupling even with wider gaps. Even this work's short wavelength 461 nm rings have gaps of ~ 1 μm in simple point couplers. The DUV photolithography resolution of the UCSB cleanroom was approximately 200 nm, and these couplers were easily defined by the DUV.

- **Large Mode Area:** Helps with designing low TRN cavities discussed in chapter 4.

- **Negligible radiative losses:** We use thick cladding, so the waveguide has no radiative loss to the substrate or air and is well protected from the environment. Dilute mode waveguides with large bends also have a low mode mismatch where the bend direction changes, resulting in negligible bend transition losses.

2.3 Fundamental TE0 mode waveguides and resonators

2.3.1 Waveguide design

This dilute mode low confinement waveguides have lower sidewall scattering loss, lower core absorption loss, and single-mode operation. We utilized the dilute mode waveguides and engineered the mode to have a large effective mode area with reduced overlap with the sidewall to minimize the loss. This is achieved by selecting the widest width that supports a single TE or quasi-single TE mode. A quasi-TE mode waveguide is designed by selecting a core width in which both the fundamental TE0 and TM0 are supported, but TM0 has a very high bend loss and can be filtered out by selecting an appropriate bend radius [89]. Because the same core thickness is used in the entire wavelength range of 461–802 nm, structures for different wavelengths in this range can be placed on the same die with only the width change in the mask design to accommodate different wavelengths. This opens up the possibility of using structures for multiple wavelengths on the same device. A comparison of low loss dilute mode waveguides with moderate confinement waveguides, which were also designed as part of this thesis, is made.

The low loss, low confinement waveguide has a 20 nm thick Si_3N_4 core. The moderate confinement waveguide is a 90 nm thick core [75] and has the advantage of smaller structures and higher density at the cost of slightly higher loss. The mode profiles and bend loss (excess loss due to bends) for both cores are shown in Figure 2.3 for λ = 461, 674, and 802 nm, with the mode at λ = 698 nm being like the mode at λ = 674 nm. A parameter called the critical bend radius is defined as the radius above which the loss contribution from the bends is $< 10^{-2}$ dB/m. When designing the ring resonators and S-bends, the bend radii are maintained above

the critical bend radius. The loss comparison between the 90 nm thick core waveguide and the 20 nm thick core waveguide shows a significant loss reduction by choosing a thinner waveguide core, which verifies the previous claim of loss dominated by sidewall roughness. This was further verified by absorption loss measurements. A thicker core can be used in applications where loss is not as critical and a higher component density is required, as the smaller critical bend radii allow for integration density. One example of where the thicker core is used in this work being large area grating emitters where the bends are designed to be 0.5 mm and the slab expander footprint also benefits from the thicker core and gets prohibitively long in thinner cores.

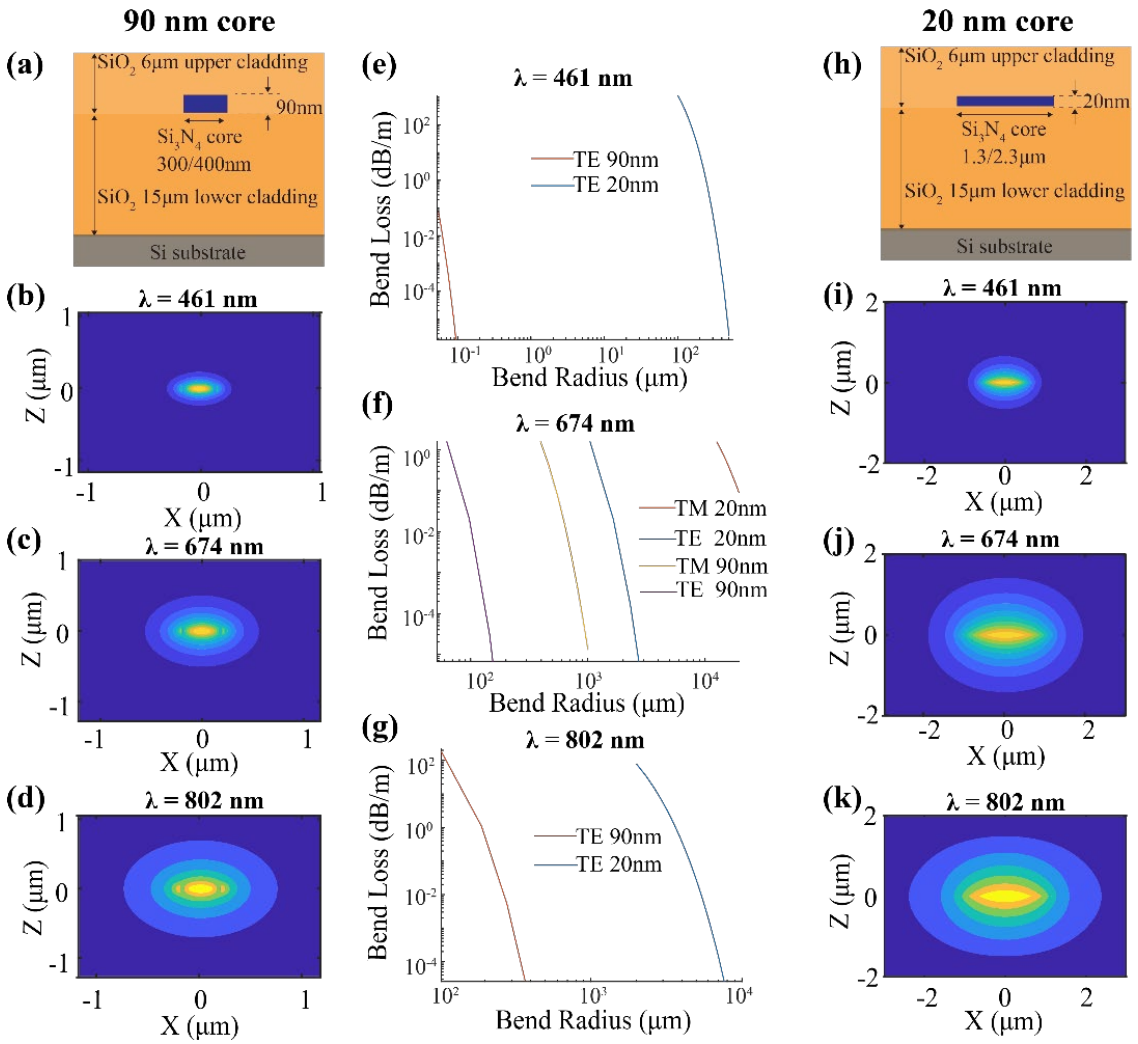

Figure 2.3 Simulation and design of waveguides with comparison of 20 nm low loss core with 90 nm core: (a) Waveguide cross section in 90 nm core geometry. (b), (c), (d) Mode profiles in 90 nm core for λ = 461 nm, 674 nm, 802 nm respectively. (e), (f), (g) Critical bend radius for λ = 461 nm, 674 nm, 802 nm respectively, 461 nm and 802 nm only support single TE in both 20nm and 90 nm core geometry, 674 nm supports TM which has very high loss in bends and can be filtered out by choosing bend radii smaller than 10 mm in 20 nm core geometry and smaller than 1 mm in 90 nm core geometry (quasi TE only). (h) Waveguide cross section in 20 nm core geometry. (i), (j), (k) Mode profiles in 20 nm core for λ = 461 nm, 674 nm, 802 nm.

Cutback spirals and ring resonators were designed for loss characterization. Spirals and resonators also form building blocks for a multitude of different passive components, such as

delay lines, filters, SBS lasers, external cavity tunable lasers, etc. For the 20 nm core, a 2 m spiral was designed to evaluate the loss at 450 nm and 674 nm, and straight waveguides were used to extract the coupling loss from the waveguides. Multiple cutback spirals are not possible because of the large footprint of the devices. In the 90 nm core, cutback spirals were designed with three different lengths: 0.5, 1, 1.5 m. Along with these spirals, bend loss measurement structures were designed with multiple S bends with radii of 50, 100, 200, and 400 μm. For the 20 nm core, ring resonators with radii of 3 mm for $\lambda = 461$ nm, 8.9 mm radius for $\lambda = 674$ nm, and 10 mm for $\lambda = 802$ nm were designed and fabricated. The resonator power coupling factor ($\boldsymbol{\kappa}^2$) is ~ 16% at $\lambda = 461$ nm, 1.5% at $\lambda = 674$ nm, 1% $\lambda = 698$ nm and 57%, at $\lambda = 802$ nm. The resonators were designed to be overcoupled at 461 nm and 802 nm, critically coupled at 674 nm, and undercoupled at 698 nm. Test structures are employed to independently measure $\boldsymbol{\kappa}^2$, and are used with the Q measurements to extract loss from resonators.

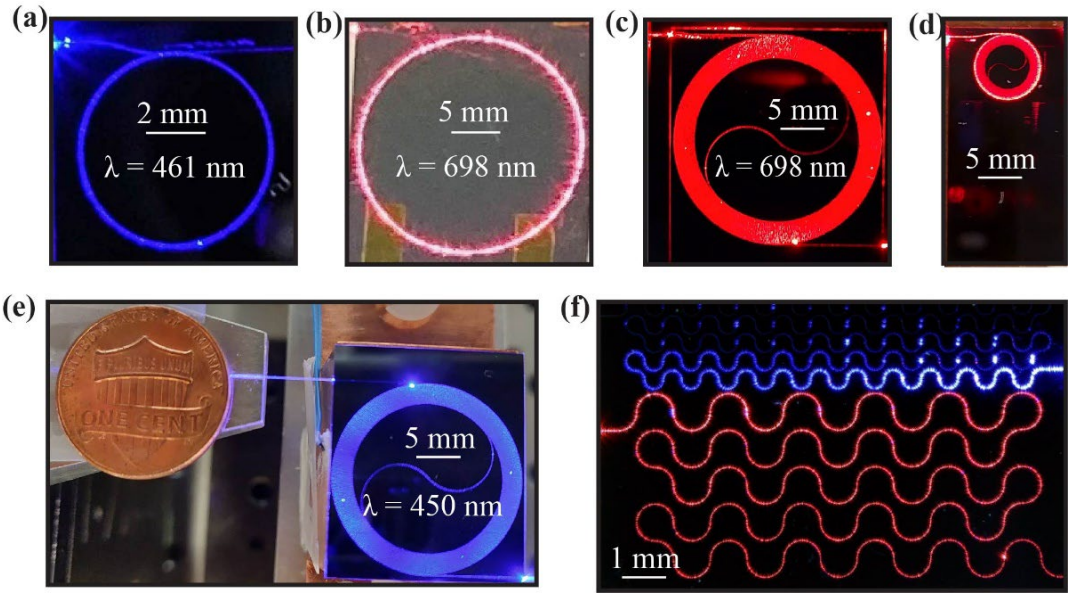

Figure 2.4 Structures for waveguide loss measurements: (a) 20 nm core, R = 3 mm resonator for 461 nm Q measurement. (b) 20 nm core, R = 9.4 mm resonator for 698 nm Q measurement. (c) 20 nm core, 2 m coil for measuring propagation loss at 698 nm. (d) 90 nm core, 1 m cutback spiral for loss measurement. (e) 20 nm core, 2 m coil for measuring propagation loss at 450 nm with a penny for size comparison. (f) 90 nm core, bend loss measurement S bends.

2.3.2 20 nm core waveguide and resonator measurements

The intrinsic and loaded Qs of the all-pass ring resonators were measured, and the waveguide losses and absorption-limited loss were extracted from these measurements. Spiral coils were used to measure the propagation losses directly and compared to the losses obtained using the resonators. A 3 mm radius resonator was used for Q measurement at 461, and a 2 m coil was used for propagation loss measurements at 450 nm. A 9.4 mm radius resonator was used for Q measurement at 698 nm and two meter coil was used for propagation loss measurements at 698 nm.

Q at λ = 674 nm and λ = 802 nm was measured using a frequency-swept source calibrated by an unbalanced Mach–Zehnder interferometer (MZI) method [24,74], as shown in the schematic in Figure 2.3(f). Q at λ = 461 nm and λ = 698 nm was measured using a swept source that was calibrated by adding sidebands at a known frequency offset from the carrier and then sweeping the carrier as well as the sidebands across the resonance [24]. The MZI was calibrated, and the Q values obtained using the MZI and sideband methods matched well with the values obtained from cavity ring-down measurements from previous publications [24,74]. Ring down could not be performed, as the ring down time of a few nanoseconds for these devices would require a fast shutter/modulator that was not available

for visible light. Loss is extracted from resonators Qs and coupling coefficients from test structures as the fit on the Q gives two Q values for intrinsic loss, one corresponding to the intrinsic loss and one corresponding to the coupling loss, and independent measurement of coupling or measurement of two rings with the same intrinsic but different coupling loss is required to separate the two. Figure 2.4 shows the frequency sweeps of the resonators for extracting Q. Both intrinsic Q and loaded Q are reported. Intrinsic Q is dependent on the resonator loss only and the intrinsic Q gives a limit to Q. Loaded Q is when the resonator is coupled to a bus and includes coupling losses and is the Q used in applications.

At λ = 698 nm, the intrinsic Q = 60 million and loaded Q = 34.4 million (Figure 2.5 (a)) were measured with a corresponding calculated 0.01 dB/cm (1 dB/m) loss. At λ = 674 nm, the intrinsic Q = 54.4 million and loaded Q = 27.7 million (Figure 2.5 (b)) with a corresponding 0.01 dB/cm (1 dB/m) loss. At λ = 802 nm the intrinsic Q = 28.3 million and loaded Q = 0.81 million (Figure 2.5 (c)), corresponding to a 0.02 dB/cm (1.8 dB/m) propagation loss. At λ = 461 nm, the loaded Q = 1.65 million and intrinsic Q = 9.5 million (Figure 2.5 (d)) with a corresponding 0.09 dB/cm (9 dB/m) loss. At λ = 698 nm, the propagation loss measured using the spiral (Figure 2.5 (c)) is 0.03 dB/cm (3 dB/m). The mismatch at λ = 698 nm between the resonator and spiral loss might be due to the increased number of particles on the spiral waveguides compared to the resonators. At 802 nm, the loss measured from the resonator is also higher than expected owing to particles, as seen in the right portion of the 802 nm resonator in Figure 2.5 (e). The propagation loss at λ = 450 nm is 0.08 dB/cm (8 dB/m), obtained from the spiral in Figure 2.5 (e), [75] which matches well with the calculated 0.09 dB/cm (9 dB/m) loss from resonator at λ = 461 nm. The fiber-to-chip coupling losses were 3 dB/facet at λ = 461 nm, 4.5 dB/facet at λ = 674 nm, and 3.5 dB/facet at λ = 802 nm. These

coupling losses can be improved by utilizing mode-size converters at the facets and polishing the facets [90].

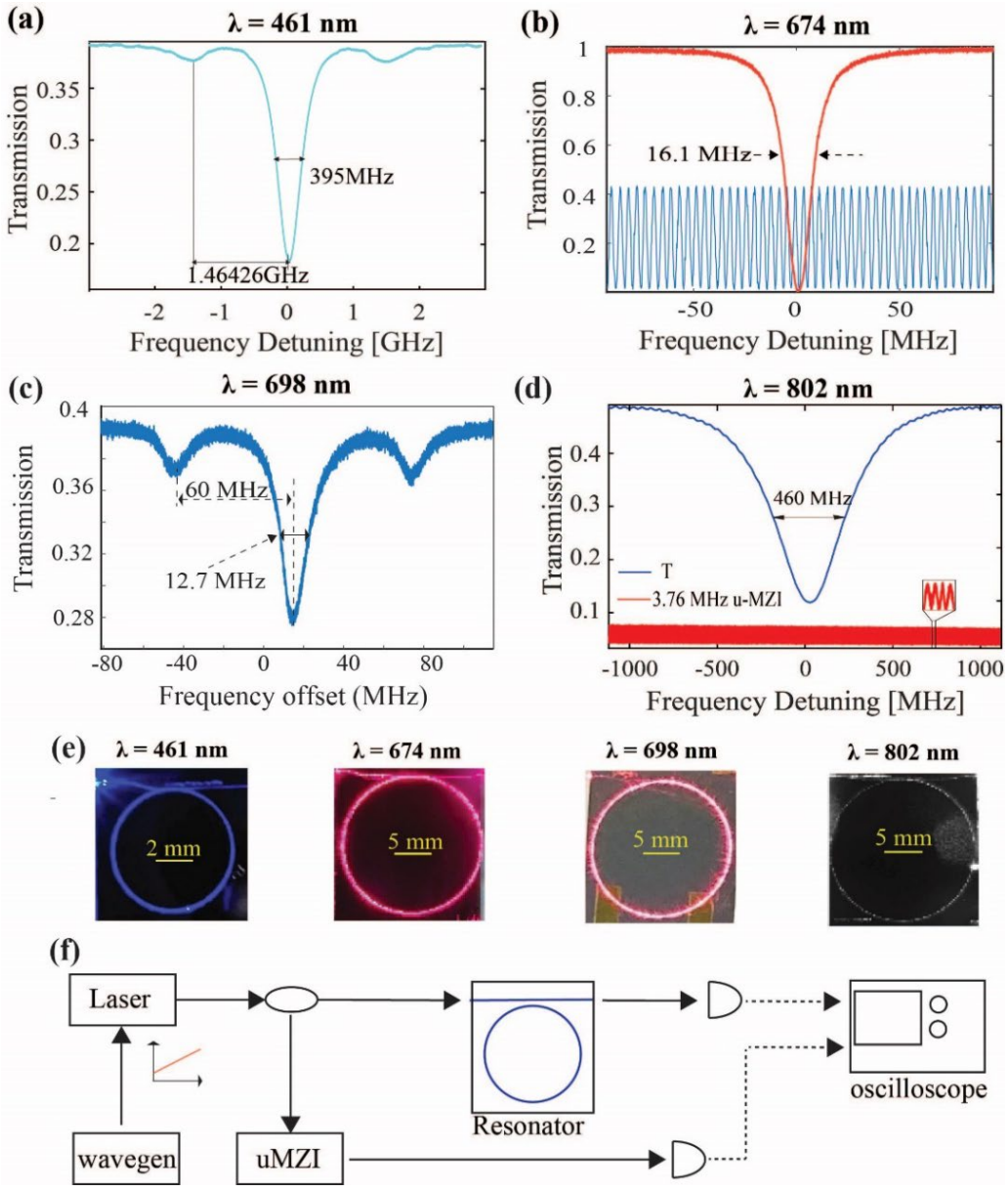

Figure 2.5 Q Measurements: (a) T is resonator transmission spectrum, Q measurement for ring of R = 9.4 mm, loaded Q = 34.4 million and intrinsic Q = 60 million at λ = 698 nm. (b) Q measurement for ring of R = 8.9 mm, loaded Q = 27.7 million and intrinsic Q = 54.4 million at λ = 674 nm. (c) Q measurement for ring of R = 10 mm, loaded Q = 0.81 million and intrinsic Q = 28 million at λ = 802 nm. (d) Q measurement for ring of R= 3 mm, loaded Q = 1.65 million and

intrinsic Q = 9.5 million at λ = 461 nm. (e) Images of resonators during Q measurements, the bright spot in 802 nm resonator is a particle in vicinity of waveguide.

2.3.3 20 nm core absorption loss measurements

The absorption loss at 674 nm was measured to separate the contributions of the absorption and scattering losses and determine the potential loss, and Q, given that the scattering loss is reduced to below absorption. This measurement follows a technique to quantify the resonance photothermal induced bistable linewidth shift [24] using a spectral scan across resonance with a high on-chip power that induces a photothermal resonance redshift that is comparable to the resonance linewidth. This photothermal effect is a direct result of the absorption heating in the resonator. As shown in Figure 2.6 (a), the red detuning (from shorter wavelength to longer wavelength) across the resonance heats up the resonator and induces a resonance redshift, resulting in a skewed line-shape. The thermal impedance of the ring resonator was simulated using COMSOL ® to extract the absorption loss relative to the total loss. Assuming $R_{th} = 9.72\ K/W$, the thermal-optic redshift with a global heating of the chip is measured, $\Delta f_{res}/\Delta T = 9.31\ GHz/K$, which yields the resonance redshift per milliwatt of optical power absorbed by the resonator, $\Delta f_{res}/P_{abs} = 38.0\ MHz/mW$. As shown in Figure 2.6 (b), the resonance redshift has a linear relationship with on-chip power, confirming the photothermal heating effect, from which the absorption loss to be 0.17 dB/m which is < 15% of total loss is extracted. The intrinsic Q corresponding to this absorption loss is ~ 340 million at λ = 674 nm. This shows that the losses are scattering limited in red with > 85% contribution

from scattering, and further improvements in losses to below < 1 dB/m and Qs in excess of 100 million at red are possible by reducing the sidewall scattering.

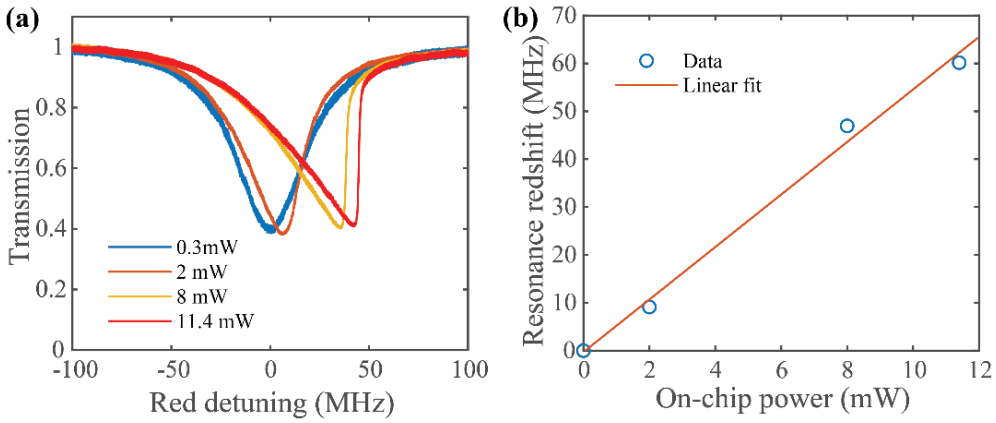

Figure 2.6 Thermal bi-stability measurement: (a) Resonance transmission at different on-chip powers (power in the bus waveguide) showing thermal redshift. (b) Rate of resonance redshift from fit = 5.4 MHz/mW.

2.3.4 90 nm core loss measurement

The losses in the 90 nm core were measured with 'cutback' in-out spirals of three different lengths: 0.5, 1, and 1.5 m. Two sets of interleaved spirals were designed: one set with a width of 300 nm for λ = 450 nm and another set with a width of 400 nm for λ = 698 nm and λ = 802 nm. The losses are plotted in Figure 2.7 below. The measured propagation losses were 5 dB/cm for λ = 450 nm, 0.24 dB/cm for λ = 698 nm and 0.13 dB/cm for λ = 802 nm, respectively. The facet coupling losses extracted from the cutback loss fits were 6.5, 4 dB/facet and 4.5 dB/facet, respectively. Facet tapers are designed and measured to reduce the facet coupling loss at λ = 698 nm and λ = 802 nm and reduce the facet loss to 3 dB/facet and 2.7 dB/facet respectively (Figure 2.7(c)). We also measured the S-bend structures for bend

loss measurements and found that the bend loss measurements agree well with simulations with a critical bend radius < 100 μm for λ = 450 nm, ~ 100 μm for λ = 674 nm, and ~ 200 μm for λ = 802 nm.

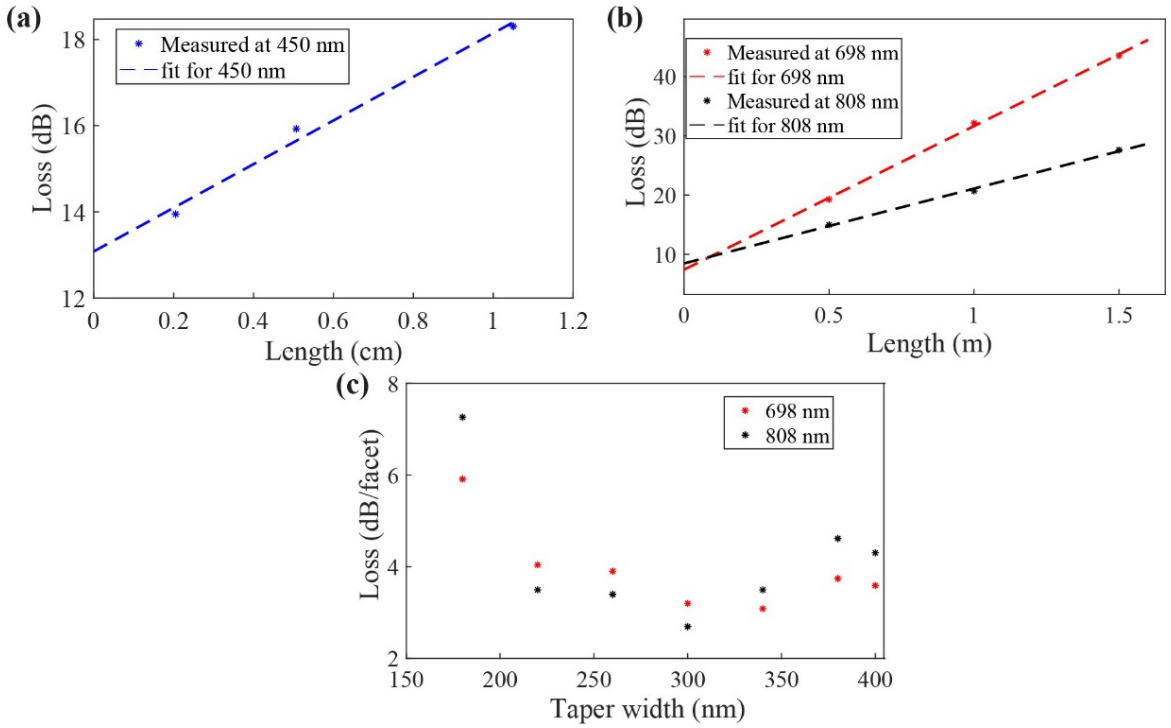

Figure 2.7 Loss measurement in 90 nm core: (a) Cut-back measurement at λ = 450 nm with 5 dB/cm loss. (b) Cutback measurement at λ = 674 nm, 802 nm with 0.24 and 0.13 dB/m loss. (c) Taper loss measurement for reduction in facet loss yielding 3 dB/m loss at λ = 674 nm and 2.7 dB/facet loss at λ = 802 nm.

2.4 TM0 mode waveguides and resonators

2.4.1 Waveguide design

This waveguide design consists of dilute mode, high aspect ratio waveguides supporting both fundamental TE (TE0) and TM (TM0) modes, with the TM0 mode being the lower loss mode. Scattering simulations on dilute mode waveguides [23] suggest that the total losses are limited by scattering from top waveguide surface and the TM0 mode surface scattering is significantly lower than the TE0 mode scattering loss. The simulation for the total scattering loss was performed at 674 nm and showed a loss reduction for the TM0 mode compared to the TE0 mode in the 20 nm core. However, because of the large bend radii required for TM0 in the 20 nm core, a core thickness of 40 nm supports the TE0 and TM0 modes, and the waveguide width is varied to support different wavelengths from 493 nm to 780 nm in the same core. There is a tradeoff between the waveguide width and bend loss, with smaller widths having lower scattering losses but higher bend losses, resulting in a larger critical bend radius. We define critical bend radius as bend radius above which the loss contribution from bend is < 0.01 dB/m and can be neglected. The waveguide widths are 1.2 um for λ = 493 nm, 2.3 um for λ = 674 nm - 698 nm and 4 μm for λ = 780 nm with critical bend radius of 1 mm for 493 nm and 2 mm for the rest of the wavelengths.

Resonators with different radii were designed for loss measurements and other functionalities. For λ = 493 nm, different gap resonators were designed with radius R = 2 mm. For λ = 780 nm Resonators are designed with R = 5.4 mm and 4.4 mm with different gaps to extract the intrinsic and coupling losses. For λ = 674 nm and 698 nm, two different sets of resonators are used for loss measurement, 3 m waveguide length coil resonators, in which the

waveguide width is adiabatically increased to 3 µm to avoid bend losses in the central S bend. The second set of resonators was made with a two-point coupler design, which will be detailed later.

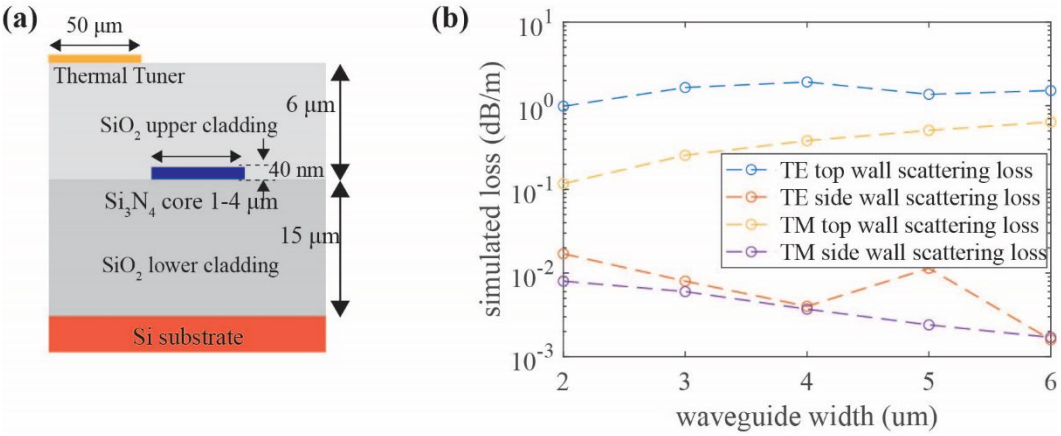

Figure 2.8 TM0 waveguide design: (a) waveguide cross-section. (b) Comparison of scattering loss at λ = 674 nm for a 20 nm thick core waveguide, demonstrating that the losses are dominated by scattering from the surface rather than the sidewalls. The sidewall loss decreases with increasing core width as the overlap with the sidewall decreases, but the top surface TM0 loss increases with increasing width owing to a higher overlap with the top surface.

2.4.2 40 nm core loss and Q measurement

The waveguide loss measurement was performed by measuring the Q factors of the resonators using the calibrated MZI method, such as the TE loss measurement. The measured losses and Quality factors are of 2.11 dB/m, Q_i = 39 x10^6 at λ = 493 nm, 0.6 dB/m, and Q_i = 94 x10^6, at λ = 674 nm, 0.51 dB/m, Q_i = 100 x10^6 at λ = 698 nm and 0.36 dB/m, Q_i = 145 x10^6 at λ = 780 nm. These are the lowest losses reported to date and the first sub 1 dB/m losses and first over 100 million Q factors for any visible wavelength waveguide. Figure 2.9 shows the Q measurements of the resonators.

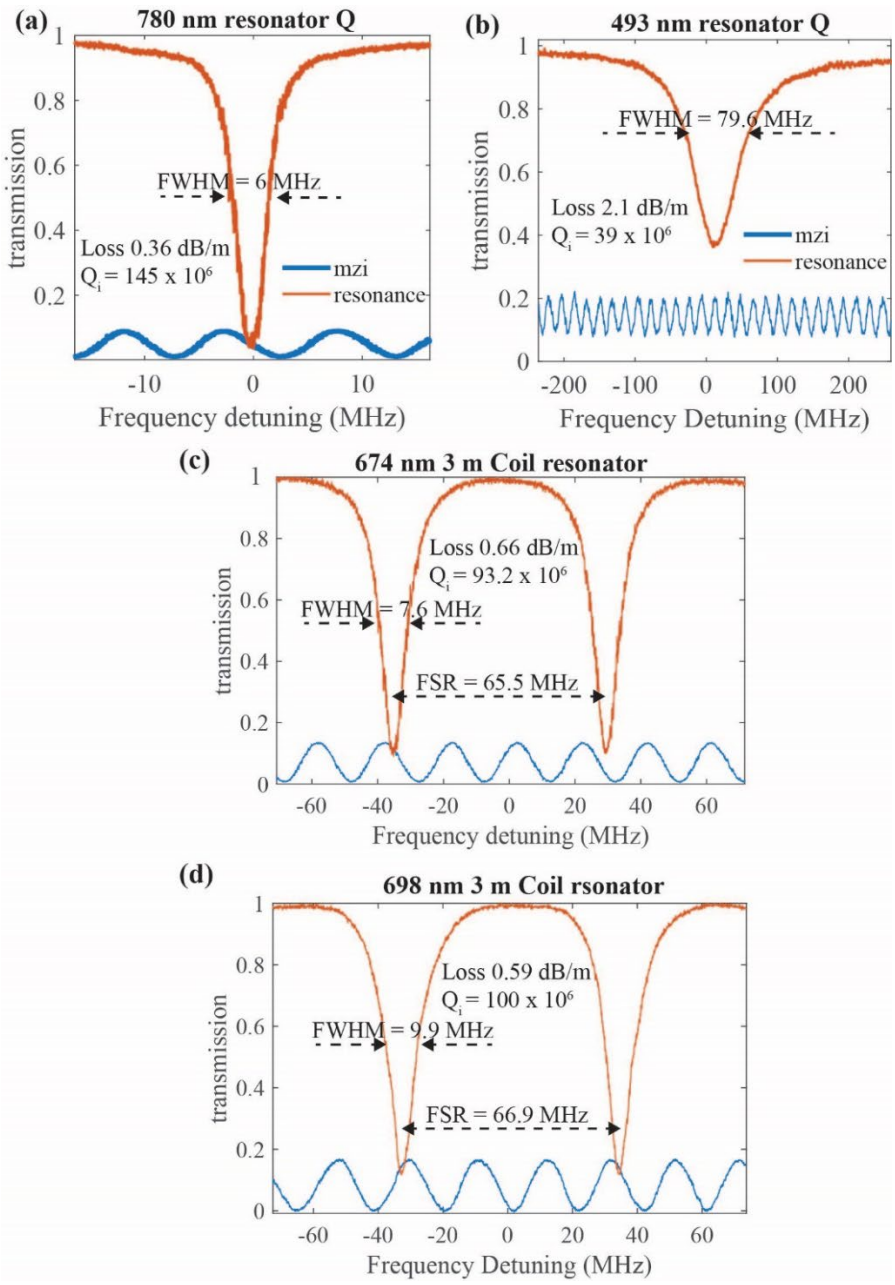

Figure 2.9 TM0 waveguide resonator Q measurements: (a) 780 nm resonator with Q_l = 64 x 10^6, Q_i = 145 x10^6. (b) 493 nm resonator with Q_l = 7.6 x 10^6, Q_i = 39 x10^6. (c) 674 nm resonator with Q_l = 58.5 x 10^6, Q_i = 93.2 x10^6 and FSR = 65.5 MHz. (d) 698 nm resonator with Q_l = 43.4 x 10^6, Q_i = 100 x10^6 and FSR = 66.9 MHz, all the resonators were fabricated in 8 inch CMOS fabrication.

2.4.3 120 nm core loss and Q measurement

The losses in the 120 nm core are measured with 'cutback' in-out spirals of three different lengths: 0.5, 1, and 1.5 m. The spirals were designed with a 900 nm width for λ = 780 nm as the fabrication robust width compared to the narrow 400 nm width for the TE0 only mode as the ASML stepper resolution at the UCSB is ~ 250 nm. Along with spirals, resonators are designed to measure the loss in an independent method and are designed for radii R = 1 mm, 0.75 mm, 0.5 mm; resonators with different radii are designed to measure the critical bend radius. The losses of the cutback spirals and the R = 1 mm resonator are plotted in Figure 2.10 below. For λ = 780 nm, the measured propagation losses are 3.1 dB/m from the spiral and 2.4 dB/m from the R = 1 mm and R = 0.75 mm resonator, showing a good agreement. R = 0.5 mm resonator yielded a loss of 26 dB/m, giving a critical bend radius of ~ 0.75 mm.

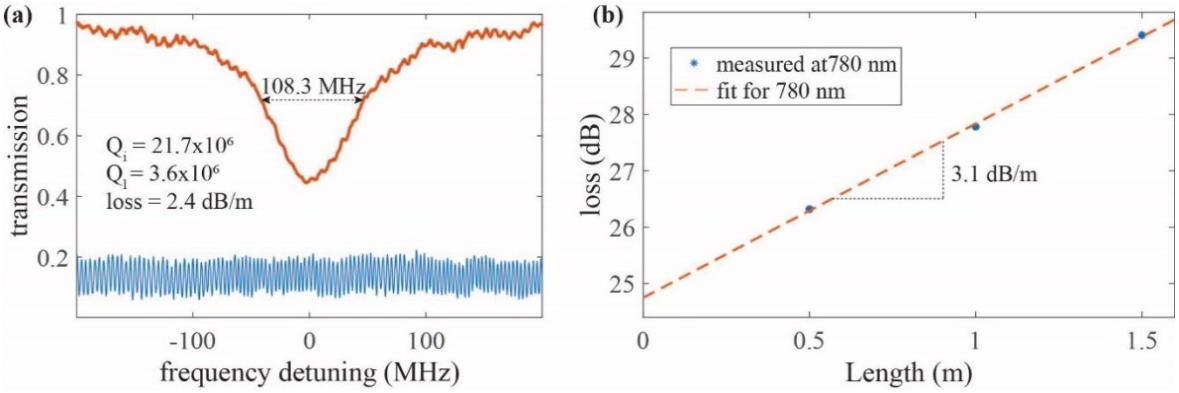

Figure 2.10 TM0 120 nm waveguide measurements: (a) 780 nm resonator with $Q_l = 3.6 \times 10^6$, $Q_i = 21.7 \times 10^6$. (b) Loss measurement from cutback spirals = 3.1 dB/m which agrees well with the loss extracted from resonator.

2.4.4 Resonators with two point coupler

Resonators can be designed with a two-point coupler, where the coupling section is an MZI that provides tunable coupling for the resonators. Such resonators have been demonstrated [91–97] and utilized for tunable bandwidth resonators, filters, and for the extraction of losses using a single resonator. These allow loss extraction using single resonators as different Q values can be measured for different k values, and the fit will give the same intrinsic loss but different coupling losses, making it possible to identify the two possible without a second resonator or coupling test structure. These also enable fabrication robustness, as the couplings can change in fabrication from shrinkage of the waveguide, minor differences in indexes, minor changes in core thickness, etc. Moreover, these also enable wide bandwidth operation of resonators, as the coupling can be changed to account for dispersion as long as the waveguide supports the mode, and the mode does not suffer from bend losses.

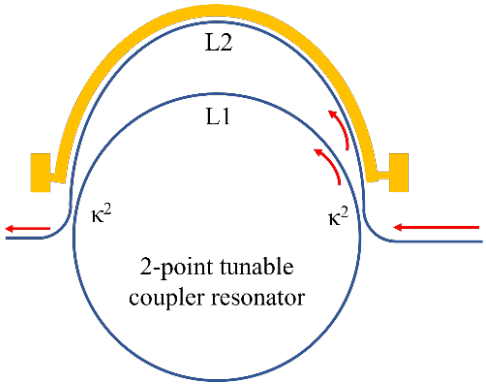

Figure 2.11 2-point coupled resonator schematic: shows a typical two-point coupled device with point couplers having power coupling coefficients κ^2, where the length of the ring arm is L1, and the coupler arm is L2.

The coupling of the MZI coupler is between a minimum value of 0 and a maximum value of.

$$\kappa_{2-point}^2 = 4\kappa^2(1-\kappa^2) \qquad 2.1$$

Assuming that the two-point couplers have the same coupling coefficient κ2 (Figure 2.9), the FSR of the coupler is given as

$$FSR(\lambda) = \frac{\lambda^2}{\Delta L . n_g} \qquad 2.2$$

where n_g is the group index at wavelength λ and the length difference between the arms is ΔL = L1–L2.

The visible two-point coupler devices are designed with R ~ 3.7 mm and κ^2 = 3 MHz, which gives the maximum κ^2_{2point} ~ 50 MHz for λ = 670 – 700 nm with the TM0 mode operation. The FSR of the two-point coupler is 0.12 nm at 698 nm which can be shortened by choosing a longer arm length for one of the arms of the coupler. A smaller FSR enables less tuning power but increases the footprint of the devices. These devices were tested at 698 nm with metal tuners used to tune the coupling and to show the versatility of these devices, which were also tested at 780 nm for the TE0 mode, as shown in Figure 2.10 summarizing the results. The coupling at 698 nm covers all three regimes of coupling, starting at over-coupled operation, with coupling decreasing, reaching critical coupling, and eventually reaching an under-coupled regime as the power continues to increase, as shown in figure 2.12 (a) and (c). Interestingly, the under-coupled regime reveals split resonance with ~ 2 MHz splitting caused by scatterers and is indistinguishable at higher coupling values. The intrinsic loss remains constant for different coupling values; thus, the two-point coupler can also be used to extract losses. As an example of loss extraction, the same resonators are used at 780 nm with TE0, and because the couplers are not designed for this wavelength, the resonators remain under-coupled, but the intrinsic loss is successfully extracted, as shown in Figure 2.12 (b) and (d).

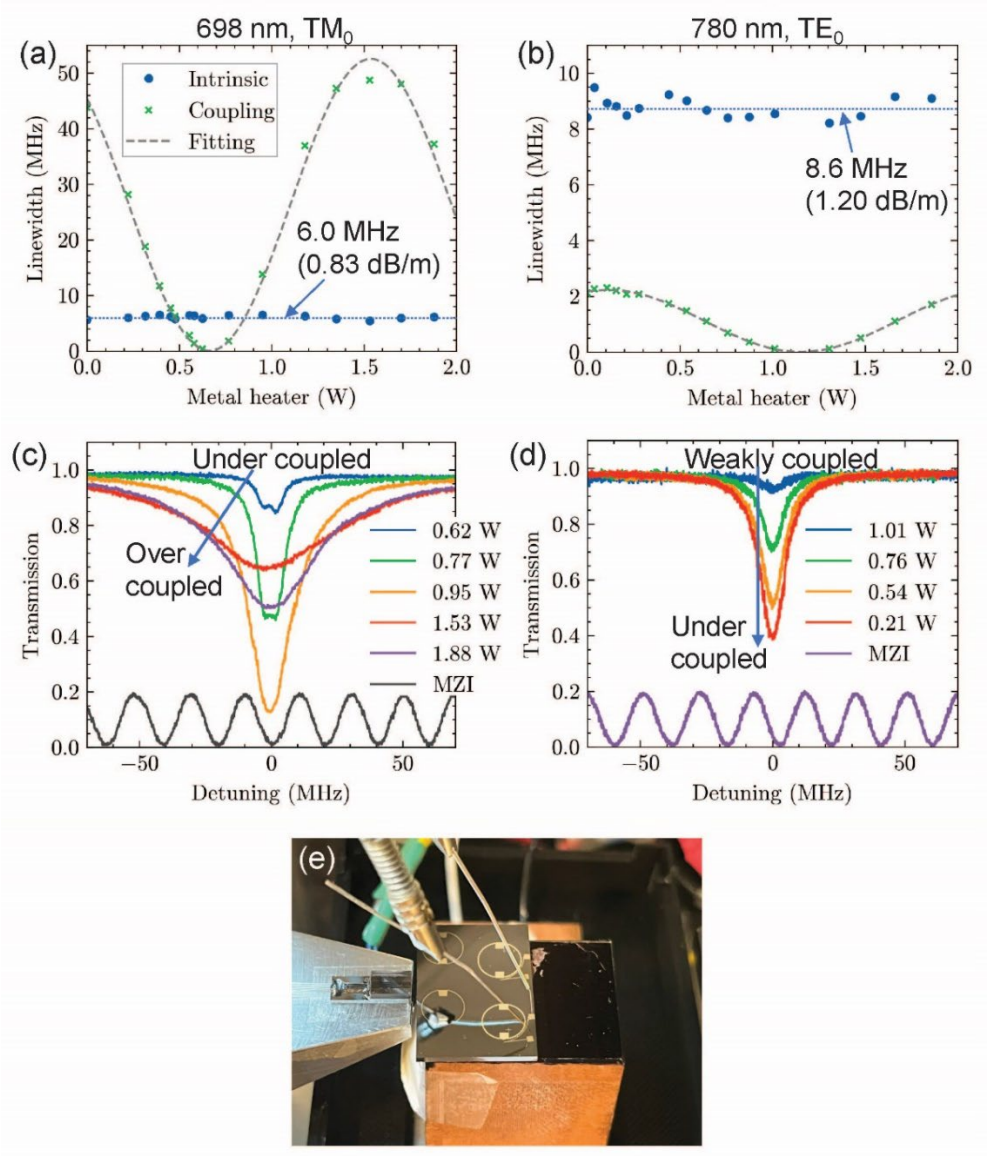

Figure 2.12 2-point coupler resonator test: (a) Measured linewidth of the two-point coupled resonator at 698 nm for TM0 mode showing full FSR tuning and showing that the tuning can achieve fully designed coupling, including achieving a critically coupled operation. These are also used to extract the intrinsic coupling and show the intrinsic coupling (loss of 0.83 dB/m) values unchanged as the external coupling is swept. (b) Measured linewidth at 780 nm, this is not able to achieve critical coupling but is sufficient to extract the intrinsic coupling for the waveguide geometry. (c) Resonance transmissions for the tuning of the 698 nm coupling, which reveals a split resonance of ~ 2 MHz in the under-coupled region, which is otherwise obscured by the larger external coupling for critical coupling and over-coupled operation. (d) Resonance transmission for 780 nm TE0 mode.

2.5 Conclusion

This chapter demonstrates the lowest waveguide losses in the visible and near-IR regions for any waveguide platform reported to date. The reported losses are between 1 dB/m and 9 dB/m for a single fundamental (TE0) mode operation with Qs for a bus-coupled ring resonator, between ~10 million and 60 million, in the same wavelength range. Further lowering of losses is demonstrated with the losses between 0.36 dB/m and 2.2 dB/m for fundamental TM0 mode operation with the Qs for a bus-coupled ring resonator, between ~40 million and 145 million, in this same wavelength range. These waveguides are CMOS compatible, and TM0 mode devices with the lowest losses are fabricated in a CMOS foundry. These waveguides enable wafer-scale integration platforms for multiple visible wavelengths and open the possibility for on-chip components such as delay lines, switches, modulators, Brillouin lasers, reference cavities, and tunable lasers [98] to support visible-light AMO applications including quantum, atom, ion, and molecule transitions. The low absorption limited loss at 674 nm (0.17 dB/m, <15% of the total loss for the TE0 mode) shows the potential to further improve these results by advanced fabrication processes that reduce the roughness of sidewalls [24]. There are opportunities to further reduce the loss to below 0.1 dB/meter and Q to greater than 300 million by employing nitride surface passivation and blanket nitride deposition techniques [24]. These results represent a significant step forward in visible-light wafer-scale photonic integration platforms, opening a wide range of potential applications that utilize atoms, ions, and molecules, including sensing, navigation, metrology, and clocks. Table 2.1 summarizes the loss and Q factors of all the waveguide configurations discussed in this chapter.

Table 2.1 Waveguide Loss Summary

Lowest loss and highest Q TM0 mode				
	493 nm	**674 nm**	**698 nm**	**780 nm**
Waveguide Width	1 μm	2.3 μm	2.5 μm	4 μm
Critical Bend Radius	1 mm	3 mm	3 mm	3 mm
Propagation loss	2.11 dB/m	0.6 dB/m	0.51 dB/m	0.36 dB/m
Qi	39 million	94 million	114 million	145 million
Low loss TE0 20 nm core				
	461 nm	**674 nm**	**698 nm**	**802 nm**
Waveguide Width	1.3 μm	2.3 μm	2.3 μm	2.3 μm
Critical Bend Radius	0.33 mm	2.3 mm	3 mm for TE0	5.5 mm
Propagation loss	9 dB/m	1.1 dB/m	1 dB/m	1.8 dB/m
Qi	9.5 million	54.4 million	60 million	27.7 million
Higher confinement cores				
	461 nm	**674 nm**	**780 nm**	**802 nm**
Core thickness	90 nm	90 nm	120 nm	90 nm
Mode used	TE0	TE0	TM0	TE0
Waveguide Width	300 nm	400 nm	900 nm	400 nm
Critical Bend Radius	100 μm	100 μm	750 μm	200 μm
Propagation Loss	~5.0 dB/cm	~0.24 dB/cm	2.4 dB/m	~0.13 dB/cm

Chapter 3: Visible integrated Brillouin lasers for low fundamental noise

3.1 Introduction

Highly coherent visible-light lasers provide the spectral purity required for precision atomic, molecular, and optical (AMO) physics such as quantum computing and sensing [15,99,100], atomic clocks [15,101], and atomic and molecular spectroscopy [102–104], as discussed in Chapter 1. Traditionally, the low-phase noise and high-frequency stability needed to address narrow optical transitions in atoms, ions, and molecules [60,105] is provided by the use of macroscopic laser systems locked to large, high-finesse, low-drift optical reference cavities in conjunction with vapor cells. These provide state-of-the-art performance [15,34,106] but are lab-scale systems that pose challenges for atomic and molecular experiments of ever-growing complexity and for portable, integrated, or even autonomous optical clocks. There is a need for visible wavelength lasers that are smaller and more reliable so that experiments can scale the number of wavelengths, atoms, or molecules, and complexity in general by reducing the size, weight, and power (SWaP) of the optical sources. Photonic integration provides a path to miniaturize these laser systems and improve their reliability [10,107,108], reduce sensitivity to environmental disturbances, and enable systems with a larger number of entangled atoms [109,110], higher sensitivity quantum sensors [99,111], higher precision positioning, timing, and navigation [112], and probing of complex molecules [113–118].

Stimulated Brillouin scattering (SBS) lasers with pump linewidth narrowing properties and ultralow phase noise emission [1] are promising candidates for AMO physics and quantum applications. SBS emission in the visible region has been achieved with fiber-optic-based resonators, exotic fibers, and bulk optical implementations [119–125]. Recently, the coherence of a near-infrared (NIR) fiber SBS laser was transferred to the visible region to address the clock transition of strontium; however, this work required bulky, power-inefficient, nonlinear frequency conversion [126]. To reduce system complexity and power requirements, and improve reliability, it is desirable to use a "direct drive" approach, where the SBS laser directly emits at the desired visible wavelength, without intermediate conversion stages. Chip-scale SBS lasers operating in the NIR have exhibited impressive performance [74,127–134], achieving sub-Hz fundamental linewidth [74], 30 Hz integral linewidth over 100 ms, and 2×10^{-13} fractional frequency stability [135], and more recently, impressive sub 100 mHz fundamental linewidth (FLW) performance [134] in a cascading inhibited SBS. To date, visible light emission in a photonic-integrated SBS laser has not yet been achieved. This lack of progress has been primarily due to barriers such as realizing ultra-low loss Brillouin-active planar waveguides in the visible region, leading to inefficient Brillouin scattering, and preventing SBS lasing in the desired operating regime of long photon guiding lifetime, short phonon guiding lifetime, large resonator photon lifetime, and large resonator mode volume [74,136]. Overcoming these barriers, as well as realizing a visible light SBS laser in a wafer-scale integration platform, will lead to reduced size and cost, improve stability and robustness to environmental disturbances, and enable experiments and applications with an increasing number of stable lasers and wavelengths, such as multi-qubit quantum computers in trapped ions and cold atoms [46,137].

This chapter demonstrates visible light stimulated Brillouin scattering (SBS or Brillouin) lasers and visible light spontaneous Brillouin scattering in a photonic integrated waveguide structure. These lasers are ring-bus resonator design fabricated using low loss waveguides described in Chapter 2. Brillouin lasing in TE0 mode at λ = 674 nm is demonstrated with a 14.7 mW optical threshold, a 45% slope efficiency, and 9.28 mW on-chip output power for the first order Stokes (S1) with linewidth narrowing to 269 Hz as the pump power is increased from below threshold up to the second order Stokes (S2) emission threshold. The record-low waveguide losses discussed in Chapter 2 (~ 1 dB/m) and record-high Q (60 million) at λ = 674 nm in TE0 single-mode waveguides enable this SBS laser to operate in a 2.68×10^4 μm^3 mode volume resonator. To measure the visible-light Brillouin gain spectrum in a photonic waveguide, detection of the extremely weak spontaneous Brillouin gain backscattered signal is enabled without the benefit of stimulated gain measurements. Traditional real-time pump-probe stimulated Brillouin gain measurements were difficult to perform due to the absence today of 26 GHz phase modulators that operate at λ = 674 nm, 698 nm and 1348 nm semiconductor sources that can be frequency doubled without filtering out the sideband. An accurate prediction of the ~ 26 GHz Stokes frequency shift was performed using a multiphysics simulation, and the Stokes shift was measured by time-averaged heterodyne Brillouin spectroscopy between the pump and backscattered signal [7,138]. A 25.110 GHz first order Stokes frequency shift and 290 MHz gain bandwidth were measured and accurately predicted by the simulations. The simulations predicted a peak Brillouin gain of 2.73 $(W\ m)^{-1}$. The gain measurements guide the laser ring-bus resonator design, with a 3.587 GHz free spectral range (FSR) equal to one-seventh of the 25.110 GHz

S1 frequency shift. To highlight the versatility of this laser, SBS lasing at λ = 698 nm using the same waveguide materials and design, with mask-only changes, is also demonstrated, but exhibits a high threshold from imperfect phase matching.

To reduce the threshold of the lasers and enable operation right below S2 emission where the S1 linewidth is narrowest, this chapter presents smaller radius and lower loss TM0 mode emission SBS resonators. TM0 SBS resonators with SBS lasing S1 threshold of 9 mW at λ = 674 nm, 6.6 mW for λ = 698 nm and 0.8 mW at λ = 780 nm are demonstrated. This first sub-mW threshold is made possible by the first < 1 dB/m loss and > 100 million Q at λ = 780 nm, as reported in Chapter 2. The λ = 698 nm SBS laser has a 6.6 mW threshold, a factor of 10x reduction over previous integrated SBS resonators and a 7.8 Hz fundamental linewidth, a factor of >500x reduction in FLW. The λ = 780 nm and 778 nm SBS laser have a 0.8 mW S1 threshold a 20 Hz fundamental linewidth a >2500x reduction in FLW. The 674 nm TM0 SBS laser has a lower 10 mW S1 threshold and 12 Hz FLW, a >3500x reduction in FLW. These SBS lasers also lower the integral linewidths by over an order of magnitude, with 1/π ILW of S1 3.6 kHz, down from 57 kHz for free running at λ = 698 nm, 6 kHz, down from 121 kHz for free running at λ = 674 nm and 1.4 kHz down from 160 kHz for free running at λ = 780 nm. The 674, 698, and 780/778 nm wavelengths were chosen to highlight their applicability in ion qubit, neutral strontium clock, and Rb two-photon clock transitions, respectively. The cascaded emission of the third Stokes tone (S3) was also demonstrated at λ = 780 nm. The SBS laser devices at λ = 780 nm were fabricated in both, 8” CMOS foundry as well as UCSB research cleanroom. Parts of this chapter have been adapted with permission from our previous publications [7,138].

3.2 SBS lasers

3.2.1 Introduction to SBS lasing in weakly guiding Si_3N_4 waveguides

The SBS process in the weakly guiding Si_3N_4 waveguides is closer to the SBS in the fibers and results from the annihilation of a long lifetime guided photon into a Stokes shifted guided photon and bulk like dissipative phonon in the presence of phonons [74,136]. The process is initiated by thermal phonons, and as the pump power increases, the generation of Stokes photons generates more phonons, which further strengthens the moving grating of phonons, facilitating further Brillouin scattering, and hence stimulated emission. The short photon lifetime results in a low peak gain and a wide bandwidth Brillouin gain spectrum, which is responsible for linewidth suppression in the Stokes tone [1]. The pump, Stokes and the phonon must satisfy the momentum and energy conservation, which are given by:

$$\boldsymbol{\omega_s = \omega_p - \Omega} \quad \text{and} \quad \boldsymbol{k_s = k_p - q} \tag{3.4}$$

where ω_s, ω_p and Ω are the frequencies and k_s, k_p, and q, are the wavenumbers of the Stokes, pump and the phonons respectively. Equation 3.1 is also called Brillouin phase matching condition and is shown in Figure 3.1 (a) shows the phase matching condition and associated resonator free spectral range (FSR) design, Figure 3.1 (b) shows the Brillouin process in the weakly confining Si_3N_4 waveguides.

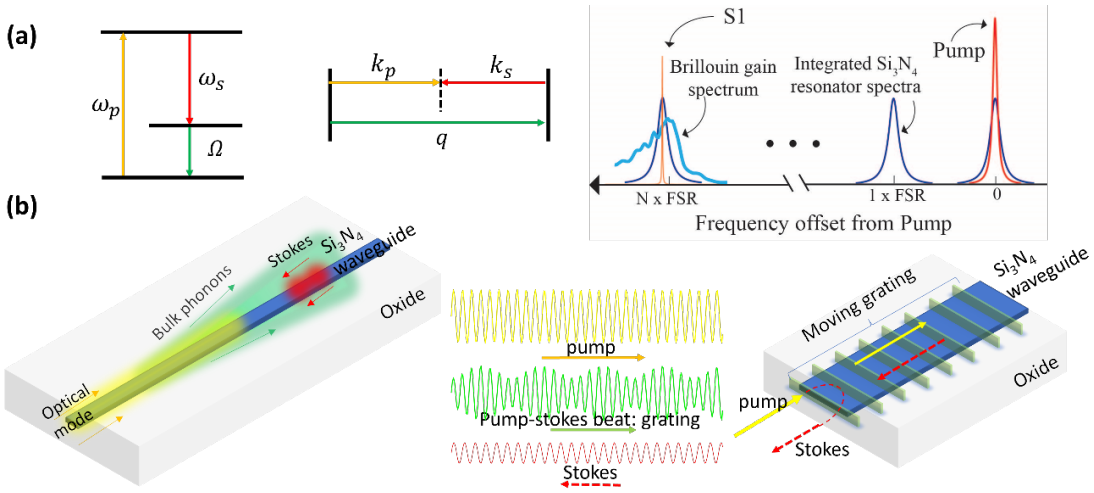

Figure 3.1 Brillouin lasing overview: (a) Energy conservation, phase matching of wave vectors, phase matching design for resonators. (b) Schematic of guided photonic mode, un-guided bulk like phonons interacting to produce moving grating that produces backward propagating Stokes tone.

3.2.2 Multiphysics simulation of Brillouin scattering

To simulate the Brillouin gain spectrum, we used finite element solvers to obtain the optical modes of the SBS laser resonator and then used these modes to construct electrostrictive forces and determine the mechanical response of the system to these time-harmonic forces [2]. Using an argument based on the Manley-Rowe relations, we obtain the Brillouin gain ($G_{\mathrm{B}}(\Omega)$) from the dissipated mechanical power when the system is driven by electrostrictive forces:

$$G_{\mathrm{B}} = \frac{1}{\delta z}\frac{\omega_{\mathrm{S}}}{\Omega}\frac{1}{P_{\mathrm{p}}P_{\mathrm{S}}}\int d^3x\langle \mathbf{f}\cdot\dot{\mathbf{u}}\rangle \qquad 3.2$$

where ω_{S} and Ω are the angular frequencies of the Stokes and phonon modes respectively, δz is the length of the waveguide, P_{p} (P_{S}) is the power in the pump (Stokes) modes used to construct the optical forces, $\mathbf{u}$ is the elastic displacement, and $\mathbf{f}$ is the electrostrictive force density. The dissipated mechanical power is represented here as the volume integral of the

time-averaged power $\int d^3x\langle \mathbf{f}\cdot\dot{\mathbf{u}}\rangle$. To obtain the electrostrictive force, the photoelastic tensor (p_{ijkl}) and the optical mode components are combined to give the i_{th} component of the force density given by

$$f_i = \frac{1}{4}\epsilon_0 \partial_j n^4 p_{\text{ijkl}}(E_{p,k}E^*_{S,l} + E_{p,l}E^*_{S,k}) \tag{3.3}$$

where $E_{p,k}$ and $E_{S,k}$ are the k^{th} components of the pump and Stokes electric fields, respectively. In addition to providing the magnitude, bandwidth, and peak of the Brillouin gain, these simulations provided insights into the spectrum structure. For example, our simulations show that phonon interference with the air-cladding boundary explains the modulation of the gain spectrum with frequency, as shown in Figure 3.2.

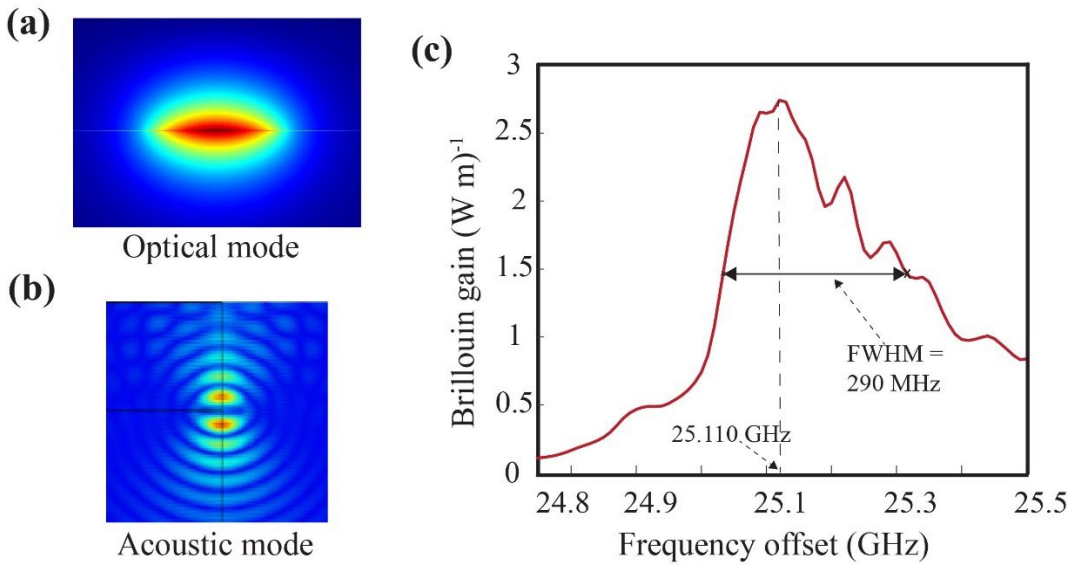

Figure 3.2 Brillouin gain simulation: (a) Mode profile of optical mode in waveguide. **(b)** Continuum of non-guided, bulk-like acoustic modes. **(c)** Simulated spontaneous Brillouin scattering spectrum. The reflection of acoustic modes from the top cladding is responsible for the smaller peaks in the high frequency offset tail of the Brillouin gain spectrum.

3.2.3 SBS lasing power dynamics

We use the simplified coupled mode approach to model the intracavity photon number dynamics and the equations of motion for the optical field amplitude are given by [139]

$$\dot{a}_m = -\left(\frac{\gamma}{2} + \mu|a_m + 1|^2 - \mu|a_m - 1|^2\right) a_m + \sqrt{\gamma_c} F_{pump} \delta_{m0} \tag{3.4}$$

where the total loss rate, $\gamma = \gamma_{in} + \gamma_c$, is the sum of the intrinsic and coupling loss rates, μ is the Brillouin amplification rate per pump photon, and $F_{pump} = \sqrt{P_{pump}/h\nu}$ is the photon influx field amplitude. The Brillouin amplification rate μ of the SBS resonator is a function of Brillouin gain factor and resonator parameters,

$$\mu = \frac{h\nu v_g^2 G_{\mathrm{B}}}{2L} \tag{3.5}$$

where $G_{\mathrm{B}} = g_{\mathrm{B}}/A_{\mathrm{eff}}$ is the Brillouin gain factor, g_{B} is the bulk Brillouin gain and L is the resonator roundtrip length. From equation 3.4, we can find the threshold power for S1,

$$P_{\mathrm{th}} = \frac{h\nu\gamma^3}{8\mu\gamma_{\mathrm{c}}} \tag{3.6}$$

and the threshold power for S2 and S3 are $4P_{\mathrm{th}}$ and $8P_{\mathrm{th}}$.

The fundamental linewidth for S1 before its clamping is found to be,

$$\delta\nu_1 = \frac{\mathrm{n}_0\gamma}{4\pi|\mathrm{a}_1|^2} \tag{3.7}$$

and it reaches its minimum at the S1 clamping point,

$$\delta\nu_1(4P_{\mathrm{th}}) = \frac{n_0\mu}{2\pi} \tag{3.8}$$

where $n_0 = k_m T/(\hbar\Omega)$ is the thermal occupation number of the acoustic mode.

The acoustic frequency is given by

$$\Delta\nu_a = \frac{2n_{eff}v}{\lambda_p} \tag{3.9}$$

Where $\Delta\nu_a$ is the acoustic frequency, v is acoustic velocity, n_{eff} is waveguide pump mode effective index and λ_p is pump wavelength.

As an example of the implementation of the above model, the TE0 mode case is calculated and simulated for λ = 674 nm with the acoustic frequency 25.110 GHz, n_0 at room temperature is estimated to be ~1300. From the measured on-chip threshold power of 14.7 mW, the resonator intrinsic linewidth of 8.0 MHz, the resonator coupling linewidth of 8.0 MHz, the resonator mode area of 3.0 μm^2 and the ring radius of 8.95 mm, we estimate the Brillouin gain rate μ to be 50.7 mHz (the corresponding Brillouin gain GB of 0.49 (W m)$^{-1}$) using equation 3.3 and equation 3.4 and the minimal fundamental linewidth of S1 to be 2.0 Hz using equation 3.5, shown in Figure 3.2. This estimated Brillouin gain GB of 0.49 (W m)$^{-1}$ is close to the simulated GB of 1.03 (W m)$^{-1}$ at the Brillouin shift frequency of 25.036 GHz (imperfectly aligned FSR from the Brillouin shift of 25.11 GHz) from the full COMSOL opto-mechanics simulation in Figure 3.3, showing a rough agreement between experiment and physics simulation. The theoretical S1 threshold of 7.0 mW assuming our simulated G_B of 1.03 (W m)$^{-1}$ is also close to the measured threshold of 14.7 mW.

Slope efficiency is defined as the fraction of pump photons converted to Stokes photons above the threshold. By modeling the laser emission, we find that the conversion efficiency, defined as the ratio between the S1 output power and pump power, is

$$\eta = 2\left(\frac{\gamma_c}{\gamma}\right)^2 \tag{3.10}$$

where γ_c is the bus-ring coupling loss rate and $\gamma = \gamma_{in} + \gamma_c$ is the total loss rate (sum of the coupling rate and waveguide loss rate). This means that the slope efficiency is 50% in critically coupled resonators, and any deviation from critically coupled towards undercoupled ($\gamma_{in} > \gamma_c$) will decrease the slope efficiency for all pass ring resonators like ours. The slope

efficiency can be increased by designing overcoupled resonators ($\gamma_{in} < \gamma_c$) at the cost of increased threshold power (equation 3.6) for lasing. Thus, we chose critically coupled resonators as a compromise between the threshold and slope efficiency for SBS lasing in an all pass resonator.

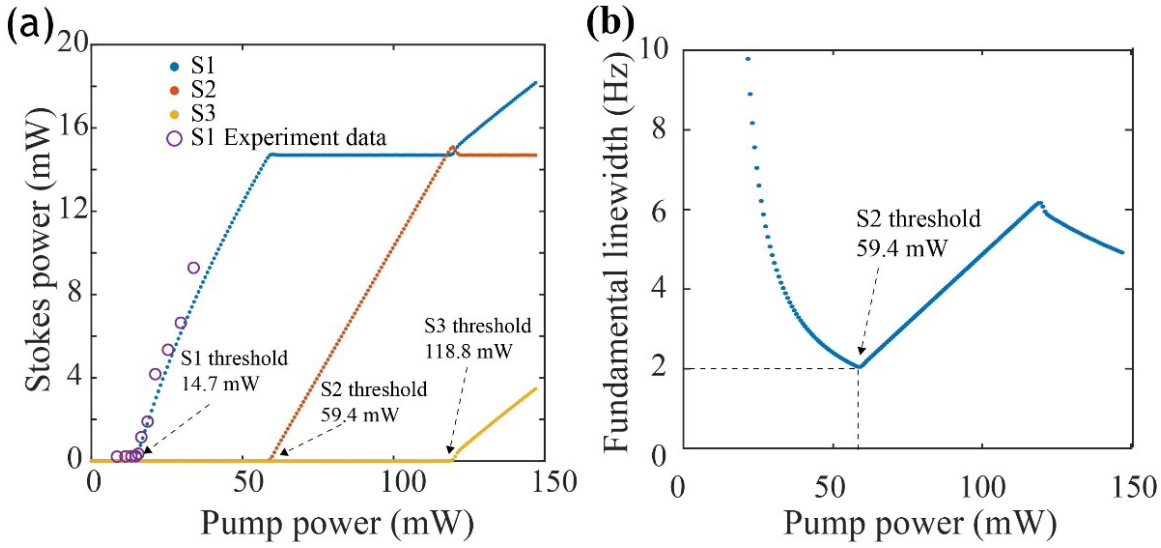

Figure 3.3 SBS lasing Stokes power and FLW modelling: (a) Modeled Stokes power for on-chip power in the range of 0-150 mW. (b) Simulated fundamental linewidth of the first Stokes tone as a function of on-chip power, assuming no crosstalk from the pump. The fundamental linewidth decreases until the S2 threshold is reached.

3.3 SBS in TE0 mode waveguides

3.3.1 Spontaneous Brillouin gain spectrum measurement

To measure the spontaneous Brillouin scattering, we used the experimental setup shown in Figure 3.4 (a). A 15 mW $\lambda = 674$ nm (free space) cavity-stabilized laser was passed through a tapered semiconductor optical amplifier, providing 120 mW of in-fiber power. Figure 3.4 (b) shows the coupling of 674 nm pump light into our 2 m spiral. After facet and fiber losses, the pump power injected into the spiral was reduced to ~30 mW. The backscattered light from the chip passes through a circulator used to recover spontaneously scattered Stokes light, where it is mixed with the pump laser on a fast photoreceiver for heterodyne detection. The detected signal was amplified and measured using an electronic spectrum analyzer (ESA).

The spontaneous Brillouin scattering measurements and simulations are shown in Figure 3.4 (c). Owing to the small amplitude of the spontaneous scattering signal, systematic effects within the apparatus must be carefully removed. The background of the apparatus was characterized by performing measurements at low optical powers, where Brillouin scattering was strongly suppressed. The difference between the spectra measured at high powers, where Brillouin scattering is appreciable, and the apparatus background isolates the scattered signal (Figure 3.4 (c)). We first measured the signal from the spiral chip, which showed prominent Brillouin peaks, and then repeated the measurement at the same power, but with the chip removed. In addition, an average of over 20 ESA traces was used to reduce the measurement noise. A prominent peak is observed near 24.8 GHz, which is produced by the optical fiber, whereas the observed peak at 25.11 GHz closely matches the simulated spontaneous Brillouin

spectrum. We attribute the high degree of skewness of spontaneous scattered spectrum towards high frequencies to unguided acoustic waves coupling into the silica cladding, which is consistent with simulations.

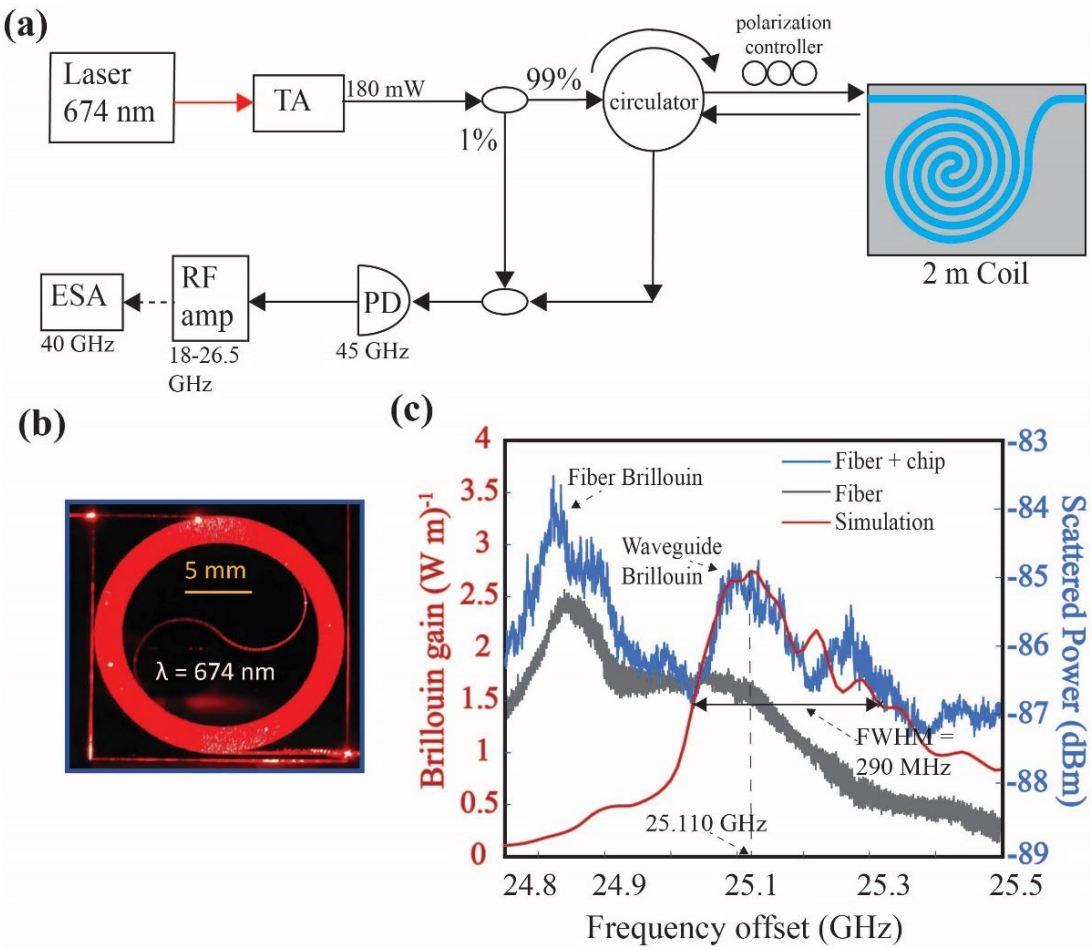

Figure 3.4 Waveguide design and 674 nm spontaneous Brillouin measurement: (a) 2 meter single mode waveguide spiral used for the spontaneous Brillouin gain measurement. (b) Photograph of the actual 2 meter spiral shown while illuminated with 674 nm light. A 5 mm scale is shown for reference. (c) Measured and simulated spontaneous Brillouin gain with a 25.110 GHz first order Stokes (S1) frequency shift, 2.73 $(W\ m)^{-1}$ gain peak, and 290 MHz bandwidth. The resolution bandwidth (RBW) of electrical spectrum analyzer (ESA) was set at 100 Hz. The measured blue curve shows the Brillouin contribution from both the fiber and silicon nitride waveguide, while the grey trace shows contribution from only the fiber, which confirms that the peak at 25.110 GHz is due to the waveguide spontaneous Brillouin scattering.

3.3.2 SBS resonator design

The SBS laser resonator is based on an ultra-low loss single mode Si_3N_4 core and SiO_2 cladding waveguide that is designed to operate at 674 nm and 698 nm. The waveguide consists of a 20 nm tall and 2.3 μm wide silicon nitride core deposited and etched on a lower thermally grown oxide cladding on a silicon substrate, with a TEOS-PECVD deposited upper cladding [88] (cross-section shown in Supplementary Fig. 4), and a final two-step annealing at 1050 °C for 7 h and 1150 °C for 2 h, which is the optimized annealing process for our waveguides. To maximize the spontaneous Brillouin signal, a 2 meter on-chip, in-out spiral is fabricated with ~ 1 dB/m loss and the extremely small $\sim 10^{-12}\, W$ (spectrum analyzer resolution bandwidth of 100 Hz) spontaneous Brillouin signal is measured to obtain the exact Brillouin gain spectrum at 674 nm.

The SBS resonator is designed to phase-match with the Brillouin gain peak. The SBS laser resonator has R = 8.9509 mm for 674 nm and R = 9.4268 mm for a 698 nm bus-coupled ring structure with a free-spectral range (FSR) designed to be 1/7 of the measured 25.110 GHz peak Stokes shift at 674 nm (Figure 3.5) and a bus-to-ring power coupling coefficient [74] κ^2 of ~1.5%. The ring is designed to have multiple FSRs per Brillouin Stokes frequency shift to facilitate the alignment of the Stokes shift and cavity resonance, increase the cavity volume, and provide robustness to fabrication variations [74]. A high intrinsic Q of 55.4 million and loaded Q = 27.7 million at 674 nm were achieved (Figure 3.5), and the coupling coefficient was also measured independently with coupling coefficient test structures. These devices were fabricated on a 4” wafer at UCSB cleanroom.

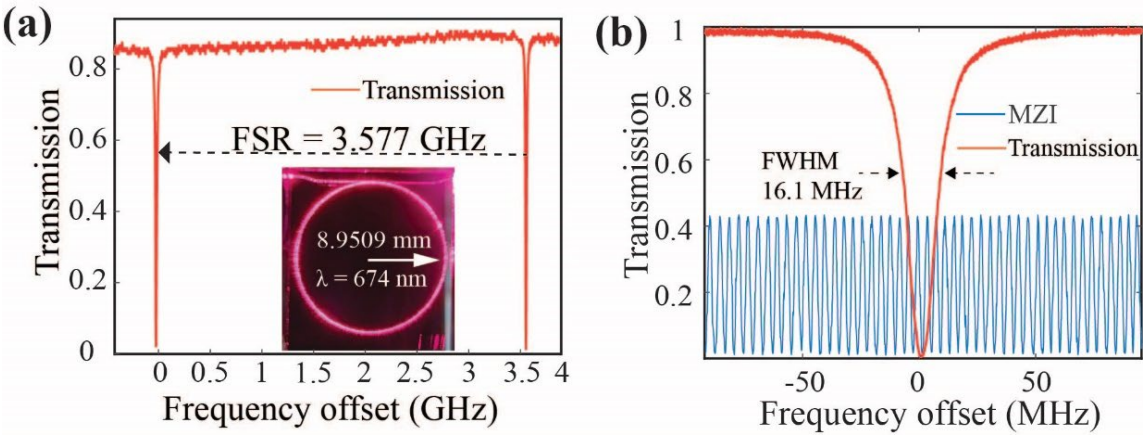

Figure 3.5 Stimulated Brillouin scattering (SBS) resonator design, FSR and quality factor: (a) Measured resonator free spectral range (FSR) = 3.577 GHz at 674 nm for the R = 8.9509 mm, image of device coupled with laser in the inset. (b) Quality factor (Q) measurement (red trace) performed using radio frequency (RF) calibrated unbalanced Mach-Zehnder interferometer (MZI) (blue trace). The full width at half maximum (FWHM) linewidth = 16.1 MHz loaded Q = 27.7 million and intrinsic Q = 55.4 million and loaded Q = 27.7 million at 674 nm.

3.3.3 SBS laser characterization

The SBS laser resonator is pumped by an off-chip tapered optical amplifier (TA) that is seeded with 674 nm light from a continuous-wave (CW) external-cavity diode laser. The TA output was coupled to the waveguide SBS resonator using a high-power fiber circulator. A maximum of ~35 mW on-chip power is delivered to the waveguide bus, limited by a 180 mW TA maximum output power and ~4 dB fiber-to-facet coupling loss. The backward-propagating S1 signal was measured using a 3-port fiber optic circulator. The measured and simulated S1 powers are plotted against the pump power in Figure 3.6 (a). A clear S1 threshold was observed for an on-chip pump power of 14.7 mW corresponding to a threshold density of

4.92 mW μm^{-2}, and a 45% slope efficiency was measured, which is in good agreement with our SBS model [139].

In addition to verifying the laser threshold, a decrease in the S1 emission linewidth as the pump power is increased from below the threshold, through the threshold, and above the threshold [74,140] has been demonstrated to verify SBS lasing. Below the threshold, the optical power spectrum was measured using a heterodyne beat note produced by mixing the backward-propagating S1 with the pump on an ESA. To minimize the contribution of the pump linewidth to the measured beat note, the pump laser was locked into a commercial high-finesse ultra-stable cavity (Stable Laser Systems^{TM}). Well below threshold Figure 3.6 (b) (i), the scattered light is produced by uncorrelated spontaneous scattering from thermal phonons and is linearly filtered by the cavity resonance which is approximately 16.1 MHz. As threshold is approached, the spontaneous emission spectra, point (ii) in Figure 3.6 (b), measures FWHM at 12.0 MHz, indicating the onset of stimulated emission, since the emission spectra is narrower than the cold-cavity resonance FWHM.

At just above threshold Figure 3.6 (b) (iii), a dramatic 100x narrowing of the linewidth to 120 kHz as stimulated Brillouin scattering dominates the emission is observed. At all points above the threshold, the frequency noise of S1 was measured using an optical frequency discriminator (OFD), as shown in Figure 3.6 (e). The fundamental linewidth ($\Delta\nu$) is defined [74,130] as the far-from-carrier white frequency noise floor, in Hz^2Hz^{-1}, multiplied by π. In Figure 3.6 (c), the noise floor for each pump power input is indicated by horizontal dashed lines (iii) – (vi). As the pump power increases beyond S1 threshold, the fundamental linewidth drops dramatically from 1.1 kHz (iv) to 269.7 Hz (vi). These linewidth results are

summarized in Figure 3.6 (d), indicating the integral linewidths for points (i) – (ii) below the threshold and the fundamental linewidths for the frequency noise curves in (iii) – (vi) in Figure 3.6 (c). We were not able to provide the required on-chip pump power, 59.4 mW, to achieve lasing of the second-order Stokes (S2) for these TE0 mode SBS lasers.

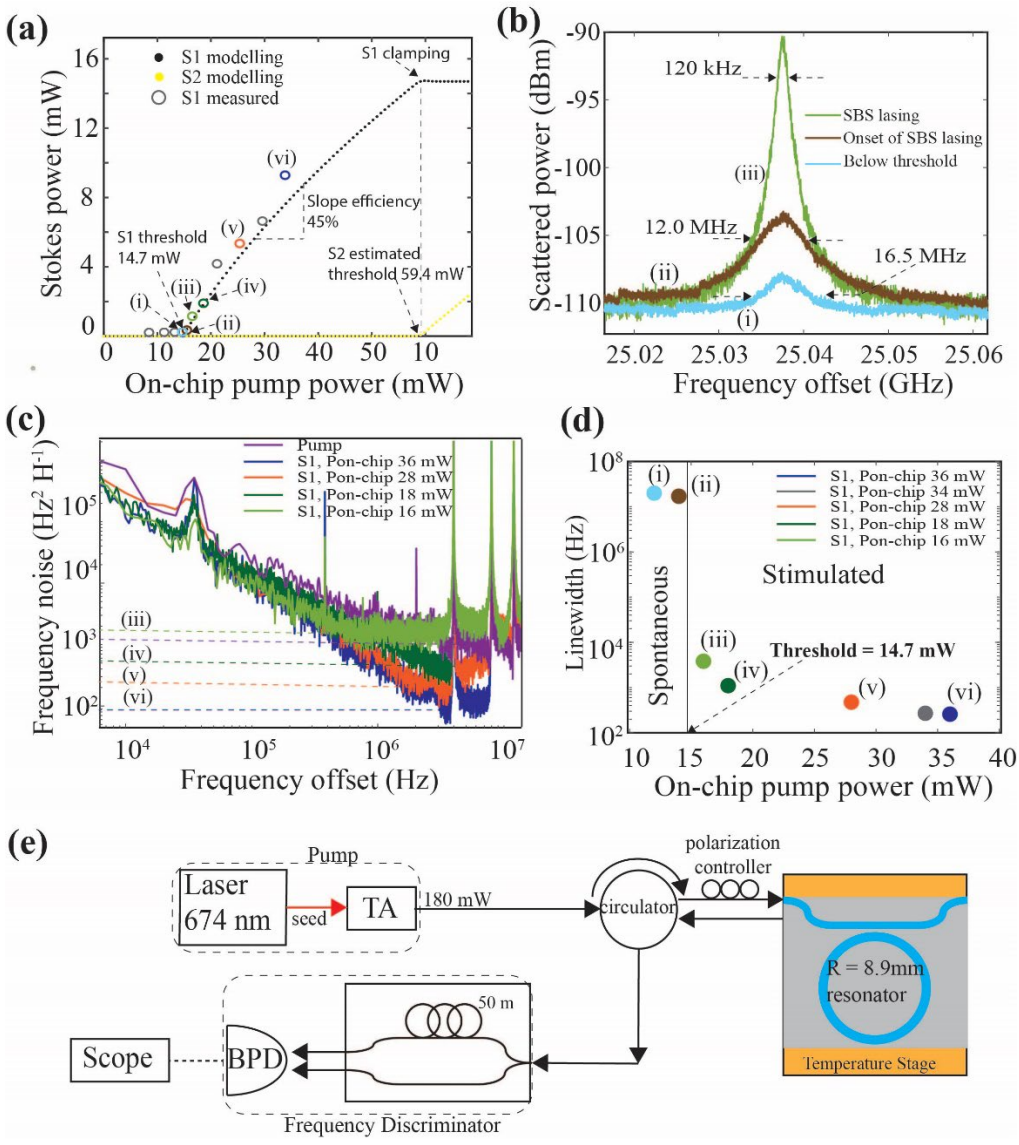

Figure 3.6 674 nm TE0 SBS laser measurements: (a) pump optical on-chip power ($P_{on\text{-}chip}$) vs. first-order Stokes (S1) signal power. The measured S1 laser threshold was 14.7 mW, corresponding to a threshold density of 4.92 mW μm^{-2} and a 45% slope efficiency. Modelling the S1 optical power (black dots) accurately predicts the measured S1 optical power as the pump power is increased from

below to above the threshold. The predicted second-order Stokes (S2) threshold is ~60 mW (yellow dots). **(b)** Measurement of S1 emission linewidth plotted on a logarithmic scale, below the threshold (blue trace), just below the threshold (brown trace), and just after the threshold (green trace). The Brillouin emission linewidth evolves from a spontaneous dominated linewidth of 16.5 MHz, which is approximately the SBS gain filtered by the cold-cavity resonator linewidth of ~16 MHz, to the onset of stimulated Brillouin, measuring a 12 MHz linewidth just below threshold, to a stimulated dominant 120 kHz linewidth just above threshold. The resolution bandwidth (RBW) of the electrical spectrum analyzer (ESA) was set to 1 kHz. **(c)** Frequency noise measurements of S1 using a radio frequency (RF) calibrated fiber optic Mach-Zehnder interferometer (MZI) frequency discriminator. The S1 emission fundamental linewidth for each pump input condition, shown in (c), is indicated by the corresponding horizontal dotted line. The free-running pump frequency noise (purple trace) corresponds to an unlocked pump (i.e., not locked to the stable cavity or SBS resonator). As the pump is increased, a decrease in fundamental linewidth (curves ii to v) is measured. Since the back reflected pump is not optically filtered before frequency noise discrimination, there is a pump noise contribution to the measured frequency noise of S1. Just above the threshold, the conversion from pump to S1 is low, and the white noise floor at the 16 mW pump (green) is a combination of pump, S1, and their beat note. As the on-chip pump power (Pon-chip) is increased, the intra-cavity S1 photon number increases while the pump signal is depleted and decreases to below 10 dB of the Stokes for all other FN traces. **(d)** Summary of beat note and fundamental linewidths from (b) and (c). **(e)** OFD setup schematic used for FN measurements.

Demonstration of 698 nm SBS lasing. A 698 nm SBS resonator using the same 674 nm waveguide design and geometry, with modifications to the FSR and bus-ring coupling gap. At 698 nm, our multiphysics simulation predicts a 24.243 GHz Stokes shift and 300 MHz Brillouin gain bandwidth (Figure 3.7 (a)). A wavelength of 698 nm was selected to match the neutral Sr atom clock transition. As with the 674 nm laser, the FSR is designed to be one-seventh of the S1 frequency shift, resulting in a 9.4 mm radius resonator design. A 3.4 μm bus-ring coupling gap was chosen to operate the resonator in the under-coupled regime with a power coupling coefficient of ~1%. For the fabricated devices, we measure a 12.7 MHz cavity resonance width, a 60 million intrinsic Q, a 33.8 million loaded Q, and a 3.421 GHz

FSR shown in Figure 3.7 (b) and Figure 3.7 (c). Lasing at S1 was observed by pumping the cavity with a Ti: sapphire laser at the expected pump-Stokes frequency offset, as shown in Figure 3.7 (d). The observed pump is a reflection from the resonator far facet. A pump-S1 heterodyne 23.892 GHz beat note is measured as shown in Figure 3.7 (d) inset. The 351 MHz beat note offset from our simulated shift is most likely due to the slight offset between the Brillouin gain peak and the narrow cavity resonance. The pump laser is free running (i.e., stabilized neither to the resonator nor to a reference optical cavity), and the beat note drifts on the order of 100 kHz over tens of milliseconds. The on-chip pump power was 108 mW and the measured on-chip pump threshold power (P_{th}) was ~ 75 mW.

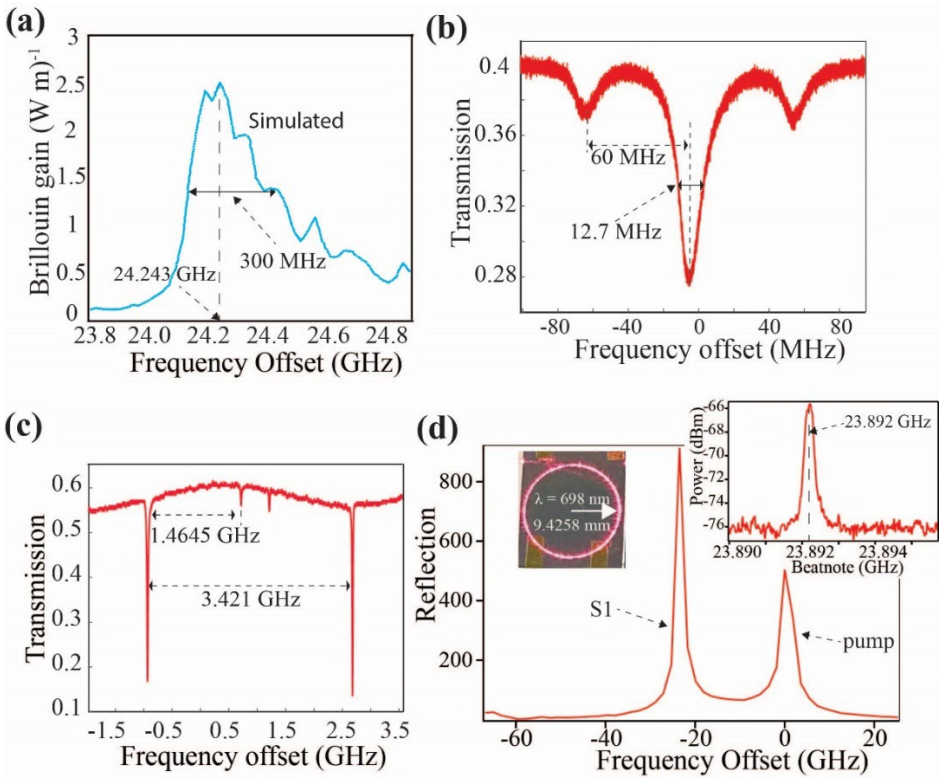

Figure 3.7 698 nm TE0 SBS laser measurements: (a) Multiphysics simulation of waveguide spontaneous Brillouin gain spectra for the pump at 698 nm. The Brillouin gain spectrum width is ~300 MHz and the Stokes frequency shift is 24.243 GHz. (b) The measured full width half maximum (FWHM) resonator linewidth at 698 nm is 12.7 MHz and the measured intrinsic and

loaded Qs are 60 million and 33.8 million, respectively. (c) The resonator free spectral range (FSR) at 698 nm was measured as 3.421 GHz by applying sidebands at 1.4645 GHz. (d) First-order Stokes (S1) and pump measured on an optical spectrum analyzer (OSA); the inset shows the pump-S1 beat note measured at 23.892 GHz on an electric spectrum analyzer (ESA). The inset on the left shows the 9.4 mm radius resonator fiber-coupled with 698 nm pump laser light.

3.4 SBS in TM0 mode waveguides

3.4.1 SBS resonator design

Low sub-dB/m loss TM0 mode waveguides are used to design lower-threshold visible SBS lasers so that they can reach the S2 threshold pump power easily, providing the narrowest linewidth possible in a cascaded SBS laser (Figure 3.3 (b)). The FSR was chosen such that 3x FSR = Brillouin gain shift for 674 nm and 698 nm. For 780 nm, two sets of resonators were designed: one with a 3x FSR = Brillouin gain shift and one with 4x FSR = Brillouin gain shift. To achieve high success of SBS lasing in a single fabrication run, four resonators with slightly offset FSRs were designed so that phase matching can be achieved without the measurements of spontaneous Brillouin scattering, as shown in Figure 3.9 (a). This was also important because the pump lasers at 674 nm and 780 nm did not have sufficient tuning to measure the FSR of the small SBS rings with FSRs > 8 GHz, and the group index was roughly calibrated by measuring the FSR of coil resonators fabricated in a different fabrication process. The 674 nm and 698 nm resonators were also designed with two different coupling schemes: point couplers and two-point couplers. Point couplers provide the simplest design but can only provide a fixed ring-bus coupling, and the fabrication can vary the coupling compared to the simulation owing to changes in the indexes, film thicknesses, and waveguide shrinkage. The

Q measurements are described in Section 2.3.4. The two-point coupler SBS resonators are designed with coupler FSR = 4x Brillouin gain shift so that the S2 coupling will be around the coupling maxima and possibly suppress cascading by increasing the S2 threshold, with the maximum coupling designed to be ~ 50 MHz. Figure 3.8 shows the different designs for the SBS laser, single-ring bus, single-ring bus with included filter ring that can be used to filter out the reflected S1 from the back-reflected pump and eliminate the need for the circulator, two-point coupler resonator, and two-point coupler with a filter ring.

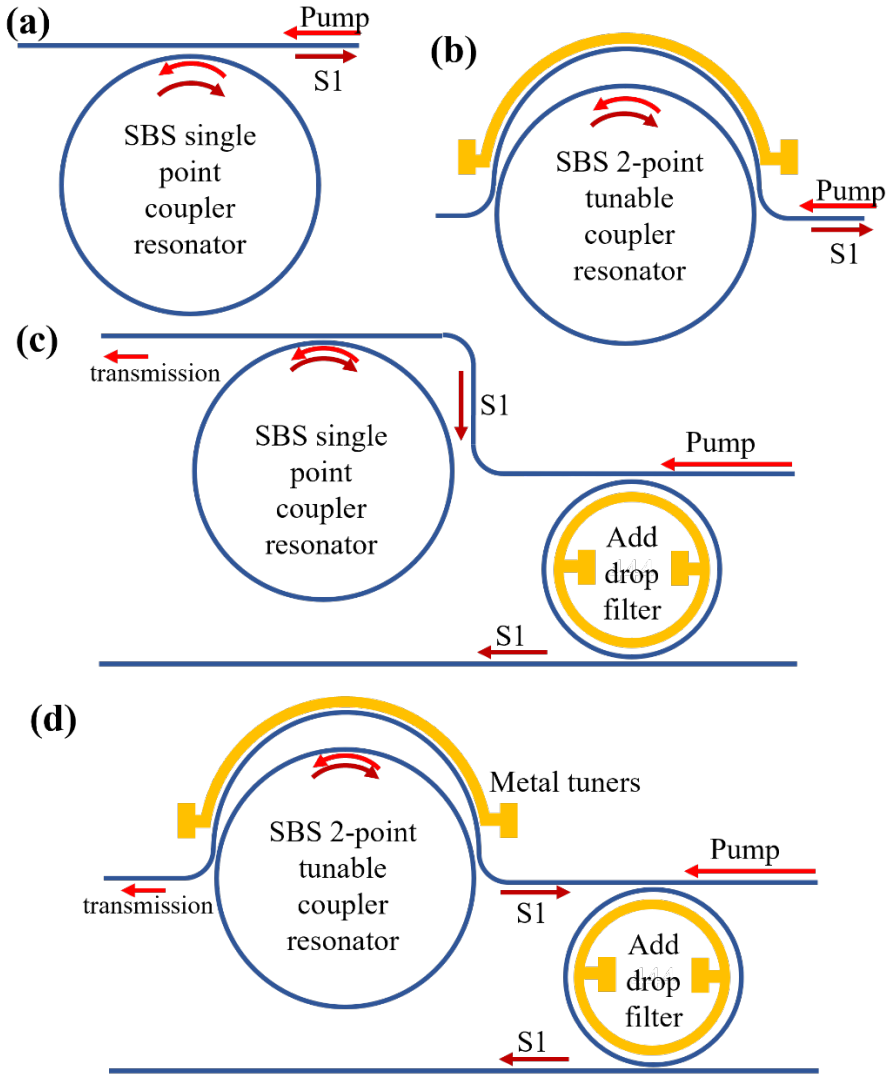

Figure 3.8 Different TM0 SBS laser designs: (a) The simplest design with a through-bus ring resonator requires an external circulator to separate the S1 tone. (b) A 2-point coupler through a resonator allows for fine-tuning of coupling and requires an external circulator. (c) Through ring with single-ring add-drop filter to separate S1 without requiring the external circulator; the filter ring has a different FSR than the SBS ring so that the pump is not resonant, but the Stokes tone is resonant. (d) 2-point coupled SBS resonator with a filter. All the above can also have metal tuners on the SBS ring itself for the modulation of the SBS laser.

674 nm: The calculated Brillouin shift is 25.7 GHz for the TM0 mode with the cross-section described in Section 2.3.1. The rings were designed such that the 3 × FSR matches the Brillouin frequency shift. The designed radii for the rings are R1 = 3.73 mm, R2 = 3.68 mm, R3 = 3.64 mm, and R4 = 3.6 mm. The 3x FSRs for these rings are R1 = 25.2 GHz, R2 = 25.5 GHz, R3 = 25.8 GHz, and R4 = 26.1 GHz. The assumed loss for these devices to design the coupling is 4.5 MHz, but considering these were fabricated in UCSB cleanroom where particles and variations are more than CMOS process, the couplings are set at R1 = 6 MHz, R2 = 9 MHz, R3 = 350 MHz and R4 = 4.5 MHz with R3 designed as 2 point coupler, targeting critically coupled operation. R2 was also designed to have a single ring add drop filter with a radius of 3 mm and couplings of 350 MHz for both the add and drop ports. The measured loss in these rings is much higher than expected, more than double the expected value (from CMOS run) at 1.6 dB/m, Figure 3.9 (e)), increasing the SBS lasing threshold by a factor of four from ideal.

698 nm: The calculated Brillouin shift is 24.9 GHz for the TM0 mode with cross section described in section 2.3.1. The rings were designed such that the 3 × FSR matches the Brillouin frequency shift. The designed radii for the rings are R1 = 3.82 mm, R2 = 3.79 mm, R3 = 3.76 mm, and R4 = 3.72 mm. The 3x FSRs for these rings are R1 = 24.5 GHz, R2 = 24.7

GHz, R3 = 24.9 GHz, and R4 = 25.1 GHz. The assumed loss for these devices to design the coupling is 4.5 MHz, but considering these were fabricated in UCSB cleanroom where particles and variations are more than CMOS process, the couplings are set at R1 = 6 MHz, R2 = 50 MHz, R3 = 50 MHz and R4 = 4.5 MHz with R2 and R3 designed as 2 point coupler, R1 and R4 targeting critically coupled operation. R2 and R3 were designed to have a single ring add-drop filter with a radius of 3 mm and couplings of 500 MHz for both add and drop port. The measured loss in these rings is slightly higher than expected from CMOS run at 0.76 dB/m, Figure 3.9 (d), increasing the SBS lasing threshold by a factor of ~2 from ideal.

780 nm: The calculated Brillouin shift is 21.8 GHz for the TM0 mode with cross section described in section 2.3.1. Two rings are designed such that the 3 × FSR matches the Brillouin frequency shift and the other two such that the 4 × FSR matches the shift. The designed radii for the rings are R1 = 5.84 mm, R2 = 5.8 mm, R3 = 4.41 mm, and R4 = 4.33 mm. The 4x / 3x FSRs for these rings are R1 = 21.7 GHz, R2 = 21.85 GHz, R3 = 21.55 GHz, and R4 = 22 GHz. The assumed loss for these devices to design the coupling is 3-4 MHz, and they were fabricated in the CMOS process, 3-4 MHz without a large split. The measured loss in these rings is record low loss and as expected from the CMOS run at 0.36 dB/m, Figure 3.9 (b). The availability of a frequency doubled widely tunable laser also enabled FSR measurement at 780 nm, which was not possible with the 674 nm and 698 nm SBS resonators. The measured FSR of R1 is shown in Figure 3.9 (c) at 5.52 GHz which gives a 4x FSR at 22.08 GHz. Since it is offset from designed FSR, multiple rings splits show the benefit with R3's measured 3 x FSR = 21.75 GHz matches well with the Brillouin gain offset. In addition, these SBS lasers operate at a bandwidth of over 6 nm with a reasonable threshold owing to the broad Brillouin

gain spectrum, enabling coverage of the relevant Rb wavelengths, such as 778 nm, for two photons with R1 having a lower threshold at 778 nm.

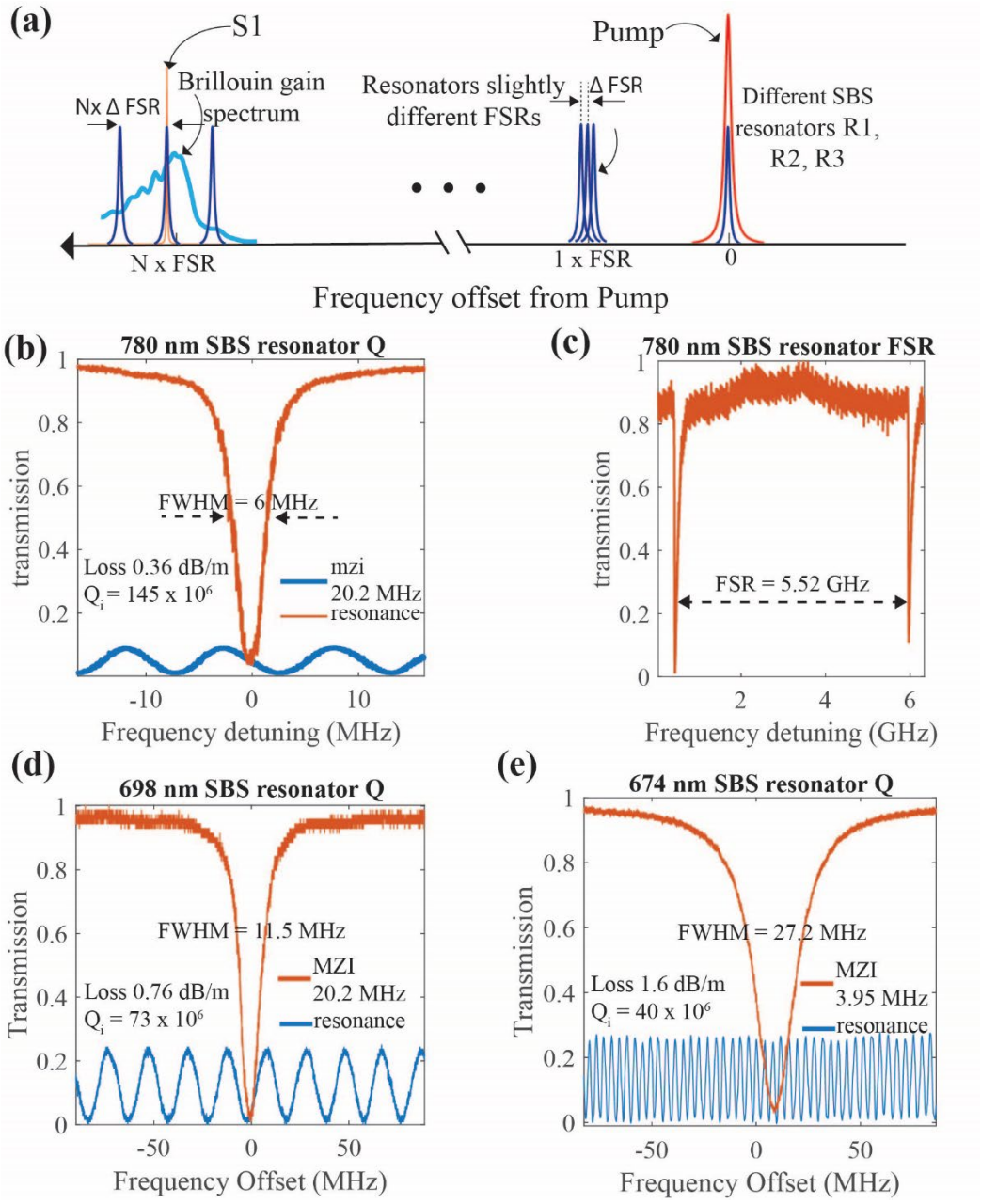

Figure 3.9 SBS resonator design and characterization: (a) Splits of resonator for fabrication robust phase matching (b) 780 nm SBS resonator with Q_i = 145 M, Q_l = 65 M, loss 0.36 dB/m (c) Measured FSR for R3 780 nm SBS resonator at 5.52 GHz (d) 698 nm SBS

resonator with Q_i = 73 M, Q_l = 37.3 M, loss 0.76 dB/m (e) 674 nm SBS resonator with Q_i = 40 M, Q_l = 16 M, loss 1.6 dB/m.

3.4.2 SBS laser characterization

The resonator is coupled to cleaved fibers with a ~ 3.5 dB/facet fiber-chip coupling loss. A commercial pump laser was used for pumping, and at 674 nm and 780 nm, a tapered amplifier was used to boost the pump power. The pump was PDH locked to the resonator quadrature point, and the on-chip pump power was varied to obtain the threshold, Stokes power, FLW, and frequency noise (FN). Figure 3.10 shows the common setup schematics used for the measurements. All three wavelengths showed significant FLW reduction and ~ 20x integral linewidth reduction. Moreover, different pump designs were used to observe the SBS, demonstrating the robustness of SBS operation.

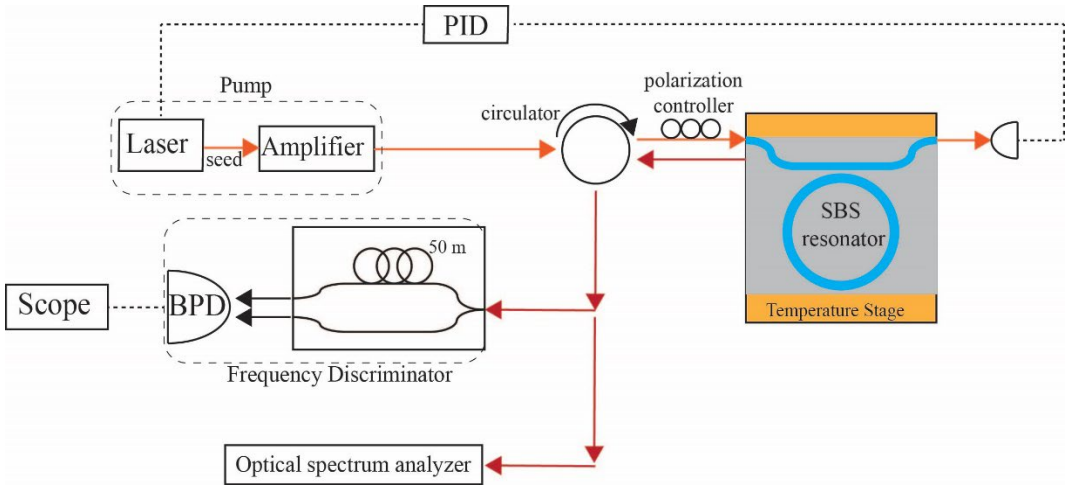

Figure 3.10 SBS characterization schematic: An optical spectrum analyzer is used to measure the Stokes power and threshold, and an OFD is used to measure the FN, similar to the TE SBS.

674 nm: A commercial Littrow cavity laser was amplified using a tapered amplifier (both MogLabs™), providing up to 120 mW pump power to the resonator. The 674 nm SBS shows the highest threshold at ~ 10 mW owing to high losses of 1.8 dB/m which are ~ thrice the

expected losses. This high loss might be due to more particles in the UCSB fabrication run or the core thickness being slightly thinner, resulting in a higher critical bend loss and, hence, a bend loss contribution. The slope efficiency of the SBS laser was ~ 14% with an on-chip power S1 power below the S2 threshold of 4.2 mW, and the facet loss was 4 dB/facet. The fundamental linewidth shows a reduction of 3700 times, whereas the 1/π reverse integral linewidth (1/π ILW) shows a ~ 20x reduction.

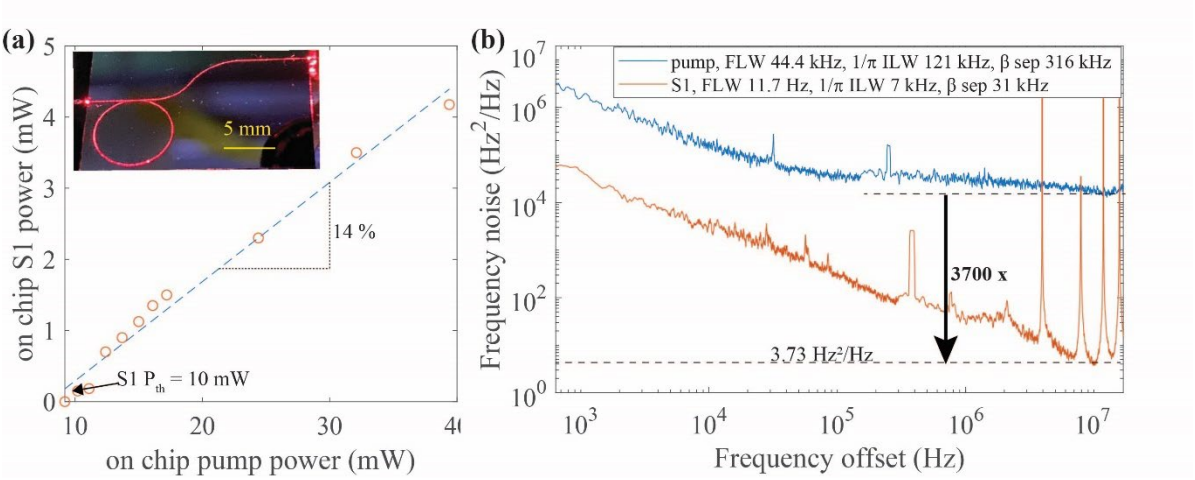

Figure 3.11 674 nm TM0 SBS measurements: (a) S1 power vs. on-chip power showing a 10 mW threshold, inset shows the SBS ring at low pump power. (b) OFD FN traces of the pump and S1 with the S1 pump power ~ 40 mW, right below S2. S1 demonstrates over three orders of magnitude of FLW reduction, which is close to the Schawlow Townes limit of these resonators at ~ 6 Hz. The integral linewidth was also reduced by more than an order of magnitude.

698 nm: A commercial cateye external cavity laser was used as the pump (MogLabs^{TM} CTL), providing up to 14 mW of pump power to the resonator, as there was no TA, SOA, or injection lock (IL) diode available for boosting power. The 698 nm SBS shows threshold at ~ 6.7 mW which is higher than calculated 3 mW, possibly due to higher than expected losses and imperfect phase matching Brillouin gain peak. The slope efficiency of the SBS laser is ~ 30 % with a maximum on-chip power S1 power 2 mW with a 14 mW pump, as shown in

Figure 3.11 (a), with facet loss at 2 dB/facet. The SBS is verified on the OSA with the SBS peak at ~ 24.5 ± 1 GHz, with resolution limited by the OSA (Figure 3.12 (b)). The pump-back reflection was suppressed by over 15 dB from S1. Another method adopted to observe SBS lasing is to ramp the laser over the resonance at 12.5 a of pump power. As the laser entered the hot resonance, an asymmetric resonance was observed. Observing the back reflected power simultaneously on the scope, a sharp change is observed in the back reflected signal, as shown in Figure 3.12 (d), as the Stokes power is higher than that of the back reflected pump.

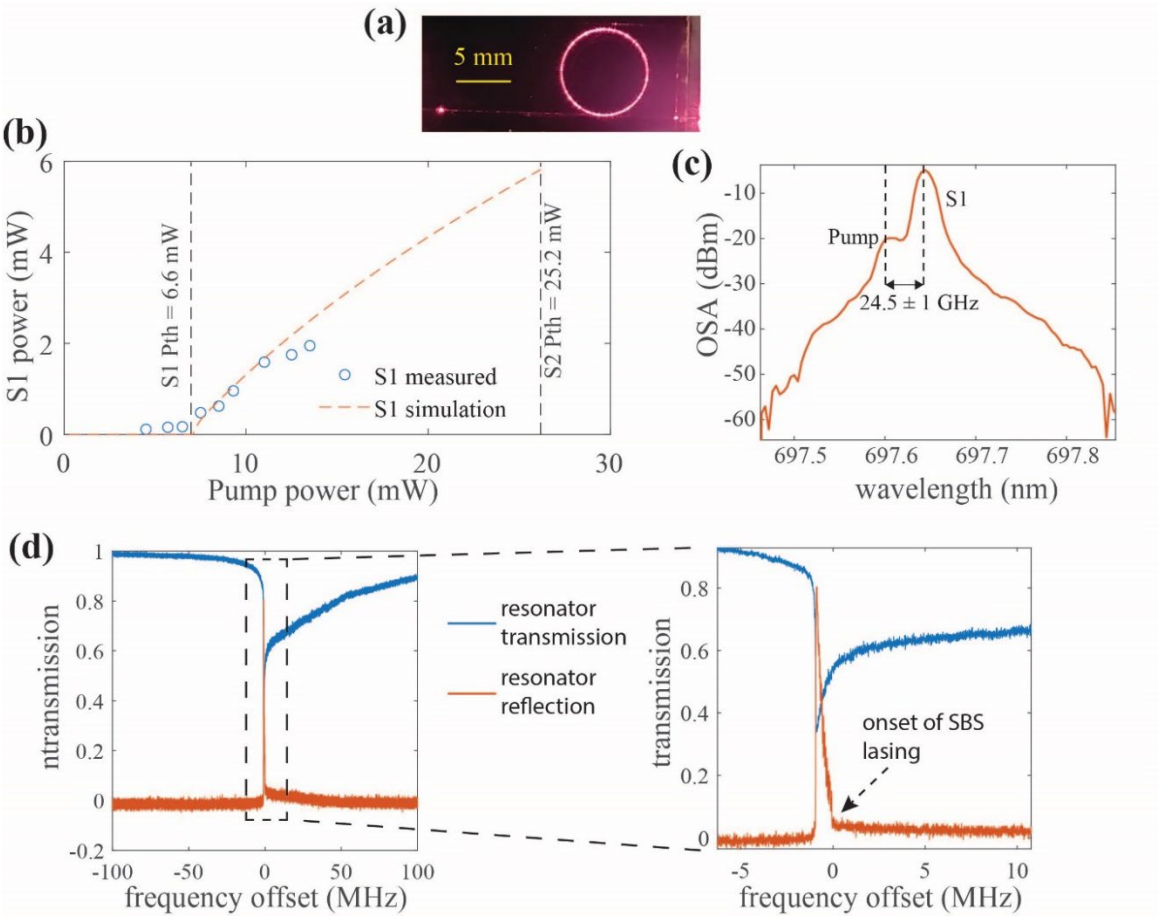

Figure 3.12 698 nm TM0 SBS threshold and stokes power: (a) The resonator used for SBS lasing. (b) Stokes power vs the pump power with threshold of 6.6 mW and maximum on chip pump power of 14 mW yielding a S1 of ~ 2 mW. (c) OSA trace of the stokes and back reflected pump showing the brillouin shift. (d) Laser ramp over the resonance also demonstrating the thresholding behavior as there is jump in backpropagating power with the onset of S1 lasing in

the resonator. If the pump power is increased above the S2 threshold, another slope change would have been observed as the onset of S2 clamps the S1 power.

The noise dynamics of the SBS laser were characterized by performing OFD and were compared to the simulated noise dynamics. The OFD is measured with increasing pump power, as shown in Figure 3.13 (a), and exhibits the expected increase in suppression with increasing pump power [1,7,74,139]. The measured fundamental linewidth from the FN measurements matches well with the simulated fundamental linewidth as a function of pump power, as shown in Figure 3.13 (b). The FLW suppression in the Brillouin laser is 570 x with a minimum FLW achieved at 7.8 Hz at 14 mW of pump power, at higher pump power, the FLW is expected to keep going down to a Schawlow Townes linewidth of 4 Hz, ~ 1000 x reduction from the pump. The SBS laser also exhibits over 10x reduction in the ILW.

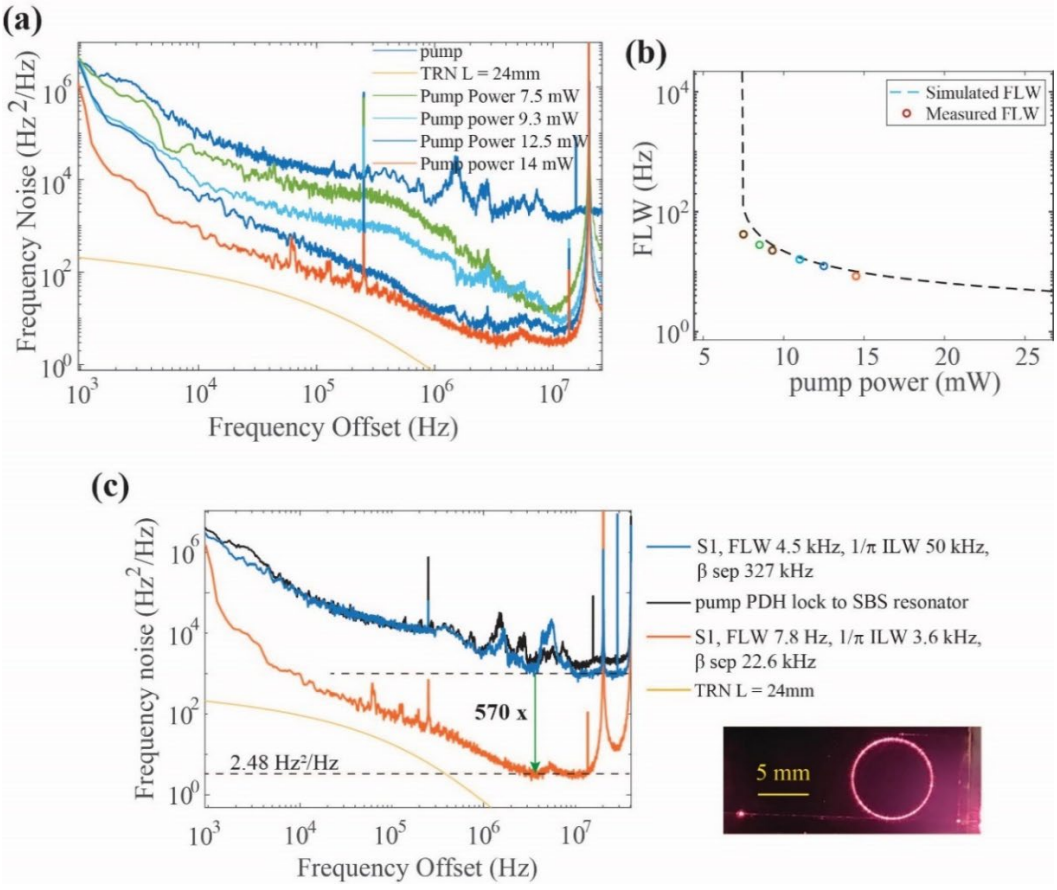

Figure 3.13 Frequency noise dynamics of 698 nm TM0 SBS laser: (a) OFD FN at different on chip pump powers showing expected behavior of decreasing FN (and greater noise suppression from

pump) as the on chip pump power is increased. (b) Measured and simulated FLW as a function of pump power showing excellent agreement. (c) The best FN plotted with the free running pump and the pump locked to SBS ring resonator when pumping SBS, on right shows the resonator at low pump power.

780 nm: This study demonstrates the first cascaded emission in a near-visible integrated SBS resonator. A commercial 780 nm DBR semiconductor laser (Photodigm^{TM} mercury package laser) with a tapered amplifier was used to pump the laser to the threshold and into cascaded mode operation, as shown in Figure 3.14 (a). First, resonator R1 was tested (5.84 mm radius). The pump is PDH locked to the resonator quadrature point and on-chip pump power varies from 0.4 mW to 34 mW. The Stokes power vs. input pump power for the first three Stokes orders is plotted in Figure 3.14 (a), with the S1 threshold measured at 3 mW, the S2 threshold at 12 mW, and the S3 threshold at 22 mW, and each order clamps at the onset of the next higher-order threshold. The spectrum of light reflected from the resonator is observed on an optical spectrum analyzer (OSA) at different pump power values (Figure 3.14 (b)) with the counter-propagating odd number Stokes tones S1 and S3 as prominent peaks and the reflection from the far side of the chip of forward propagating S2 as a small peak. The Brillouin gain shift was measured at ~22 ± 1 GHz, limited by the OSA resolution, which matches well, within 1%, from the calculated Brillouin gain offset. Another frequency doubled pump laser amplified with an SOA is used to test the threshold of R1 ring over 6 nm of bandwidth and shows only marginal increase in threshold and operates with < 1.6 mW threshold for S1 over entire S1 with a minimum threshold of 0.8 mW obtained at 776.9 nm, Figure 3.14 (e). The lower threshold at approximately 777 nm indicates better phase matching for resonator R1 at the shorter wavelength of 777 nm. We also measure the threshold of the

smaller ring R3 (R = 4.4 mm) and find its threshold to be 0.8 mW at 780 nm, demonstrating the first sub mW integrated SBS laser near visible, Figure 3.14 (c) and (d).

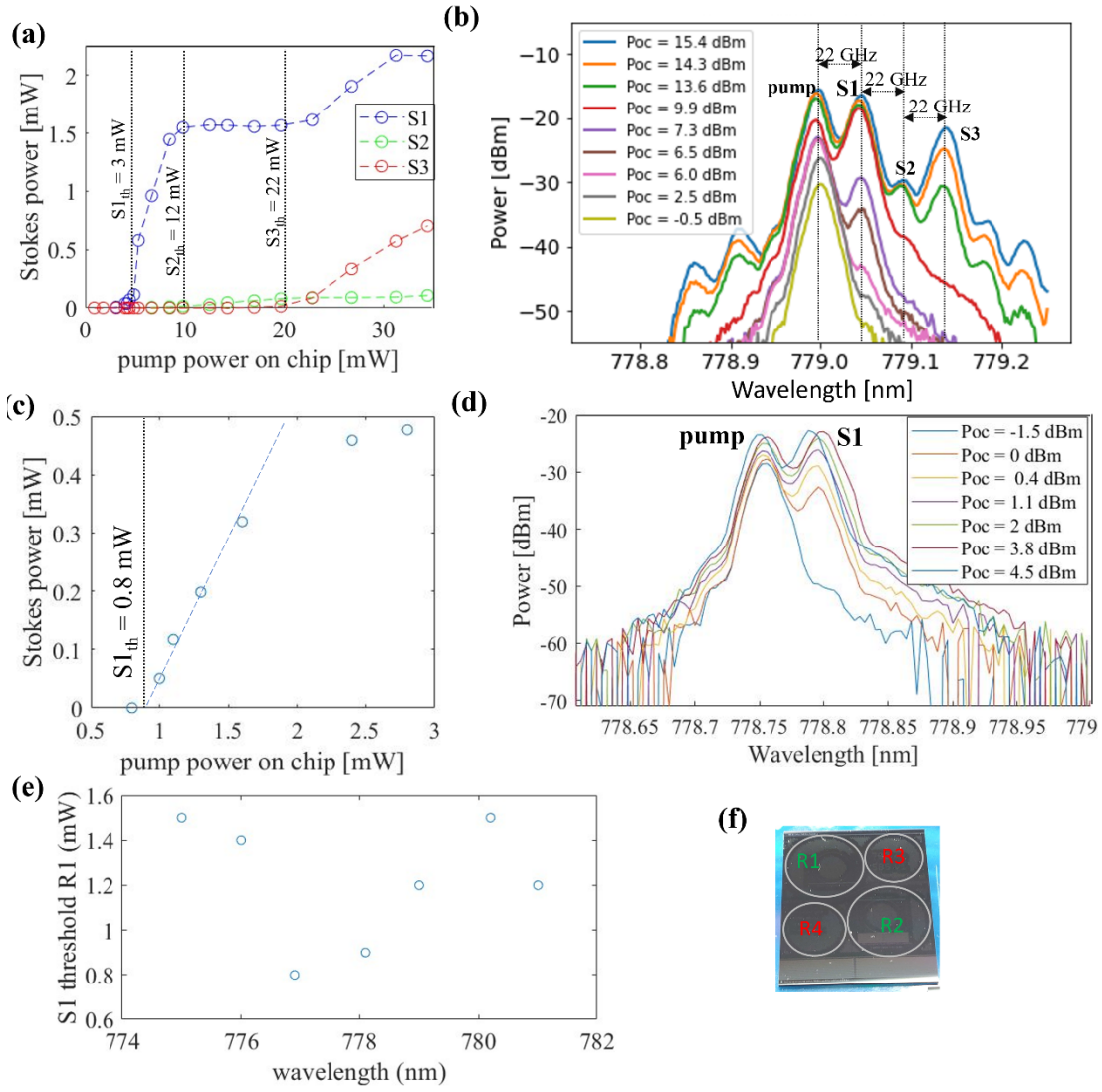

Figure 3.14 780 nm SBS measurements: (a) R1 ring Stokes power as the pump power is increased for cascaded emission at 780 nm. (b) OSA traces corresponding to powers in a for R1. (c) R3 ring Stokes power and pump power at 780 nm. (d) OSA traces corresponding to powers in c for R3. (e) Wavelength sweep demonstrating wide bandwidth operation of a single SBS ring resonator with < 3 dB change in threshold, with the 4 rings, a much wider tunable bandwidth can be achieved on the same mask. (f) Fabricated device with 4 SBS resonators.

The Frequency noise of S1 was measured immediately below the S2 threshold pump power. In the case of 780 nm, unlike the 674 nm and 698 nm resonators, a tight PDH lock is performed for the pump to the SBS resonator exhibiting ILW reduction. The SBS further reduced the ILW and provided a narrow FLW of 19 Hz. The Schawlow Townes linewidth of this resonator is at ~ 0.6 Hz but that cannot be achieved with the current pump as the measured suppression factor of over 2500 for TM SBS is close to theoretical suppression factor of $(1+300/6)^2$ ~ 2600 possible for these resonators, Figure 3.15.

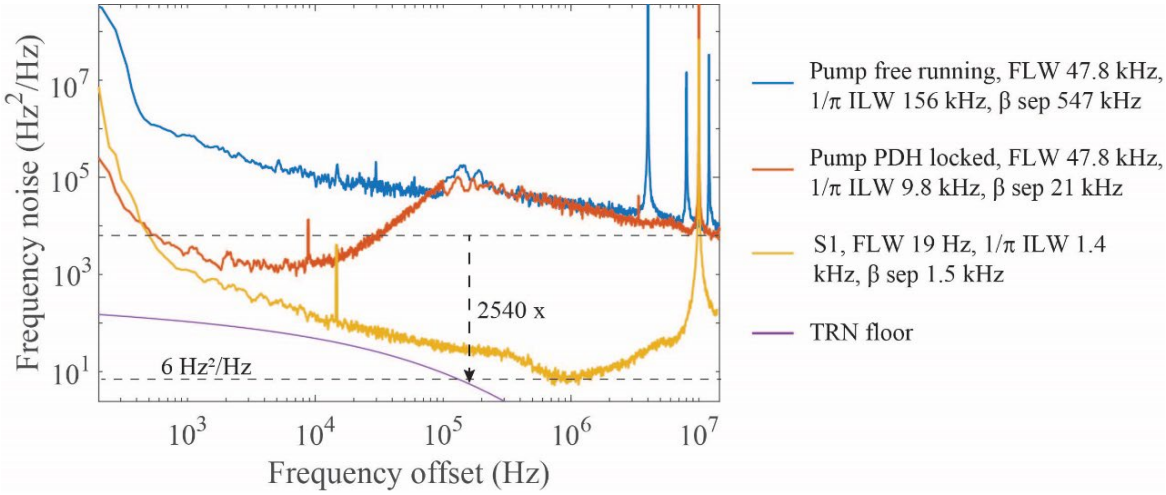

Figure 3.15 Frequency Noise of 780 nm TM0 SBS: Comparison of the FN of the 780 nm free running pump, pump PDH locked to the SBS ring for pumping SBS and S1 pumped by the tightly locked pump to the SBS ring.

3.5 Conclusion

This chapter demonstrates visible light SBS lasers and the measurement of Brillouin gain in a waveguide photonic integrated circuit. The 674 nm laser is designed to serve as a low phase noise "direct-drive" chip-scale source that can couple directly to the $^{88}Sr^{+}$ ion clock and qubit transition, 698 nm for the ^{87}Sr clock transition and 778 nm for ^{87}Rb two photon clock transition without the need for intermediate frequency doubling and has wide application to other visible light ultra-low phase noise applications including quantum and precision metrology. The bus-coupled ring laser design produces Brillouin linewidth narrowing in the visible region by operating in the regime of a long photon lifetime, short phonon lifetime, large cavity volume, and long resonator decay time. To meet these lasing requirements, prior limitations are overcome, and advances in visible light photonics are required, including low waveguide losses and high resonator intrinsic Qs, in large mode volume and low Schawlow Townes limit resonator-based SBS lasers [139]. Laser frequency noise sources include SBS fundamental noise [130], intrinsic noise of the SBS cavity, noise coupling from the backscattered pump, technical noise sources in the pump laser and SBS resonator, and pump amplitude-to-phase noise conversion. These noise sources can be reduced by locking the resonator, pump laser, or modulated S1 emission to an optical reference cavity [135]. Combining these advances with the results reported here shows promise for visible laser linewidth and stability for precision applications that normally require tabletop laser systems. Using this laser design, SBS lasing can be achieved at other visible wavelengths by making mask-only changes to the pump source. To illustrate this versatility, we demonstrate lasing at 698 nm, a wavelength suitable for probing long-lived transitions in ^{87}Sr, and 778 nm for ^{87}Rb.

To improve the SBS laser efficiency and further reduce the linewidth, simulations showed that improvements can be made with closer FSR matching to the Brillouin gain peak shift. Calculations predict a factor of 2x reduction threshold for the 674 nm and 698 nm TM0 SBS thresholds, as well as higher S1 optical output power. FSR optimization can be achieved by adjusting the SBS cavity using waveguide tuning utilizing the thermal [141] and piezoelectric [142] techniques. With the continued increase in the S1 photon number up to the S2 threshold and with pump filtering, the fundamental linewidth can be reduced to ~ 2 – 4 Hz, which is the Schawlow-Townes limit of these resonators. Further improvements will require lowering the visible light loss by exploring additional silica deposition processing techniques [24], larger-volume SBS resonators, and different waveguide modes for lasing. Other possible improvements to further reduce the linewidth include modulating the laser resonator with grating or photonic molecules, splitting the second-order Stokes (S2) resonance, preventing S2 emission, and further increasing the S1 optical power [139]. Given the transparency and bandgap of the silicon nitride core and the low loss achievable down to ~405 nm, this platform can support a wide range of SBS photon-phonon interactions and, as such, wavelengths for a variety of atomic and molecular transitions. Future work can demonstrate this design across a broad range of silicon nitride waveguide transparencies (e.g., Yb @ 578 nm, Ca + @ 729 nm) and waveguides with a higher bandgap that can support the UV (e.g., Al+ 267.4 nm).

Chapter 4: Coil resonator stabilization cavities

4.1 Introduction

Stabilized lasers are critical for applications that demand low laser phase noise and high carrier stability, including atomic clocks [15], microwave photonics [143,144], quantum applications [145–147], as discussed in Chapter 1 and energy-efficient coherent communications systems [148]. Lasers with integral linewidths below 1 Hz and Allan deviations greater than 10^{-16} over ∼1 s have been realized using Pound–Drever Hall (PDH) locking to ultra-stable optical cavities [4,61,105,149]. This level of performance is achieved with tabletop, vacuum-cavity, cryogenic, ultrahigh finesse resonators that employ sophisticated mirror and athermal designs, and other features to mitigate intrinsic thermal fluctuations [62,150]. Translating the qualities of these systems to a photonic integrated, CMOS compatible, wafer-scale platform will enable new generations of precision portable applications, as well as systems-on-chip integration [107].

Progress towards miniaturization of PDH-locked stabilized lasers has centered mainly on bulk-optic reference cavities and a limited number of integrated cavities. Centimeter-scale whispering gallery mode (WGM) resonators have yielded a fractional frequency noise (FFN) stability of 6×10^{-14} at 100 ms in a thermally and acoustically isolated vacuum enclosure [151]. Injection locking a diode laser to a crystalline WGM resonator achieves a sub-100 Hz integral linewidth and an FFN stability of 4.2×10^{-13} at 10 ms [152], which requires a glass coupling prism for fiber-to-resonator power coupling and a hermetic package to reduce environmental thermal noise. A fused silica microcavity stabilized a semiconductor

laser to a 25 Hz integral linewidth and an FFN stability of 1×10^{-13} at 20 ms [9,153]. In general, it is desirable to increase the optical mode volume to reduce various intrinsic thermal noises that scale inversely with the mode volume [3,151,154–156]. The stabilization of a fiber laser to a deep-etched silica waveguide spiral resonator yielded a linewidth of 4×10^{-13} at 0.4 ms and of the order of 100 Hz linewidth [3]. However, novel approaches that are less environmentally sensitive and wafer-scale CMOS compatible are critical. Recent CMOS compatible, silicon nitride resonators achieved a $1/\pi$ -linewidth reduction from 3.66 kHz to 292 Hz and a carrier stability of 6.5×10^{-13} at 8 ms [155]. Microfabricated compact cavities have been demonstrated more recently as scalable high-finesse cavities; however, these require bulk optics processing steps for thin film coatings for reflection and are not compatible with CMOS fabrication [157,158].

This chapter reports photonic integrated laser stabilization achieved by locking semiconductor lasers in O-bands and in visible to photonic integrated coil resonators. The visible and 1319 nm coil resonators employ 3.0 m and 4.0 m long coils, significantly lowering the cavity-intrinsic thermorefractive noise (TRN) over other designs [156] as well as susceptibility to photothermal noise induced fluctuations. The visible coil resonator has two designs: a lower Q TE0 mode resonator at 674 nm with measured $Q_l = 20 \times 10^6$, $Q_i = 40 \times 10^6$ and FSR = 67.4 MHz and the TM0 mode high Q resonator with measured $Q_l = 58.5 \times 10^6$, $Q_i = 93.2 \times 10^6$ and FSR = 65.5 MHz. The TM0 mode coil also performs well at longer red wavelengths with measured $Q_l = 43.4 \times 10^6$, $Q_i = 100 \times 10^6$ and FSR = 66.9 MHz at 698 nm, and has a mode volume of $\sim 5 \times 10^6$ μm^3. The 1319 nm coil resonator measures a FSR = 48.9 MHz, $Q_i = 142 \times 10^6$, $Q_l = 71 \times 10^6$, and $\sim 1 \times 10^8$ μm^3 mode volume. The large mode volume, 3 m length resonator is used to PDH lock a commercial 674 nm laser demonstrating

a 4.2 kHz 1/π integral linewidth, an 8.8 kHz β-separation linewidth, and an Allan deviation (ADEV) of 3.5 x 10^{-12} at 20 ms and a 4 orders magnitude noise suppression at low frequencies. The coil resonator has an intrinsic Q of 40 × 10^6 and a 70 MHz FSR. The locked noise performance, which is currently limited by resonator Q and gain saturation, can be reduced toward its TRN-limited linewidth in the visible coil of 12 Hz using further waveguide loss reduction techniques [13, 9] or using an SBS laser as the pre-stabilization cavity. These long, ultra-low loss waveguides can also be used for other applications such as delay lines, extended cavities of external cavity lasers, and Mach–Zehnder modulators. The performance of the O-band is limited owing to drift and reaches the TRN floor at 1–50 kHz frequency offsets. Parts of this chapter were adapted with permission from our previous publications [59,159].

4.2 CoilR design

The low-loss dilute-mode waveguides described in Chapter 2 have inherent advantages for low TRN operation as the mode areas are quite large compared to tightly confining and moderately confining waveguides; for example, the mode area of a 674-698 nm waveguide is 3 μm^2, while for O-band devices it is 30 μm^2, while moderately confining 674 nm has ~0.3 μm^2 area. Moreover, to design a long length, and hence a short FSR resonator, to further reduce the mode volume and hence the TRN floor, low losses are required such that the FWHM is approximately less than half of the FSR of the resonator to prevent the resonances from overlapping. Thus, the Si_3N_4 platform is suitable to enable such a coil resonator cavity design for stabilization [59,159]. Figure 4.1 compares the TRN floor of this work's visible waveguides with tightly confining core waveguides [8] as well as the miniature

rod bulk cavity [9], showing around 7 order of magnitude reduction in TRN when comparing coil resonator (ii) with small tightly confining resonators (iv).

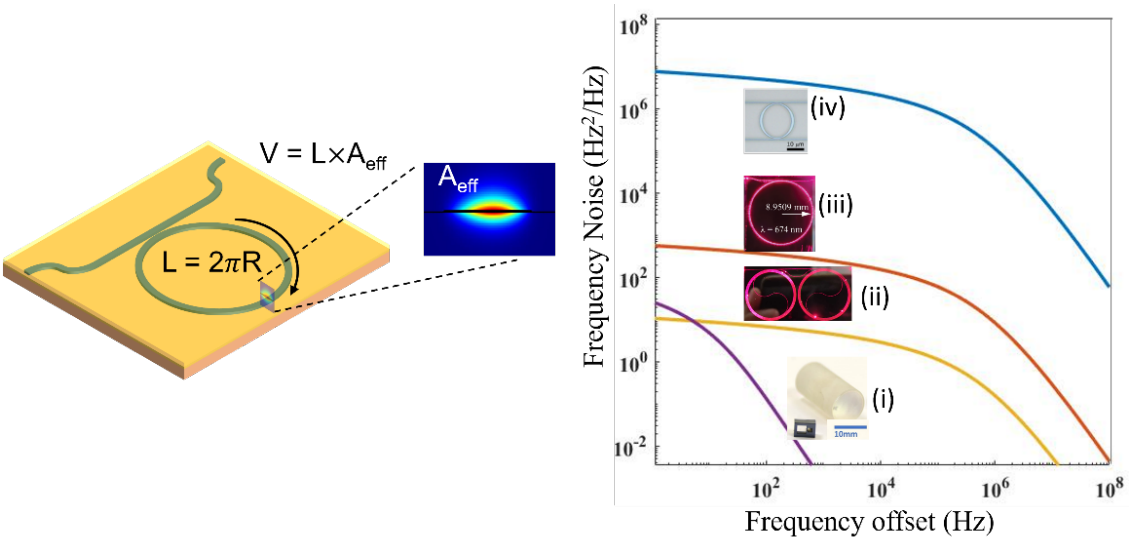

Figure 4.1 CoilR design considerations: The large area dilute mode waveguide resonator with 9 mm radii shown in (iii) [7] has nearly four orders of magnitude lower TRN floor than tightly confined in (iv) [8] which is crucial for both laser design and for stabilization cavity design for low noise performance. This limit can be further lowered by making long length of cavity to increase the mode volume further reduce the TRN floor shown in (ii) (this chapter) and approaches the performance of bulk miniature high finesse Fabry-Perot cavities like silica microrods in (i) [9].

674 nm and 698 nm coilR: The 3 m Si_3N_4 coil resonator consists of high-aspect-ratio waveguides (Chapter 2) with a waveguide core at a coupler with a width of 2.3 μm and core thickness of 20 nm, supporting a single fundamental TE0 mode. The waveguide spacing in the coil is 40 μm and the inner S bend is 4.5 mm in radius and the waveguide width is increased to 3.5 um for the coil part to avoid bend losses. The Q and FSR were measured using an unbalanced MZI of $Q_l = 20 \times 10^6$, Q_i of 40×10^6, and FSR = 67.4 MHz, as shown in Figure 4.2, and fabricated in the UCSB cleanroom. The TM0 mode coil resonator also had a length of 3 m, used for 698 nm, the width of the coupling region was kept at 2.3 um while the coils

at 3 µm and the loss are discussed in section 2.3.2 and Figure 2.6. The coupling region for both is a directional coupler, as relatively high values of the power coupling coefficient are required to achieve critical coupling, 36-48 % and is analogous to a pulley coupler in ring resonators.

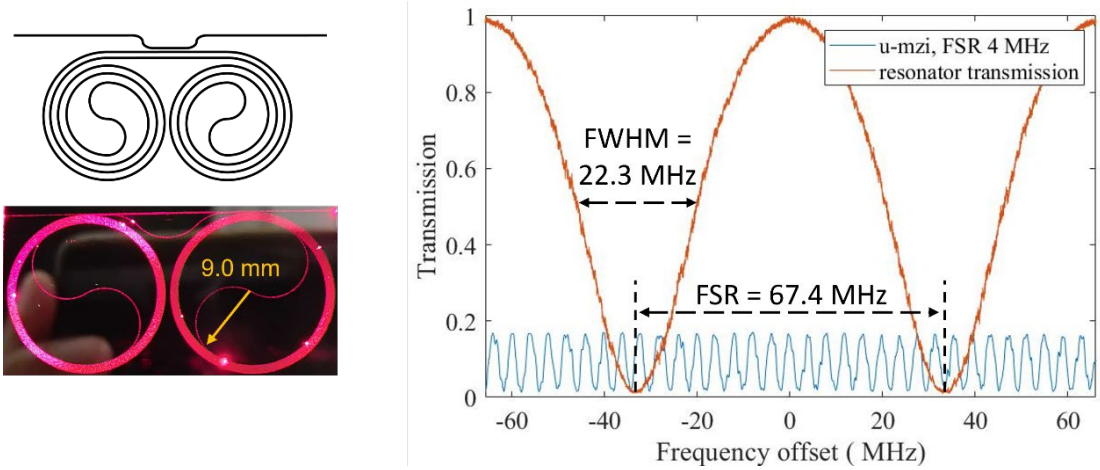

Figure 4.2 TE0 mode coilR at 674 nm: The coil design picture of coil coupled with 674 nm laser is shown on left with the measured Q and FSR Q_l = 20 x 10^6, Q_i of 40 x 10^6 and FSR = 67.4 MHz shown on the right.

1319 nm coilR: The Si3N4 4.0 m coil waveguide resonator employs a high aspect ratio waveguide core design, like the visible coils, 6 µm wide × 80 nm thick, with a 15 µm thick thermal silicon dioxide lower cladding and 6 µm thick oxide upper cladding. The coil waveguide spacing was 40 µm and the minimum bending radius was 4.5 mm. This waveguide design was chosen to provide a low-loss high-aspect-ratio waveguide for the fundamental transverse magnetic (TM0) mode to mitigate sidewall scattering loss and to minimize the coil bend radius, waveguide bend loss, and crosstalk between coil waveguides [23]. The directional coupler for 1319 nm has a 3.5 µm gap and 0.5 mm coupling length to provide ~ power coupling coefficient of ~ 18 %. Such a coupler design provides proper coupling for the fundamental TM mode and weak coupling for transverse electric modes. To measure the

resonator Qs, we used a fiber-extended-cavity semiconductor laser developed by Morton Photonics™ [143] to probe the resonator and perform spectral scans with a radio frequency (RF) calibrated fiber Mach–Zehnder interferometer (MZI) as an optical frequency ruler. The 1319 nm resonator is measured to have Q_i = 142 million and Q_l = 71 million, corresponding to a propagation loss of 0.16 dB/m.

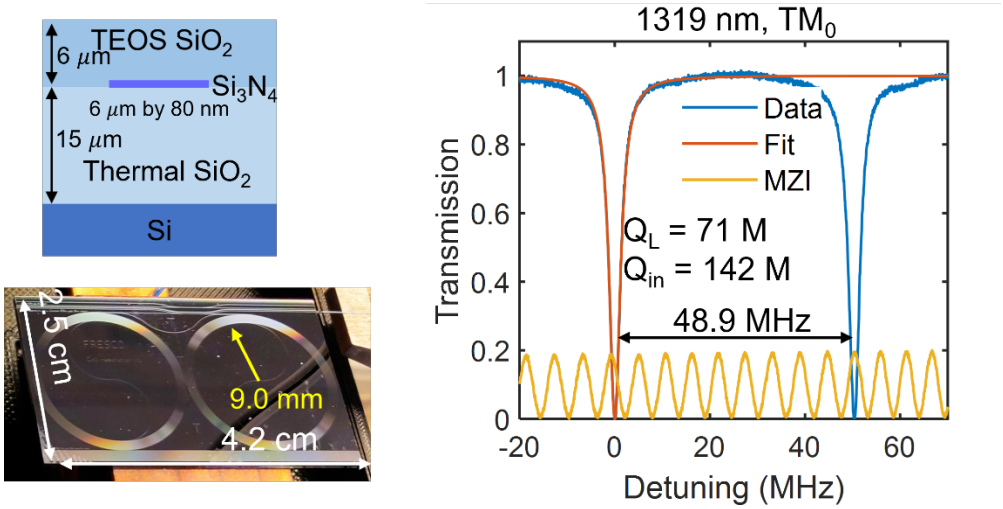

Figure 4.3 TM0 coilR at 1319: Coil cross section and device image on the left with the Q measurements on right with Q_i = 142 million and Q_l = 71 million corresponding to a propagation loss of 0.16 dB/m and FSR = 48.8 MHz.

4.3 Laser Stabilization using coilR

Laser stabilization was demonstrated by PDH locking commercial lasers to coil resonators and by measuring the frequency noise. The PDH lock requires low power and 3-6 dBm of power is tapped from the laser for the lock. The coil resonator was mounted on an active temperature-controlled stage with an mK-resolution temperature controller (Vescent™ QTC) inside a passive enclosure [59,155]. The PDH lock requires ~0.2 mW optical power at the photodetector for 1319 nm, 60 μW for 674 nm, and 100 μW for 698 nm to provide a

sufficient signal-to-noise ratio (SNR) to overcome other noise sources such as photodetectors and shot noise. The PDH locking bandwidth was approximately 1 MHz using a commercial servo controller (Vescent^{TM} D2-125). To measure the frequency noise and laser-carrier stability, we used two independent methods. A fiber-unbalanced MZI is used as an optical frequency discriminator (OFD) for self-delayed homodyne laser frequency noise measurement at a frequency offset above 1 kHz [59,160], and is utilized for all 3 wavelength coil resonators that are described here. Because the fiber noise in the MZI dominates at frequencies below 1 kHz offset, we employ a Rock single-frequency fiber laser PDH locked to a Stable Laser Systems (SLS) ultralow expansion (ULE) cavity, delivering a Hz-level linewidth output at 1550 nm wavelength with a frequency drift of ~0.1 Hz/s, which is then transferred to other wavelengths using a commercial fiber frequency comb and second harmonic generation. Furthermore, a GPS reference is also available for long-term stability, but is not used for coilR measurements. This laser is referred to as a stable reference laser (SRL). The SRL frequency noise measurement below 1 kHz was performed by photo-mixing the SRL with our stabilized laser on a high-speed photodetector to produce a heterodyne beat note signal that was measured using a precision frequency counter (Keysight^{TM} 53200A). The 674 nm coilR was characterized with both OFD and beatnote, and the beatnote for 698 nm and 1319 nm will be performed in the future. In addition, a 674 nm beatnote measurement was also performed on an ESA and 3 dB bandwidth ILW was also reported to demonstrate good agreement between different measurement techniques. Figure 4.4 shows the full measurement setup.

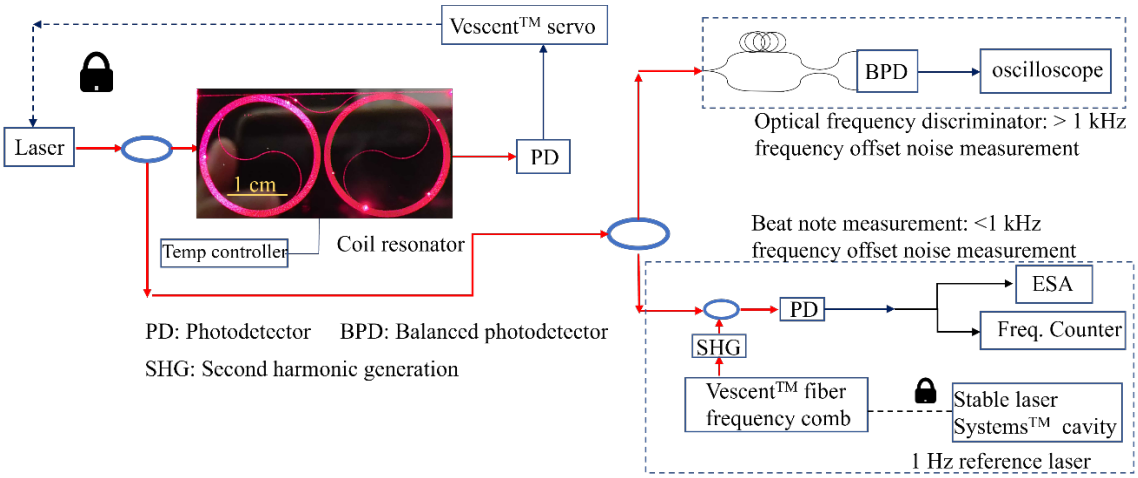

Figure 4.4 Setup schematic for complete frequency noise measurement: Frequency noise measurement is carried out with a combination of optical frequency discriminator (OFD) for frequency offsets > 1 kHz and a beatnote measurement by beating with a stabilized laser on frequency counter for offsets < 1 kHz and stitched together.

698 nm Coil lock: A Moglabs™ cateye external cavity laser was locked to the coil resonator. The measured FN is plotted below and shows a 2-4 orders of magnitude reduction in FN in the lock bandwidth. The integral linewidth is < 1 kHz, which is limited by the OFD noise. The beatnote measurement was not fully set up and will be performed in the future to extract an accurate integral linewidth. The FN does not reach the TRN floor, possibly because of the high FN of the pump laser used and the limited servo gain and bandwidth of the lock.

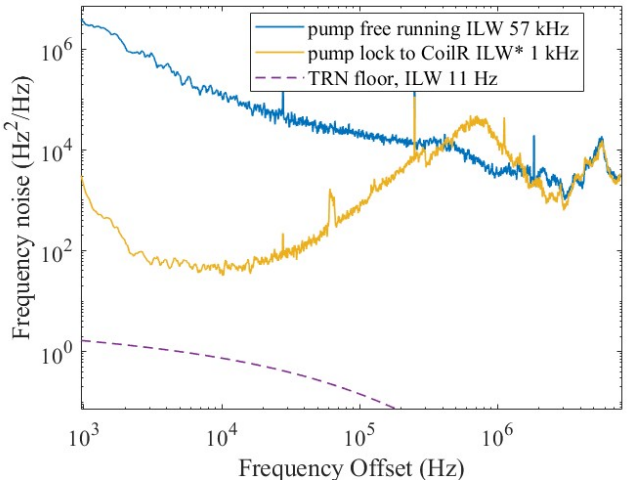

Figure 4.5 698 nm CoilR: FN measurement of 698 nm source locked to the TM0 mode coil resonator; the locked laser does not reach the TRN floor but still shows over 50x ILW reduction as well as 2-4 order of magnitude of noise reduction.

1319 nm Coil lock: A Morton Photonics semiconductor low noise laser was locked to the coil resonator. The measured FN is plotted below and shows four orders of magnitude of reduction in FN in the lock bandwidth, with the FN of the locked pump hugging the TRN floor of the coil resonator. This indicates that a longer coil can be used with an even lower TRN floor for further noise reduction at this wavelength by using the pump laser. The TRN-limited noise of this coil is ~ 1 Hz, which is difficult to achieve because of the thermal drift of the coil resonators and is not captured by the OFD, but is shown for a similar coil at 1550 nm in [59].

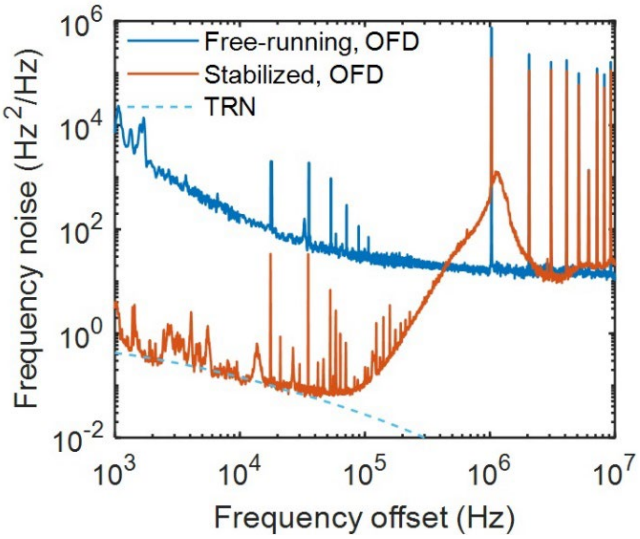

Figure 4.6 1319 nm CoilR: FN measurement of 1319 nm source locked to the TM0 mode coil resonator; the locked laser reaches the TRN floor and achieves four orders of magnitude of FN reduction.

674 nm Coil lock: A Moglabs^{TM} Littrow cavity external cavity laser was locked to the coil resonator. We stitched the low- and high-frequency noise measurements together and calculated a 1/π integral linewidth of 4.2 kHz, a Î ² integral linewidth of 8.8 kHz Figure 4.7

(c), and an Allan deviation of 3.5 x 10^{-12} at 20 ms (Figure 4.7 (d)). This is an improvement of twenty times in the integral linewidth and a second-order magnitude reduction in frequency noise. The FN does not reach the TRN floor, possibly because of the high FN of the pump laser used and the limited servo gain and bandwidth of the lock. The TRN-limited ILW of the visible coil was ~ 12 Hz.

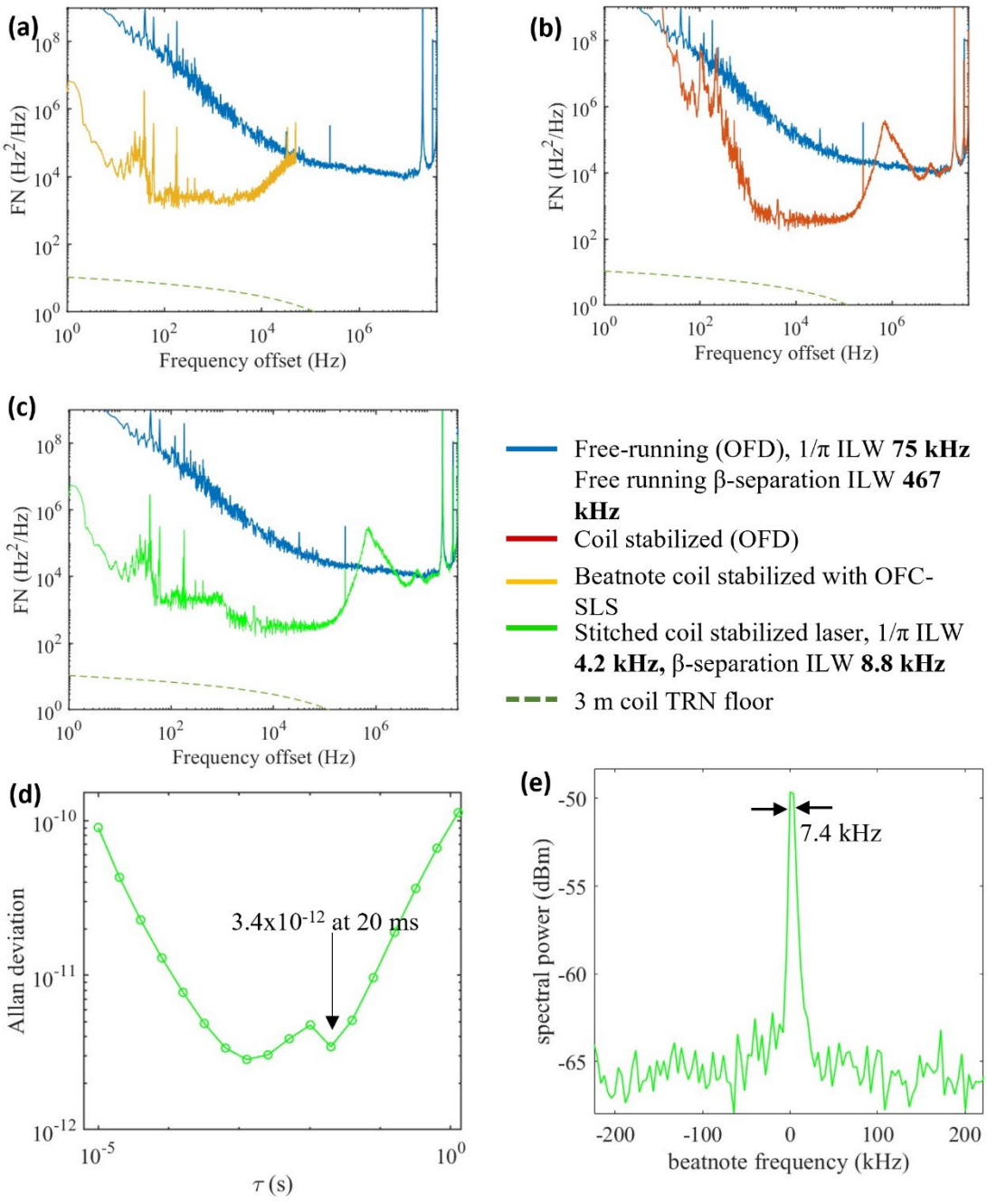

Figure 4.7 674 nm TE0 coilR measurements: (a) Beatnote measurement in yellow showing the noise getting dominated by frequency counter above 1 kHz (b) OFD measurement in red showing the coil MZI noise dominating below 1 kHz. (c) Stitched FN measurement with both, 1 kHz and > 1 kHz noise to extract the ILW, with a $1/\pi$ integral linewidth of 4.2 kHz, a β integral linewidth of 8.8 kHz. (d) Allan deviation of 3.5×10^{-12} at 20 ms. (e) Beatnote measurement on the ESA with a resolution bandwidth of 1 kHz showing the beatnote linewidth of 7.4 kHz which matches well with the calculated ILW from FN.

4.4 Conclusion

We report demonstrations of large-mode volume and low-TRN coil resonators for laser linewidth narrowing by PDH locking, with demonstration of TRN-limited FN at 1319 nm. We demonstrated for the first time a 3 meter long photonic integrated silicon nitride waveguide coil resonator operating at 674 nm and 698 nm with PDH laser stabilization, achieving a reduction of 20x in integral linewidth and two orders of magnitude improvement in ADEV and four orders of magnitude improvement in frequency noise at low offset frequencies. Further improvements in the Q of these coil resonators can enable sub 100 Hz integral linewidths and open new applications such as on-chip frequency discriminators, wavelength meters, and visible light delay lines. Table 4.1 shows a summary of the stabilization of a pump achieved by SBS or by coilR.

Table 4.1 Summary of stabilization

λ	Stabilization Process	Pump			S1/stabilized pump		
		FLW	1/π ILW	β ILW	FLW	1/π ILW	B ILW
674 nm	TE0 SBS	3.3 kHz	-	-	269 Hz	-	-
	TM0 SBS	44.4 kHz	121 kHz	316 kHz	11.7 Hz	7 kHz	31 kHz
	CoilR PDH	-	75 kHz	467 kHz	-	4.2 kHz	8.8 kHz
698 nm	TM0 SBS	4.5 kHz	50 kHz	327 kHz	7.8 Hz	3.6 kHz	22.6 kHz
	CoilR PDH	-	57 kHz	387 kHz	-	< 1 kHz	<35 kHz
780 nm	TM0 SBS	47.8 kHz	156 kHz	547 kHz	18.5 Hz	1.4 kHz	1.5 kHz

Chapter 5: CoilR stabilized 674 nm for $^{88}Sr^{+}$ qubit operations

5.1 Introduction

Trapped ions are emerging as a leading technology for quantum computing, where the ions are confined in RF traps to serve as quantum bits (qubits), and entanglement is provided by the shared ion motional modes. Trapped ions have demonstrated a single qubit with 99.9999% fidelity [161] and the highest quantum volume for commercial quantum computers [162]. The qubit is formed with the electronic states of the ion, and ion cooling, state preparation, repumping, and readout are all performed using lasers that address specific transitions. There are four types of ion qubits: Zeeman qubits, magnetically split Zeeman states, optical qubits, transitions separated by optical frequency, and hyperfine or fine structure qubits, with the first two being more commonly used qubits. As discussed in Chapter 1, the linewidth requirement of the laser is determined by the purpose; for example, the cooling and repumping lasers only require a spectroscopy lock, as they address transitions that are MHz linewidth. In contrast, lasers used for state preparation and readout must be 1 kHz or better for the Zeeman qubit (for a Rabi frequency of 50 kHz) or 1 Hz or better for an optical qubit [137].

Scaling a trapped ion quantum computer requires multiple laser beams delivered to each ion for the operation and would benefit from integrated beam delivery [49], lasers [8,163], passives [11,29], modulators [164], and stabilization cavities; the progress towards the latter has been limited to miniature bulk cavities [153,157] owing to the lack of high-Q resonators with low thermal refractive noise before this work.

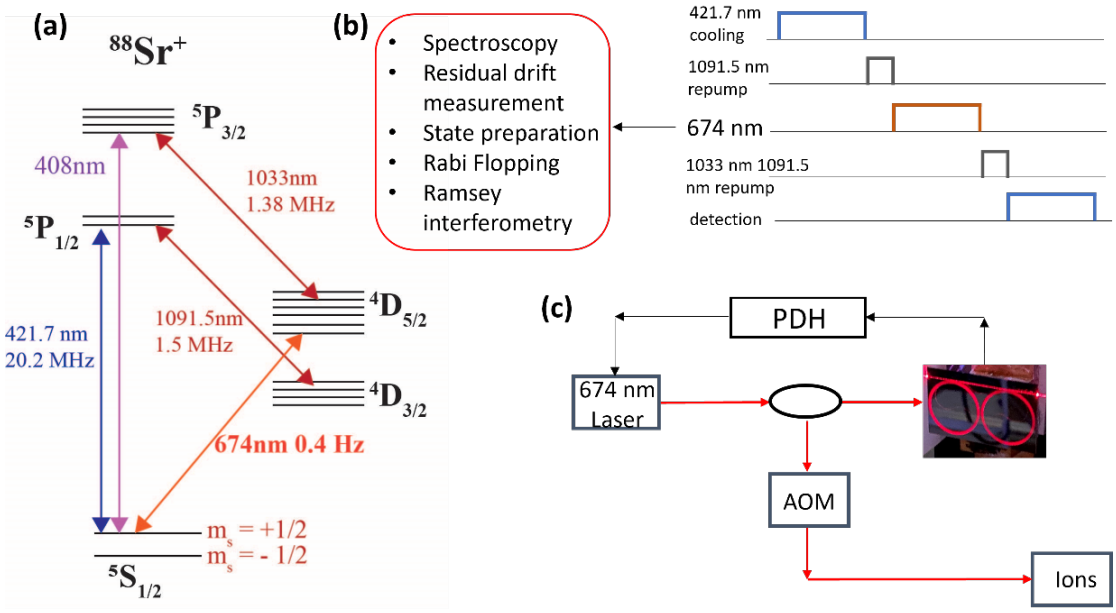

Figure 5.1 Electronic structure and 674 nm demonstrations: (a) Electronic structure of $^{88}Sr^+$. (b) A simplistic pulse sequence showing the different wavelengths involved in Sr qubit operation along with the demonstrated functionalities with coilR stabilized 674 nm. (c) Simple schematic of 674 nm laser stabilization.

In this chapter, the coil resonator stabilization cavities at 674 nm, discussed in Chapter 4, which is wavelength for $^{88}Sr^+$ optical qubit as well as state preparation and readout for Zeeman qubit, as shown in the electronic level diagram in Figure 5.1, is used to demonstrate the viability of coilR as a stabilization cavity for ion qubit applications. The CoilR is packaged in a two-layer passive metal enclosure, and the temperature of the inner enclosure is controlled with mK resolution using a commercial temperature controller to reduce thermal drift and isolate it from environmental variations. Spectroscopy sweep of the ion was performed to extract the drift and linewidth of the coilR at 2 kHz/s and 12.8 kHz, respectively. Since the second DeVincenzo's criteria for the implementation of a quantum computer requires that the system be initialized into a well-defined and determinate initial state, we demonstrate state preparation with 97% state preparation fidelity. Moreover, Rabi flopping and Ramsy

interferometry of the optical quadruple transition were demonstrated to explore the feasibility of a compact clock. The coherence of the laser severely limits these, as TRN-limited performance from the coil resonator has not yet been achieved, possibly owing to gain saturation. Further linewidth reduction and TRN-limited performance should be possible using the SBS laser demonstrated in Chapter 3 at 674 nm as an intermediate stabilization cavity, as shown in Figure 5.2.

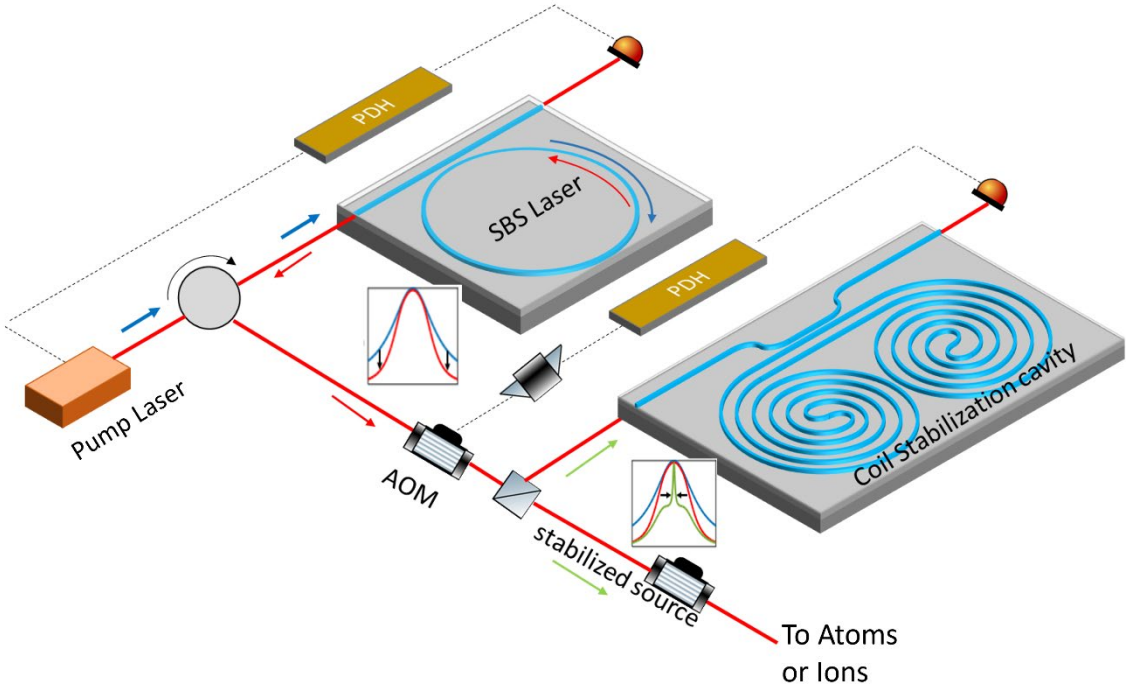

Figure 5.2 Vision schematic of SBS locked to coil: Linewidth reduction with SBS providing ~ 100-500x ILW and >1000x FLW reduction and the S1 is then locked to the coilR using an AOM for further 50x reduction in ILW.

5.2 Spectroscopy, Rabi flopping and Ramsey interferometry

5.2.1 Spectroscopy

A broad sweep of a stabilized source over the atomic transitions was performed using spectroscopy to reveal all the electronic transitions around the central wavelength. The scan also reveals the motional sidebands for the trapped ions and servo peaks. For electronic transitions that are much narrower than the laser ILW, the linewidth of the transitions in the spectroscopic scan is limited by the laser ILW. Moreover, the drift in the laser can cause an incorrect linewidth, either broadening it or even narrowing it in the case of a linear scan if the drift is in the opposite direction of the scan. To alleviate this problem, a waterfall scan is performed where the laser is not scanned linearly; instead, the scan points (laser offset) are varied randomly. This will result in the scanned linewidth being correct or wider, but never narrower than the actual linewidth. In the case of pulsed detection, the pulse duration is sufficiently long when scanning with noisier kHz ILW lasers, so that the scanned linewidth is not Fourier limited; however, when using very narrow sub-Hz linewidth lasers, the linewidth can be Fourier limited, as it is not possible to increase the scan time indefinitely. Power broadening from higher power excitation can also occur; thus, the power is kept lower than saturation in these scans as with higher power, even though the peak probability will increase the linewidth will also increase [34].

The energy level of the optical $^{88}Sr^{+}$ quadrupole transition is shown in Figure 5.3 below. For the configuration of 674 nm beam parallel to the magnetic field and at 45° from the trap RF electrodes, only four transitions are allowed: $S_{1/2,1/2} \rightarrow D_{5/2,-1/2}$, $S_{1/2,-1/2} \rightarrow D_{5/2,-3/2}$, $S_{1/2,1/2} \rightarrow D_{5/2,3/2}$, $S_{1/2,-1/2} \rightarrow D_{5/2,1/2}$. State preparation can be carried out such that all electrons

are initially in the $S_{1/2,\,-1/2}$ state, and the state preparation fidelity is measured by the contrast of the $S_{1/2,1/2}$ state. Spectroscopy can also be used to measure the magnetic field at the ion, as the Zeeman splitting of the states depends on the magnetic field strength, as follows:

$$\Delta f\ (m, m') = \left(-2.802\frac{MHz}{G}.m + 1.680\frac{MHz}{G}.m'\right).B \qquad 5.1$$

where the first term is due to splitting of the $D_{5/2}$ manifold and the second term is due to Zeeman splitting of the $S_{1/2}$ manifold. Spectroscopy can also be used to measure the drift of a stabilized laser against the absolute reference of the ion.

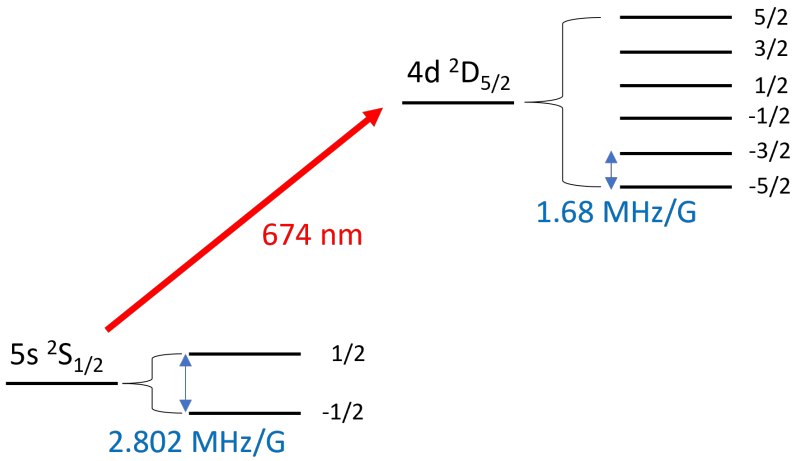

Figure 5.3 Zeeman split $S_{1/2} \rightarrow D_{5/2}$ transition: The 5s $^2S_{1/2}$ state is split into two non-degenerate Zeeman states in presence of magnetic field. These two states are used as Zeeman qubits in $^{88}Sr^+$. The 4d $^2D_{5/2}$ state splits into six Zeeman nondegenerate states.

5.2.2 Rabi Oscillations

The evolution of a two-level system in the presence of time-varying resonant electric fields, with the population exchange between the two fields, is given by Rabi flopping or Rabi oscillations, where the frequency of exchange between the two levels Ω_0 (Rabi

frequency) [165] is given by the solution of the Hamiltonian of a two-level system in the presence of a driven field as

$$P_e(t,\Delta) = \frac{\Omega^2}{\Omega^2 + \Delta^2}\left[\sin\left(\frac{\sqrt{\Omega^2 + \Delta^2}t}{2}\right)\right]^2 \quad 5.2$$

Where $P_e\ (t,\ \Delta)$ is the probability of the excited state at time T and laser detuning from resonance Δ, with Rabi frequency Ω, which is the strength of the atom laser dipole interaction. A pi pulse is defined as $\Omega T = \pi$ and results in a sinc^2 function that changes to a Lorentzian line-shape in the presence of a large decoherence of the excitation field [15]. In this regime, if the Lorentzian linewidth is larger than the Rabi frequency, it is not possible to distinguish between purely electronic (i.e., carrier excitation) and mixed electronic and motion (i.e., sideband transitions). Both laser decoherence and the motional state of the atom or ion cause decoherence in Rabi flopping.

5.2.3 Ramsey Interferometry

Ramsey interferometer, also known as separated oscillatory filed method utilizes two π/2 pulse with a varying delay time in between to allow for the phase evolution. The probability of the excited state in Ramsey spectroscopy depends only on the delay time Δt between the two π/2 pulses as

$$P_e(t,\Delta) = \cos^2\left(\frac{\Delta t}{2}\right) \quad 5.3$$

The advantage of Ramsey spectroscopy is that the two π/2 pulse durations are fixed and less dependent on the motional state than Rabi flopping.

5.3 $^{88}Sr^{+}$ operations with 674 nm coil stabilized laser

5.3.1 Drift measurements

The ion provides an absolute reference for drift measurement. The coilR was packaged in a temperature-controlled metal enclosure with a TEC controlled by a Vescent™ QTC controller with mK accuracy. This inner metal enclosure was placed in a larger metal enclosure, whose temperature was controlled using a resistive heater and the same controller. This is necessary for a very accurate temperature stabilization of the coilR. A third Styrofoam box was created to shield the coil from external acoustic vibrations. The drift of the coilR was measured as 2 kHz/s. The drift was compensated with an AOM by measuring against the ion and feedforward. Figure 5.4 shows the residual drift measured after the feedforward is reduced to a maximum of 1 kHz/min but is not linear.

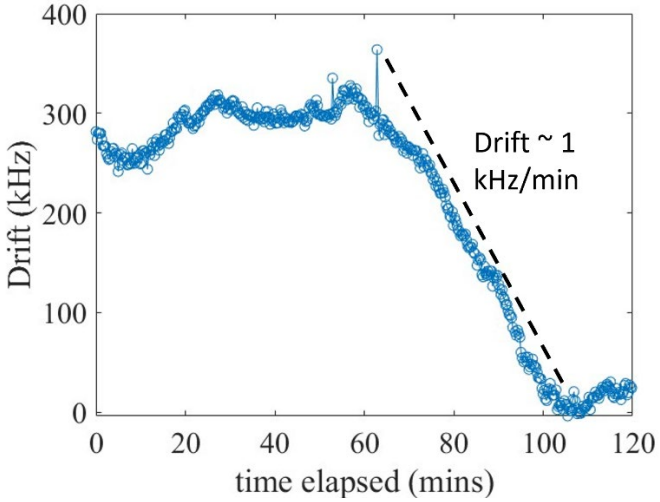

Figure 5.4 Residual drift: The feedforward reduces the drift of the coilR-locked 674 nm from 2 kHz/s to < 1 kHz/min.

5.3.2 Qubit spectroscopy

Waterfall scan of the ion is performed with the stabilized 674 nm over the $S_{1/2, -1/2} \rightarrow D_{5/2, -5/2}$ state. The interrogation times at 674 nm were kept between 10-100 μs to avoid limiting the linewidth by pulse times. A wider scan reveals the carrier and motional sidebands at 850 kHz and servo bumps at 350 kHz. The higher noise far from carrier (FLW) linewidth results in broader wings of the carrier around the servo bumps.

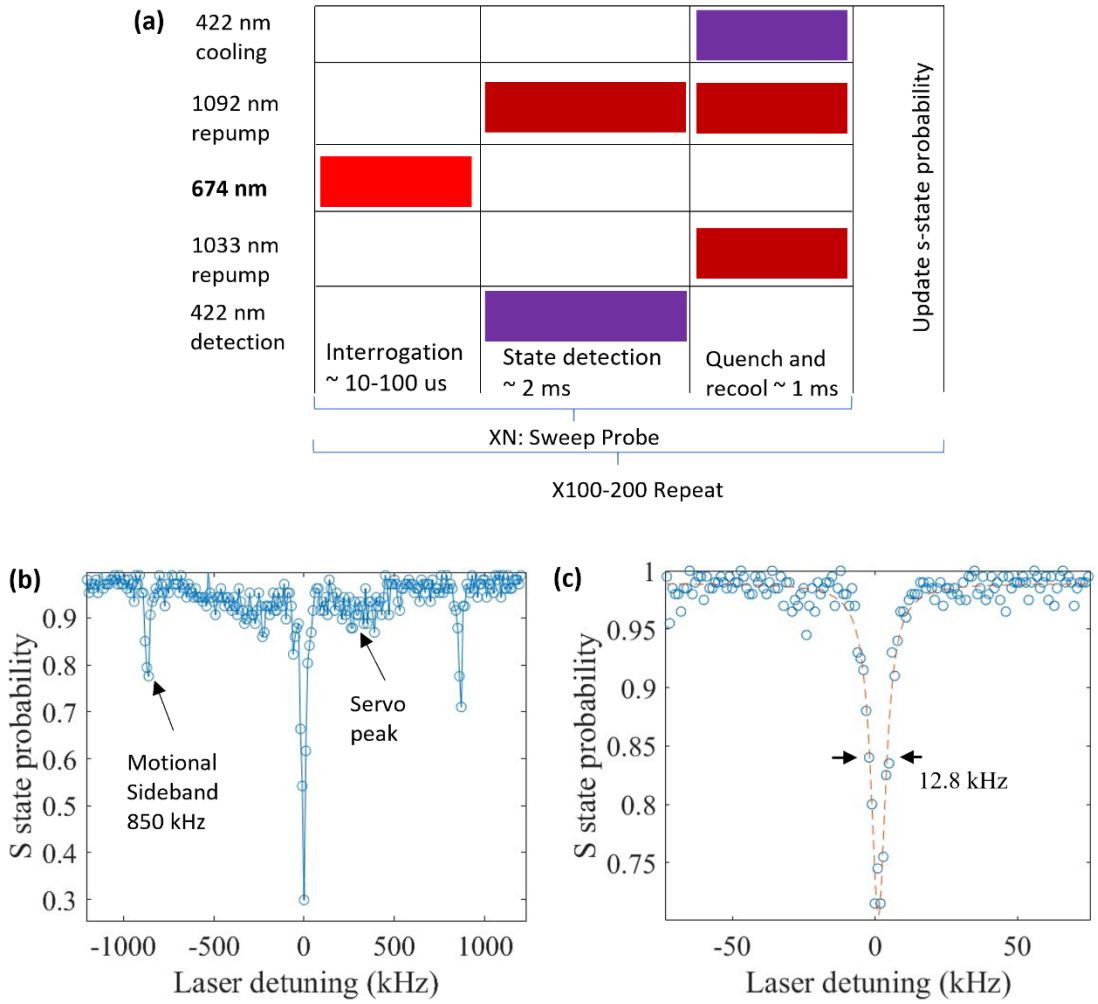

Figure 5.5: Qubit spectroscopy: (a) Pulse sequence for qubit spectroscopy. (b) A wide scan shows the LO, motional sidebands at 850 kHz and servo peaks at around 350 kHz. (c) A narrower scan gives laser linewidth limited scan indicating the laser ILW is around 12.8 kHz, the ILW could have been widened by the drift of coilR.

5.3.3 State preparation

State preparation is necessary to initialize the qubit to a particular state at the start of qubit operations. For a Zeemann qubit, the electrons are shelved into the $S_{1/2,-1/2}$ state by 10 674 nm pulses from $S_{1/2,1/2} \rightarrow D_{5/2,-3/2}$ for 30 μs with 80 μs repumping 1033 nm interleaved, which excites it to $P_{3/2,-3/2}$, from where it can only decay to $S_{1/2,-1/2}$. The disappearance of the $S_{1/2,1/2}$ peak on performing the qubit spectroscopy shows successful state preparation with the measured state preparation fidelity of 97%.

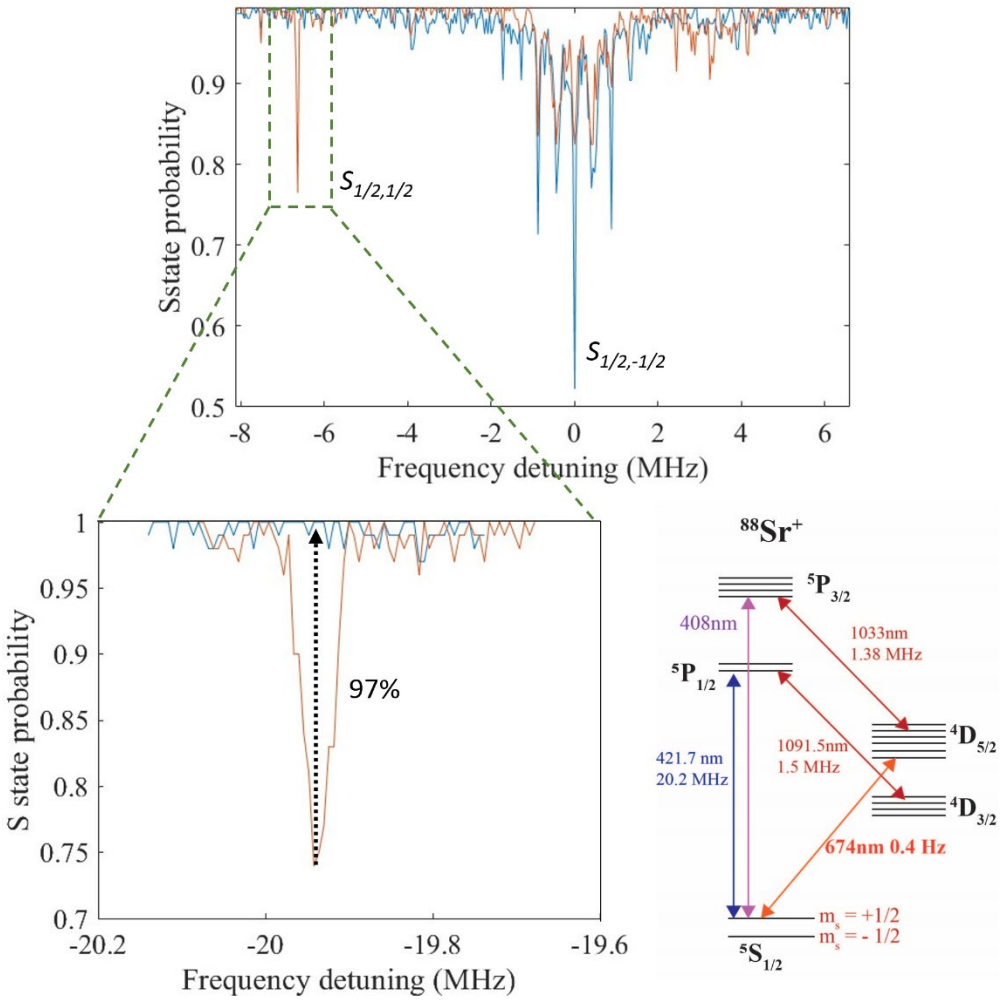

Figure 5.6 State preparation: Wide spectroscopy was performed before and after the state preparation with 97% fidelity to demonstrate the feasibility of coilR-locked 674 nm for qubit state preparation.

5.3.4 Rabi oscillations

The quadrupole transition of Sr has been used as an optical qubit and an atomic clock. To test the ability of the coilR stabilized at 674 nm for optical qubit or clock, Rabi oscillations on one of the carrier electronic transitions were performed, and weak contrast corresponding to single qubit gates with a maximum of 80% fidelity was observed. This fidelity can be improved by improving the laser ILW by locking the S1 to coilR and by cooling the ion to the motional ground state.

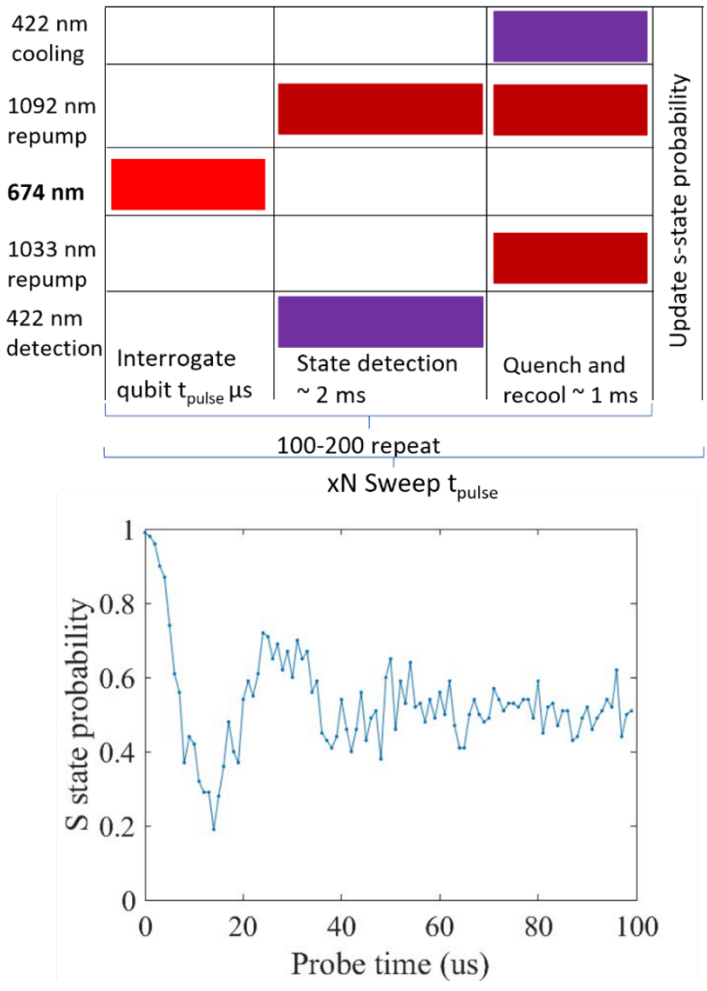

Figure 5.7 Rabi Oscillations: Pulse sequence for Rabi oscillations and plot showing 80% contrast of first Rabi pulse for $S_{1/2, -1/2} \rightarrow D_{5/2, -5/2}$ qubit.

5.3.5 Ramsey interferometry

Ramsey interferometry is performed to disentangle the sources of decoherence, which limits the single-qubit fidelity. The optical quadrupole transition from the $S_{1/2} \rightarrow D_{5/2}$ state imparts momentum during excitation, and the Rabi frequency depends on the motion state of the ion. For an ion that is not cooled to the ground state of the trap, the different Rabi frequencies shot-to-shot create an effective amplitude noise on the qubit rotations, which can wash out the Rabi flop contrast. However, the Ramsey contrast is not limited by this, as the first $\pi/2$ pulse of the qubit has a fixed susceptibility to the effective amplitude noise that does not grow with delay time if the heating rate is not high.

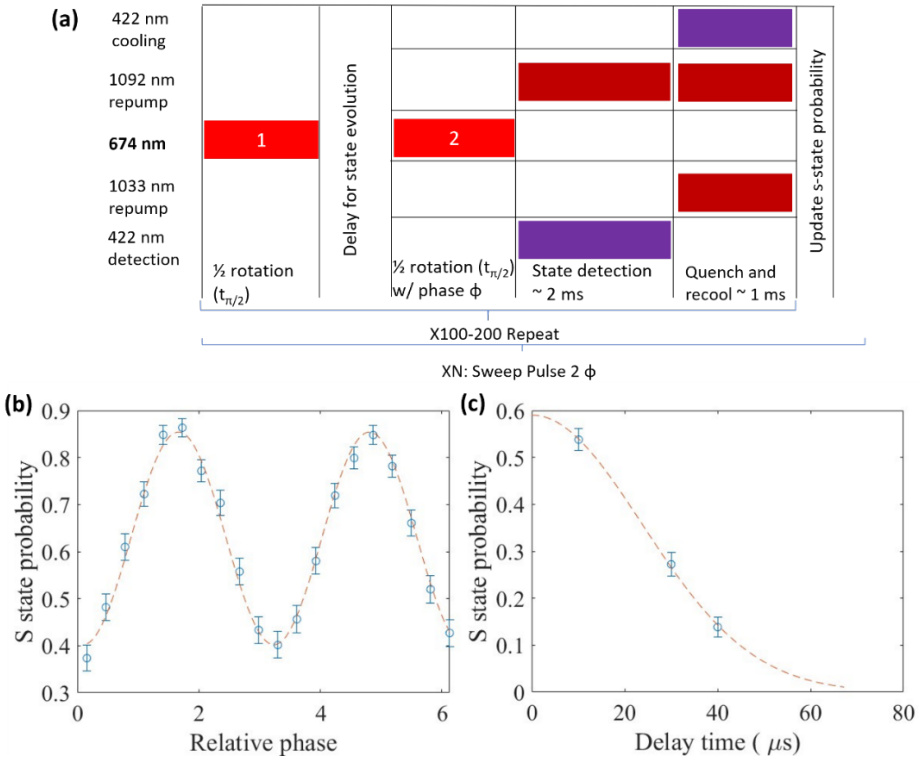

Figure 5.8 Ramsey interferometry: (a) Pulse sequence for Ramsey interferometry (b) Ramsey contrast vs the relative phase of the two $\pi/2$ pulses, total time 10 μs. (c) Ramsey contrast vs. delay time measured with the ion, with $\pi/2$ pulses between the $S_{1/2,-1/2} \rightarrow D_{5/2,-5/2}$ states of the trapped ion qubit with the coilR stabilized 674 nm laser, with optical pumping.

5.4 Conclusion

We utilized our coilR-stabilized 674 nm laser for various operations with $^{88}Sr^{+}$ ions relevant to qubit operations. These experiments are in progress, and better state-preparation fidelities approaching 99% are expected as the setup improves. Moreover, the addition of SBS as a pre-stabilization cavity will further improve the ILW of the 674 nm stabilized laser, and the ILW might approach 100 Hz. The drift of the coilR may become the limiting factor, and better techniques such as dual-mode thermometry may be required for better drift reduction [166]. This coil-stabilized cavity opens the doors to compact and highly scalable realization of state preparation and manipulation lasers for $^{88}Sr^{+}$ Zeemann qubits. SBS pre-stabilization will further enable optical qubits and compact portable optical atomic clocks based on $^{88}Sr^{+}$ and can be easily extended to other species, such as 698 nm for the compact ^{87}Sr clock and 778 nm for the compact ^{87}Rb two-photon clock.

Chapter 6: Photonic large area grating emitters for 3-D MOT

6.1 Introduction

Cold atoms [167], a central component for precision scientific tools including atomic clocks [15] and ultra-high resolution spectroscopy [168,169] are emerging as basic building blocks for emerging applications including quantum computing [41,65]. The ability to cool atoms to ultra-low temperatures removes effects that limit the spectroscopy resolution and enables the observation of the quantum behavior of atoms [170]. The cooling of neutral atoms is accomplished using light to slow the atoms down to near-zero velocity and further cool them using an electromagnetic field [170]. However, neutral atom cooling systems require complicated free-space lasers and optics that occupy large tables and racks, and are costly and power consuming. New photonic integrated circuit technologies will enable a drastic reduction in the size, power, and cost of atom cooling systems and enable the wider scale application of these precision techniques.

Magneto optic traps (MOTs) [167,170–172] are widely used to create a large population of cooled atoms that can be trapped for a significant time duration for use in further stages of measurement or manipulation. A typical 3-dimentsional (3D) MOT consists of a vacuum cell with optically transparent windows and a mechanism for introducing the atomic species of interest. MOTs utilize a complex arrangement of free-space laser beams external to the vacuum cell, which are carefully aligned using precision bulk optics and properly configured magnetic-field gradient coils. External counter-propagating laser beams at a wavelength slightly red-shifted from the atomic species absorption line are coupled through

the cell windows and converge at the desired atom trap location. The magnetic field is introduced using coils that are aligned to form a field null at the intersection of optical cooling beams with large cross-sectional areas [171].

Efforts to miniaturize 3D MOTs have utilized micro-optic components such as conical mirrors or volume Bragg gratings and prisms to convert a collimated free-space laser beam into three intersecting beams within the MOT [173,174]. Further size reduction using a conical mirror with chip surface gratings patterned onto a 2D substrate has been reported. The photonic integrated circuit (PIC) technology offers a rich set of passive and active components to further reduce the size, power, and cost of an MOT and improve the performance of atom cooling systems. To date, there has been limited success in migrating atomic systems to PIC technology. Recently, a silicon nitride (Si_3N_4) PIC was shown to transform 780 nm light from a waveguide to a free-space beam via an on-chip surface grating with an off-chip beam waist of 160 μm [175], and subsequently used as an optical probe beam to demonstrate Rb spectroscopy [176] in a miniaturized 1-D MOT [177]. More recently, metasurface baser diverging beam emitters have been reported, which are illuminated directly by fibers [178]. PIC integration of a 3D-MOT requires the conversion of guided light to multiple free-space, large-area laser cooling beams that converge within the atom vapor cell at proper angles for atom cooling. Such PIC technology requires significant advancement in extremely large-area gratings integrated with waveguides and other on-chip components, as well as compatibility with the miniaturization of other 3D-MOT components.

This chapter demonstrates a 3D MOT laser interface PIC that transforms 780 nm light from a single waveguide input into three large-area, non-diffracting, free-space beams via an ultra-large area (4 mm × 5 mm) partially etched, chirped, and apodised gratings. The 3D MOT

interface PIC achieved a mode expansion factor of ~ 20 × 106, a factor greater than 40x larger than that previously reported [175]. This level of performance eliminates the need for bulky beam splitters, Galilean telescopes, and collimation lenses and replaces an array of table-top bulk optical components. The PIC produces three non-diverging Doppler cooling beams from large-area surface gratings at an angle of 54.7°, intersecting orthogonally 9 mm from the chip surface within the Rb vacuum cell. A large working distance of 9 mm allows the PIC to be placed outside the cell for modular design. Part of this chapter was adapted with permission from our publications [14,69].

6.2 Design

6.2.1 Slab expander design

The beam expander is a wide taper of Si_3N_4 that allows the mode to expand freely inside it. Different waveguide core thicknesses result in different beam expander lengths, owing to the different effective refractive indices of the modes. A thinner core results in exceedingly long tapers, which are impractical because they require stitching multiple masks for a single slab expander. A thicker core helps to make the beam expander more compact owing to the higher index contrast. In addition, the bend radii also have to be considered, as thinner cores have a larger minimum bend radius, resulting in larger devices.

A commercially available simulation software was used to model the expansion of the beam inside the taper for different core thicknesses. The simulation was performed for core thicknesses of 40 nm, 90 nm, and 120 nm with waveguides designed for each core thickness entering a taper of identical length and width. The TE0 mode of the waveguides was used for

the device design; however, it can also be performed for the TM0 mode. For the 40 nm and 90 nm core modes, the beam propagation method (BPM) was used to observe the mode diameter in the taper, while eigenmode expansion (EME) was used for the 120 nm core. Figure 6.1 (a) and (b) show the schematic of the expander and one simulation of the beam expansion in the expander.

The length of the slab required for a 4 mm beam diameter is extremely long (>20 mm) for the 40 nm core but is more reasonable in the 90 nm core and even smaller in the 120 nm core. The length of the expander required for the 4 mm beam waist was 11.43 mm for the 90 nm core and was our initial design choice, although the same mask was used in the 120 nm core for a larger beam size from the same grating partial etch.

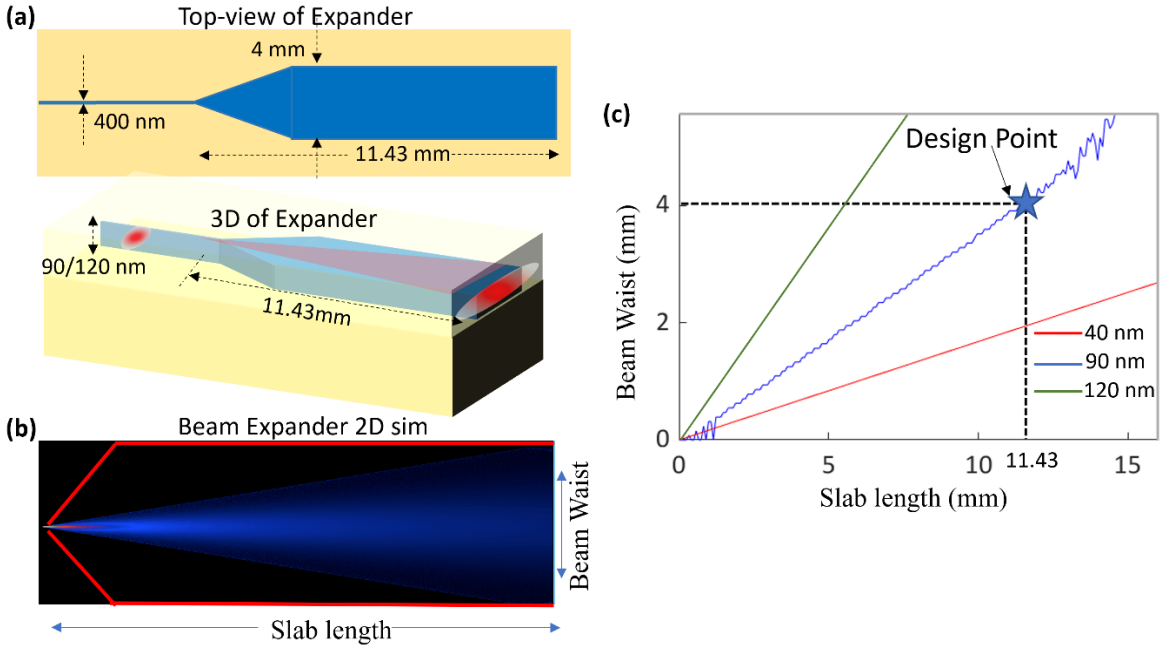

Figure 6.1 Slab expander design: (a) Schematic of the Slab expander. (b) 2D simulation of beam expansion in the expander. (c) Beam waist vs. length of slab expander for different core thicknesses.

6.2.2 Grating emitter design

The three beams that generate the atom-trapping and cooling used in our 3D-MOT are formed using three large-area, chip-to-free-space, weakly diffracting, chirped, and apodised grating couplers. These couplers were formed in a material system composed of a silicon nitride device layer and two silicon dioxide cladding layers. Historically, grating couplers have been used in integrated photonics for a relatively small subset of tasks, the most well-known of which is likely the coupling of light between chip-scale waveguides and optical fibers. Grating couplers are an easy method for interfacing planar devices and their surrounding environment because, through careful control over the k-vector of the grating, the angle at which light is either emitted or received can be targeted with a high degree of precision. When light propagating within a chip diffracts from a grating written into its path, the angle at which the light diffracts relative to the surface normal of the chip can be calculated analytically. If we assume that the light initially propagates within the x-y plane and that the z-axis represents the direction normal to the chip's surface, then the diffraction angle is given as

$$\theta = \text{atan}\left(\frac{\sqrt{{kx_o}^2 + {ky_o}^2}}{kz_o}\right) \tag{6.1}$$

Where:

$$\begin{aligned} kx_o &= kx - Kx \\ ky_o &= ky - Ky \\ kz_o &= kz - Kz \end{aligned} \tag{6.2}$$

$$kz_o = \sqrt{(2\pi\lambda)^2 - {kx_o}^2 + {ky_o}^2}$$

In these expressions, kx and ky are the x- and y-components of the initial k-vector of the light, and Kx and Ky are the x- and y-components of the grating's k-vector, respectively. Additionally, kx_o, ky_o, and kz_o represent the three components of the diffracted light's k-vector in free-space. For the 3D MOT, the three beams diffracted from the chip are required to be orthogonal to one another, and this translates in turn to the requirement that, for each grating, the diffraction angle relative to the surface normal is 54.7°.

To achieve an expanded beam size, we introduce an abrupt waveguide-to-slab mode transition within the chip. At the interface between the waveguide, which provides two-dimensional confinement, and the slab, which only provides confinement along one axis, the optical wave begins to diverge along the direction that is both transverse to its propagation and parallel to the surface normal of the chip. This divergence is represented mathematically as a spatially dependent distribution of k optical vectors, given as

$$\begin{aligned} kx(x,y) &= k_o \cos(y/x) \\ ky(x,y) &= k_o \sin(y/x) \end{aligned} \tag{6.3}$$

In this expression, x and y are the coordinates within the nitride slab relative to the point at which waveguide-to-slab transition occurs. This means that because the light is required to be emitted in a specific direction regardless of position, the grating coupler's k-vector must vary spatially to compensate for the varying components of the optical k-vector. This requirement can be mathematically represented as

$$\begin{aligned} Ky &= ky - k_o \sin\left(\operatorname{atan}\left(\frac{y}{x}\right)\right) \\ Kx &= kx - \frac{k_o \tan(54.7^0)}{\sqrt{1+\tan(54.7^0)}} \end{aligned} \tag{6.4}$$

After these local maps of the grating period and direction are calculated, the spatially variant

grating may be generated numerically by beginning a single grating line at a chosen starting point and "walking forward," iteratively defining its movement and width. This process can be repeated for an arbitrary number of grating lines until the chosen grating area is defined. Thus, we generated curved gratings that take the slab mode and produce a flat intensity profile in free space. We include both chirped and un-chirped gratings in our test structures because un-chirped gratings are easier to fabricate, but chirped gratings are required to produce a uniform intensity profile in the propagation direction. Figure 6.2 shows a schematic of the grating design. We also designed test structure small gratings with splits of period to calibrate the simulations with the fabrication in a 90 nm core and determined 1.08 μm as the optimum period for a 50% duty cycle. The grating chirp was limited to 25-75% duty cycle due to fabrication constraints using an ASML DUV 248 nm stepper whose resolution is ~ 200 nm, and anything below 300 nm has a chance of not being properly resolved.

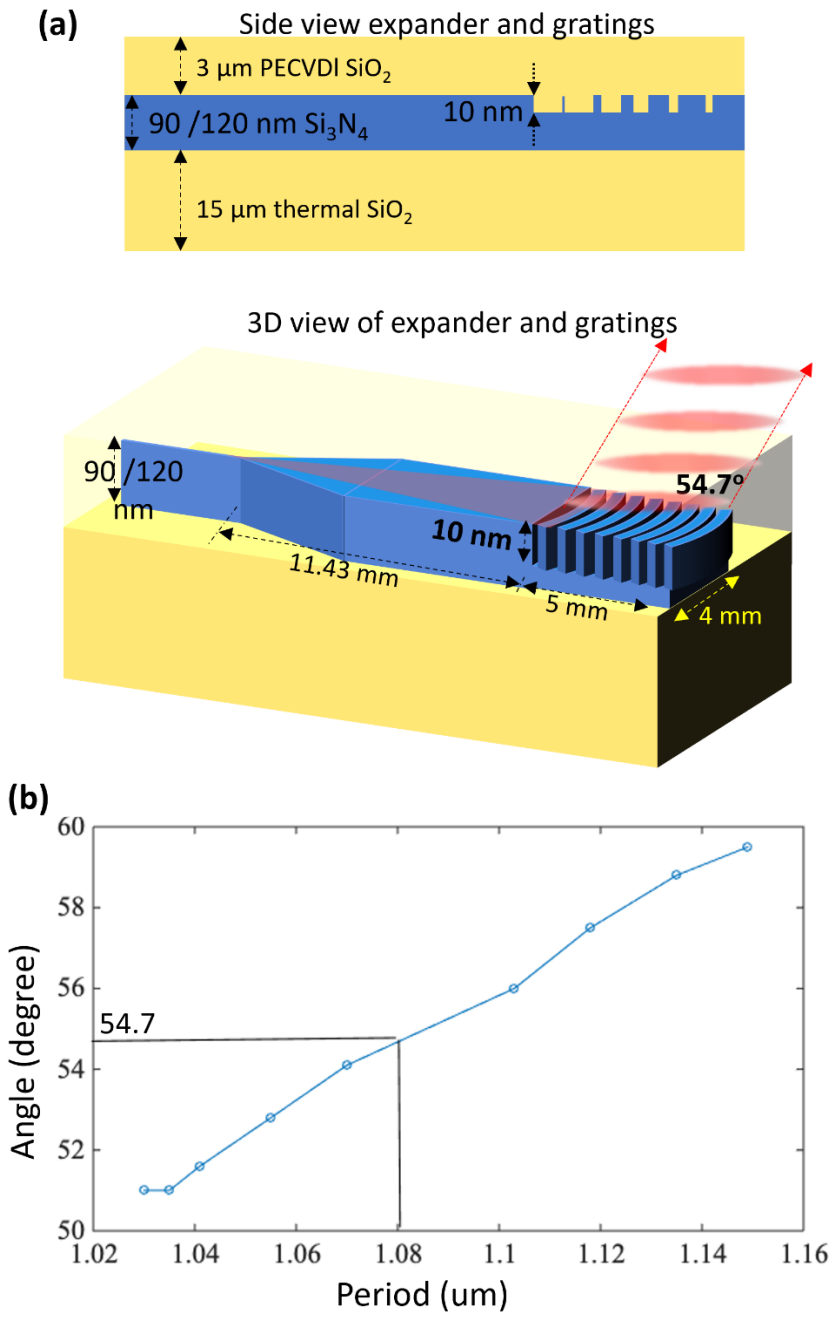

Figure 6.2 Grating design: (a) Sideview of grating showing material stack and partial etch along with 3D schematic of the grating. (b) Measurement of the test structure period split to calibrate the design with the fabricated device.

6.2.3 3D MOT PIC design

A schematic of a 3D MOT with a 6-beam configuration is shown in Figure 6.3. A single fiber coupled waveguide input is required for the MOT PIC. A 1 × 3 mmi split the input equally into three to feed the three gratings. The bends were designed to have a radius of 500 µm, which is sufficient to avoid bend loss. The three beams originated from the bottom of the MOT PIC at ~54° (from the surface normal) and were placed 120° from each other to provide three orthogonal beams. There are three quarter waveplates to convert polarization from linear to circular lying flat on the PIC, and the three beams are retroreflected back on themselves to form the three counter-propagating pairs. The magnetic field is provided by a traditional pair of Helmholtz coils placed along the beam on the outside of the PIC and is not shown here, although a PCB-based planar coil can be used [179]. Our PIC-based implementation realizes a true six-beam 3D MOT in contrast to prior non-integrated approaches that used a free-space illuminated surface grating pyramidal MOT design [180] and flat top beams instead of the commonly used Gaussian beam profile.

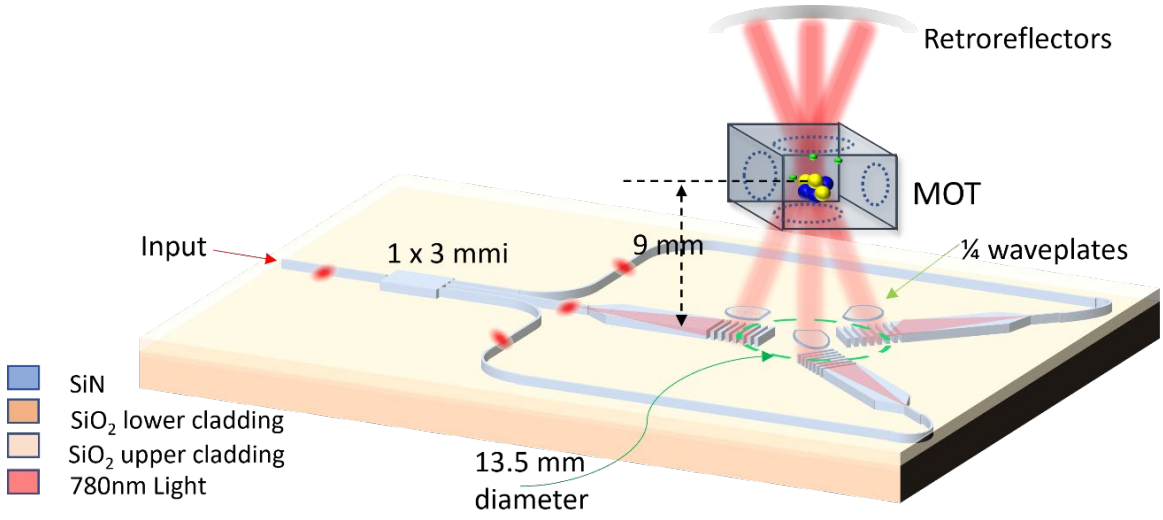

Figure 6.3 MOT PIC schematic: Schematic of complete MOT PIC with single input and mmi feeding the three slab expanders placed 120° from each other on a 13.5 mm circle ending in three

grating emitters emitting at 54.7° from each other providing three orthogonal large area cooling beams., the gratings are lensed, chirped and apodized which is not reflected in this figure.

6.3 MOT PIC fabrication

The starting wafer was a 1 mm thick 4-inch diameter silicon wafer with 15 μm of thermally grown oxide. The waveguide core consisted of stoichiometric LPCVD Silicon Nitride (Si_3N_4). Two wafer splits with waveguide core thicknesses of 90 nm and 175 nm were fabricated. The entire process was a two-mask fabrication, one for the waveguide and the other for the grating, as it required a partial etch of 10 nm in a 90 nm core. Both the waveguide and grating were patterned using a 248 nm DUV stepper. They were then etched with an Inductively Coupled Plasma-Reactive Ion Etcher using an optimized $CHF_3/CF_4/O_2$ etch chemistry developed at the UCSB, one for the waveguide etch [17,18], and one for the grating etch, which was developed specifically for these devices. Subsequently this, 6um of SiO_2 upper cladding was deposited using a PECVD process with TEOS as a precursor. Etch calibration was performed on the grating etch to identify the optimal conditions for an etch depth of 10 nm. This was performed by running four different etching conditions on four quadrants of a 4" wafer. One calibration condition resulted in 9.8 nm and the same etch conditions were used during the etching of actual devices. On performing AFM on the gratings in the actual devices, the deviation from the target 10 nm etch was found to be 1-2 nm. The fabrication process is shown in Fig. 6.4. In addition, a dark-field image of the fabricated waveguides and an atomic force microscope (AFM) of the gratings were obtained.

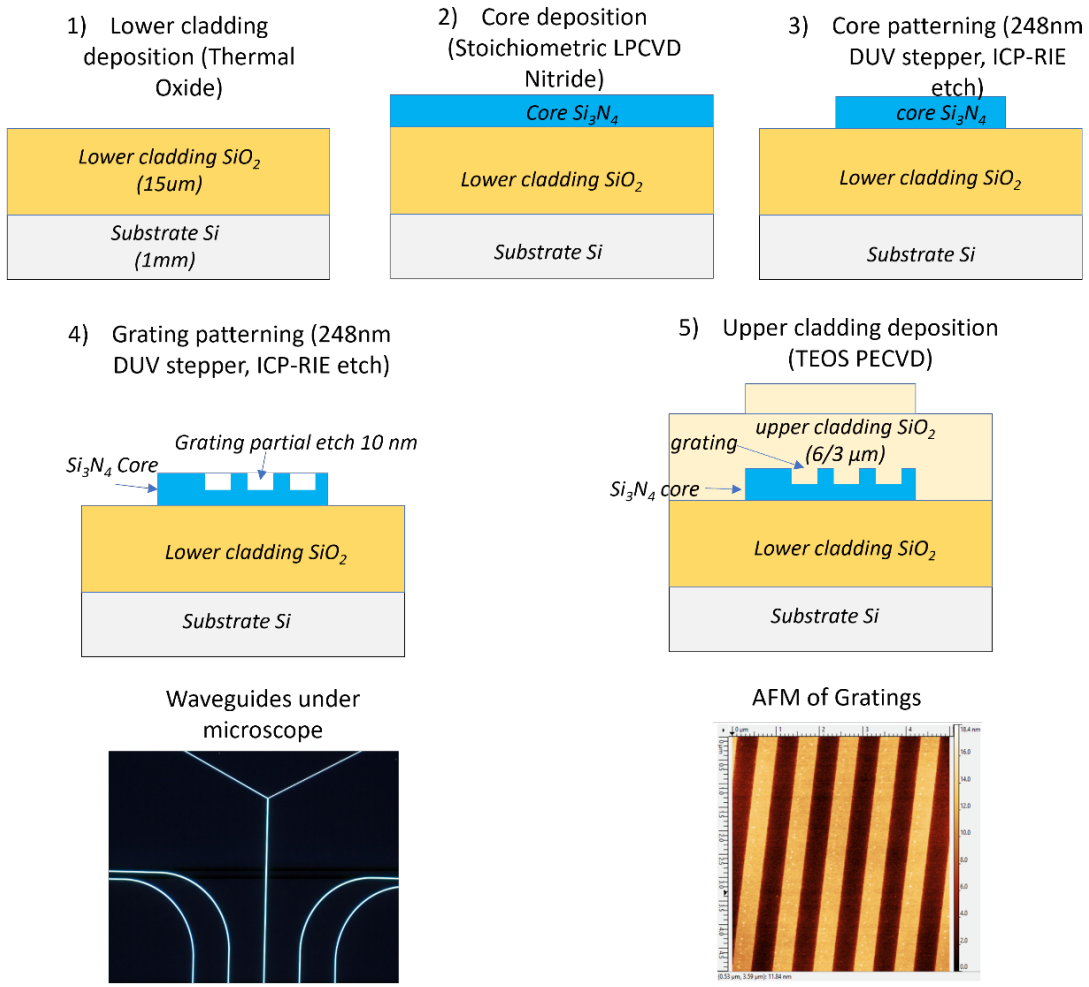

Figure 6.4 Grating fabrication flow: Steps in the fabrication of the MOT PIC with partially etched gratings, also shown in the images of the fabricated waveguide and the AFM of the grating.

6.4 MOT PIC characterization

Two devices were fabricated with the same mask design: one with a 90 nm thick core and one with a 120 nm thick core. To quantify the grating emission from these PICs, the beam waist and intensity profile for the x- and y-lateral cross sections were measured by imaging the beams at varying distances from the PIC on a camera or on a screen.

90 nm core MOT PIC measurements: The measured beam waist is plotted as a function of distance, showing that the beams have very low divergence angles of 0.35 °and 0.18 °for the x and y directions perpendicular to the direction of propagation. This represents a divergence half-angle $\theta < 1$ °in both dimensions. An example image of the beam at a distance of 6 mm from the PIC, as well as the cross-sectional profiles, demonstrates high-quality beam uniformity (Figure 6.6). The measured free-space beam width of 3.8 mm x 2.0 mm is an optical mode area expansion factor of 18.2 x 10^6 from the 0.444 μm^2 area waveguided mode.

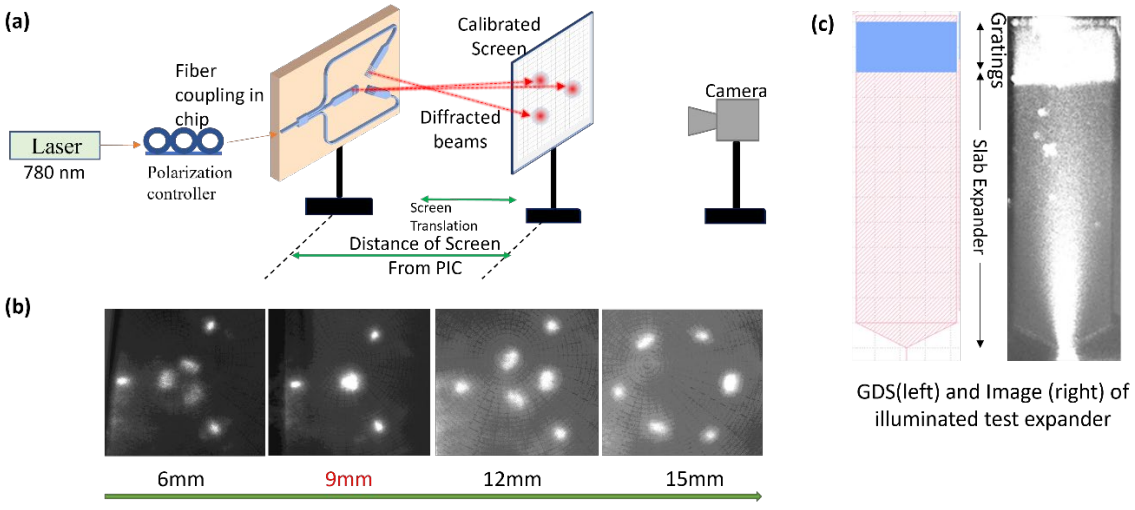

Figure 6.5 90 nm core MOT PIC characterization images: (a) Setup schematic for measuring beam size and divergence. (b) Measured beam profile on the screen as the gap between the screen is varied, six spots are seen with the smaller spots being higher-order modes. The 0^{th} order beams intersect at 9 mm, as designed. (c) GDS of a single slab with grating along with image of fabricated single grating showing a 780 nm beam expanding inside the slab and then diffracting from the grating.

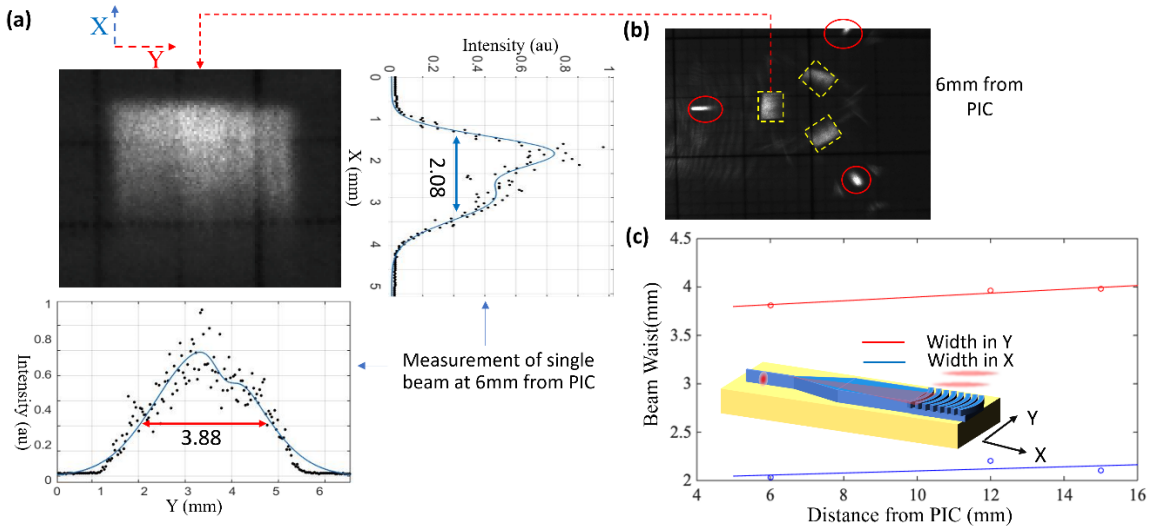

Figure 6.6 90 nm core MOT PIC characterization beam size and divergence: (a) Fitting Gaussian profile in the two axes to obtain 3.88 mm x 2.08 mm beam size. (b) Image of beams at 6 mm gap used to extract the beam profile in a. The yellow square represents 0 order diffraction, whereas the red circle represents the higher-order mode. (c) Divergence of beams with distance from PIC MOT in both axes.

120 nm core MOT PIC measurements: The measured beam waist is plotted as a function of distance, showing that the beams have very low divergence angles of 0.35° and 0.16° in the x- and y-directions, respectively, perpendicular to the direction of propagation. This represents a divergence half-angle of $\theta < 1°$ in both dimensions. The M^2 values were 10 and 15, as these are flat-top beams. An example image of the beam at a distance of 6 mm from the PIC, as well as the cross-sectional profiles, demonstrates high-quality beam uniformity (Figure 6.6). The measured free-space beam width of 3.5 mm x 2.5 mm is an optical mode area expansion factor of 20×10^6 from the 0.444 μm^2 area waveguided mode. The effective Rayleigh lengths were 125 cm and 113 cm, respectively. This MOT PIC was successfully used to demonstrate Rb-87 MOT with over a million atoms trapped at a temperature of ~ 200 μK [14] but will not be discussed in detail here.

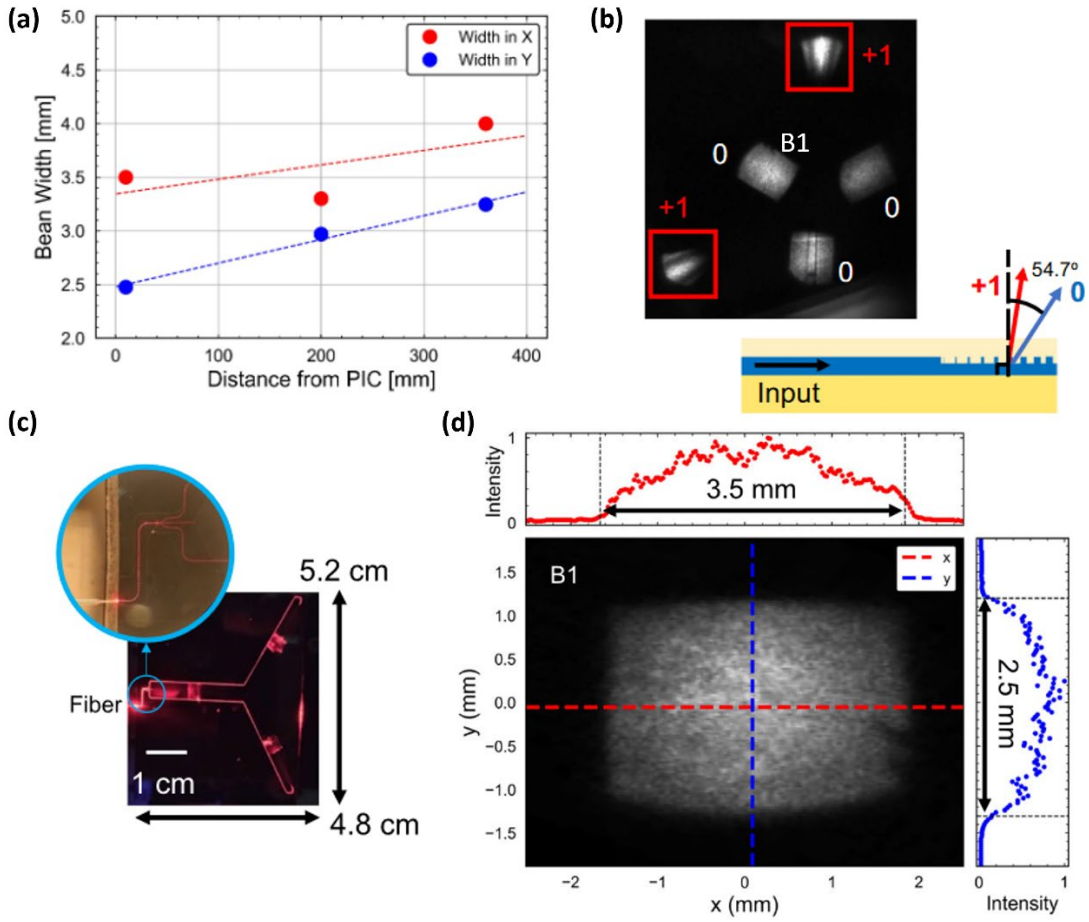

Figure 6.7 120 nm core MOT PIC characterization: (a) Divergence of the beam in both the axis. (b) Beam profile 5 mm from the MOT PIC surface showing the 0 order and 1st order beams. (c) Image of red laser coupled to the MOT PIC showing propagation and the illuminated gratings. (d) Mode profile of one of the beams from b.

Power Budget: The average power loss from the fiber input to each free-space beam output was 21.4 dB, corresponding to a total optical loss of beam delivery (fiber input to the sum of the beams) of 15.8 dB. These losses include fiber-to-waveguide facet loss, mmi splitter excess loss, grating loss, and waveguide propagation losses. The losses of the 90 nm core PIC MOT device were also similar. The cutback method was used to determine loss and individual components as fiber facet coupling 3.8 dB, 1 x 3 mmi excess loss 3.3 dB, waveguide to slab expander 0.7 dB, slab to free space grating emitter 8 dB. There is no taper at the facet or from

the waveguide to the slab interface. The facet loss can be reduced to 0.3 dB by using advanced facet couplers, as in [181]. We designed 1 × 3 evanescent directional couplers that reduce the excess loss to 0.4 dB. Further grating optimization might require higher-resolution fabrication and potentially full grating inverse design and fabrication using e-beam lithography to reduce grating losses and eliminate grating higher-order modes.

6.5 Conclusions

This chapter demonstrates a compact silicon nitride PIC-based 3-D MOT for cooling ^{87}Rb atoms. The laser cooling beam PIC interface demonstrates a record beam expansion factor of 20×10^6. The cooling beams were generated with three ultra-large-area-mm-sized area mm size gratings that emitted collimated light at an angle of 54.7 °to the PIC normal and intersected in the atomic vacuum cell 9 mm from the PIC surface. The modular MOT design in the future can be combined with PIC technology and a planar magnetic coil design to generate a magnetic zero at the cooling beam intersection inside an atomic vacuum cell for a fully planar, compact, modular, and robust system. The laser-cooling PIC can readily be adapted for other visible wavelengths owing to the transparency of the silicon nitride waveguides from 405 nm to 2350 nm, as well as hybrid integration with on-chip laser and detector technology. This opens up the potential for cooling other atomic species and transitions, as well as more complex laser cooling and interrogation designs; for example, ^{87}Sr atoms require two stages of cooling: probe, spectroscopy, clock, and magic-λ lattice beams from the same PIC. Further integration with narrow linewidth lasers and self-referenced optical frequency combs designed in silicon nitride platforms can enable compact clocks in

which all laser delivery, interrogation, and probing are integrated into a PIC, which will result in the next generation of sensors and space-based applications.

Chapter 7: Summary and Future Work

7.1 Thesis Summary

This thesis reports visible stabilized sources for atomic and quantum applications. The stabilized source consists of the first integrated Brillouin laser and coil stabilization cavities at visible wavelengths. These are enabled by the lowest loss and highest Q waveguides and resonators at visible wavelengths, which are also demonstrated in this study. Moreover, a coil stabilized SBS was used for performing state preparation and spectroscopy for $^{88}Sr^{+}$ as an application of these stabilized lasers. A large-area grating was also demonstrated for cooling neutral atoms in an MOT.

The low-loss waveguides are shown in blue, 450 nm to near IR, 808 nm for the TE0 mode, and 493 nm to 780 nm for the TM0 mode. The TM0 mode waveguides are the first < 1 dB/m loss waveguides at visible wavelengths with minimum losses of 0.36 dB/m at 780 nm and the resonators are first resonators with > 100 million Q in red and near IR, with Qs of 100 million at 698 nm and 145 million at 780 nm.

The SBS lasers have moderately low threshold of 10 mW at 674 nm, 7 mW at 698 nm and an extremely low threshold of 0.8 mW at 780 nm. We also observed cascading typical of the SSB process in the lower threshold 780 nm SBS. The Fundamental linewidths of the three SBS lasers were in 8-20 Hz with suppression factors of 500x – 3500x for the fundamental linewidth. The power dynamics of these SBS lasers matched well with those of their simulations. These SBS lasers also demonstrate integral linewidth reduction of an order of magnitude.

Coil resonators are demonstrated at 1319, 698, and 674 nm for PDH linewidth reduction with a PDH lock. The coilR has a 4 m resonator length at 1319 nm and achieves TRN-limited performance for this wavelength. The coilR is 3 m long at 698 nm and demonstrates about 10-50x integral linewidth reduction to and 2-4 orders of magnitude of frequency noise reduction. OFD was performed to measure the FN at 698 nm and 1319 nm. In the future, beatnote measurements can be performed for a more accurate integral linewidth by measuring the accuracy close to the carrier noise. For 674 nm, the coilR is 3 m in length and demonstrates 2-4 orders of magnitude of frequency noise reduction. Both OFD and beatnote measurements were performed to give a 4 kHz integral linewidth with the $1/\pi$ reverse integral method and 8 kHz with the β-separation method.

The coilR stabilized at 674 nm from above was used with $^{88}Sr^{+}$ to perform spectroscopy and a 12.8 kHz linewidth was extracted from it. State preparation was performed with 95% fidelity. Rabi oscillations and Ramsey interferometry have also been reported. These results are the first demonstration of ion operation with an integrated cavity-stabilized laser.

Finally, large-area gratings were demonstrated to provide millimeter-scale beams intersecting orthogonally to provide cooling and trapping beams for a neutral atom 3D MOT. The design provides 20 million times increase in mode area from 0.44 μm^2 in waveguide to three beams of 3.5 mm x 2.5 mm in free space. All the above devices will enable ‘beam line’ PICs which will process and provide required optical wavelengths for atomic, ion and molecule based experiments, improving SwaP budget and new ways to improve performance and scalability of these systems.

7.2 Potential future work

The waveguides and SBS in this work are the first generation of devices, and more optimizations can be performed to improve performance as well as to combine different devices to obtain better functionality. Cascading suppressed SBS resonators design [134] and design of large cavity volume coilR SBS resonator can be done for an even lower fundamental linewidth. For waveguides, material properties and optimizations were not performed and can be explored to further reduce losses.

An immediate near-term future work is to lock the SBS laser's output to the coilR, as envisioned but not executed in this work, to obtain a TRN-limited narrower ILW source for higher fidelity ion and clock operations with 674 nm and 698 nm, respectively. Plotting the pump, measured SBS laser, and the pump locked to the coilR shows that the coilR-locked pump is approximately 10 dB higher in the FN than the TRN, while the SBS individually provides a 10x reduction in ILW, as shown in Figure 7.1. Using the SBS as an intermediate stabilization can be a viable way to achieve a limited, sub 100 Hz integral linewidth. S2 suppressed the operation of these SBS resonators using photonic molecules [134], multimode SBS operation, and a new method using a two-point coupler can also be explored.

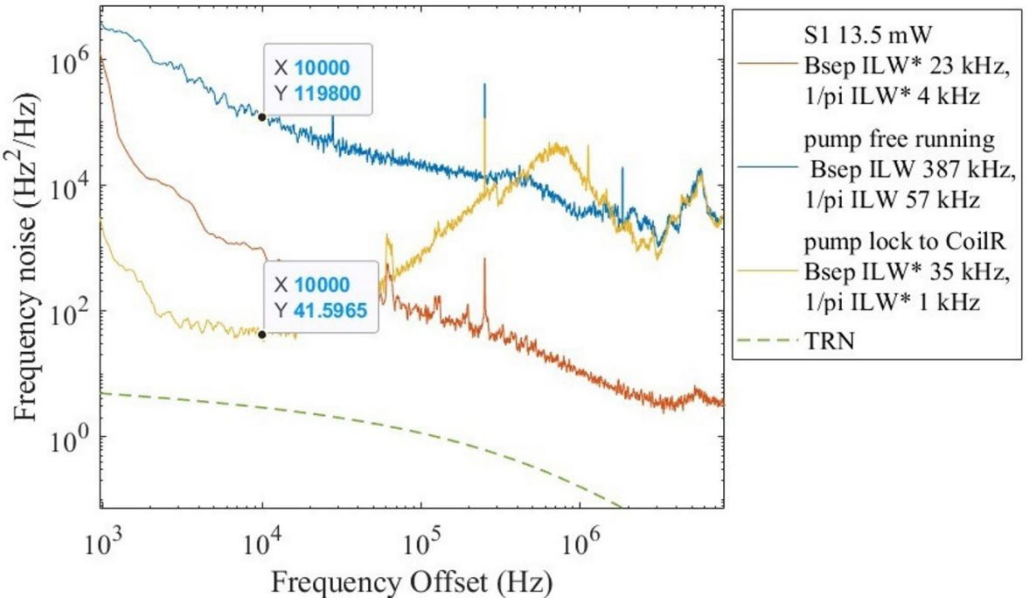

Figure 7.1 698 nm Pump, SBS and TRN: The FN of the pump that is used for SBS and locked to coil independently along with TRN floor of the coilR showing potential for future improvement with an SBS laser locked to coilR.

Moreover, these high-Q SBS resonators are also ideal for self-injection locking [182], and combining SBS with SIL can lead to a phase-robust SIL that has been demonstrated in fiber [183] and will require a chip 25 GHz phase shifter, which might be possible from thin-film $LiNbO_3$ that has been demonstrated at near red and near IR wavelengths [27]. SIL has been claimed to provide isolator-free operation [184], and combining it with SBS might provide even higher isolation when odd Stokes modes are used as they are counterpropagating and can be filtered out with a filter between the laser and SBS ring. SIL can be attempted with a coil resonator for an ultra-low FLW laser and locked to another coil for ILW stabilization [155]. Moreover, new physics and interesting interactions that were not previously known might be possible through the interaction between the two.

Finally, a fully integrated PIC for processing the wavelength required for AMO, including lasers, modulators, filters, shutters, and photodiode stabilization cavities, can be integrated on a heterogeneous chip with low-loss Si_3N_4 waveguides; passive and stabilization cavities are closer than ever to reality and will serve to revolutionize compact and portable systems, improve the scalability of quantum systems, and provide performance benefits leading to new science in state-of-the-art lab-based systems.

References:

1. A. Debut, S. Randoux, and J. Zemmouri, "Linewidth narrowing in Brillouin lasers: Theoretical analysis," Phys. Rev. A **62**, 023803 (2000).
2. R. O. Behunin, N. T. Otterstrom, P. T. Rakich, S. Gundavarapu, and D. J. Blumenthal, "Fundamental noise dynamics in cascaded-order Brillouin lasers," Phys. Rev. A **98**, 023832 (2018).
3. G. Huang, E. Lucas, J. Liu, A. S. Raja, G. Lihachev, M. L. Gorodetsky, N. J. Engelsen, and T. J. Kippenberg, "Thermorefractive noise in silicon-nitride microresonators," Phys. Rev. A **99**, 061801 (2019).
4. E. D. Black, "An introduction to Pound–Drever–Hall laser frequency stabilization," American Journal of Physics **69**, 79–87 (2001).
5. M. Nickerson, "A review of Pound-Drever-Hall laser frequency locking," 7 (n.d.).
6. N. Chauhan, C. Caron, J. Wang, A. Isichenko, N. Helaly, R. J. Niffenegger, and D. J. Blumenthal, "Qubit operations with photonic coil resonators," under preparation (n.d.).
7. N. Chauhan, A. Isichenko, K. Liu, J. Wang, Q. Zhao, R. O. Behunin, P. T. Rakich, A. M. Jayich, C. Fertig, C. W. Hoyt, and D. J. Blumenthal, "Visible light photonic integrated Brillouin laser," Nat Commun **12**, 4685 (2021).
8. M. Corato-Zanarella, A. Gil-Molina, X. Ji, M. C. Shin, A. Mohanty, and M. Lipson, "Widely tunable and narrow-linewidth chip-scale lasers from near-ultraviolet to near-infrared wavelengths," Nat. Photon. 1–8 (2022).
9. W. Zhang, F. Baynes, S. A. Diddams, and S. B. Papp, "Microrod Optical Frequency Reference in the Ambient Environment," Phys. Rev. Appl. **12**, 024010 (2019).
10. D. J. Blumenthal, "Photonic integration for UV to IR applications," APL Photonics **5**, 020903 (2020).
11. N. Chauhan, J. Wang, D. Bose, K. Liu, R. L. Compton, C. Fertig, C. W. Hoyt, and D. J. Blumenthal, "Ultra-low loss visible light waveguides for integrated atomic, molecular, and quantum photonics," Opt. Express, OE **30**, 6960–6969 (2022).
12. D. J. Blumenthal, N. Chauhan, A. Isichenko, J. Wang, D. Bose, K. Liu, and M. W. Harrington, "Visible Light Photonics for Atomic and Quantum Sensing and Computation," in *Optica Quantum 2.0 Conference and Exhibition (2023), Paper QTu4C.1* (Optica Publishing Group, 2023), p. QTu4C.1.
13. D. J. Blumenthal, N. Chauhan, A. Isichenko, K. Liu, and J. Wang, "Integrated stabilized lasers and circuits for atom cooling, trapping, and interrogation," in *Quantum Sensing, Imaging, and Precision Metrology*, S. M. Shahriar and J. Scheuer, eds. (SPIE, 2023), p. 71.
14. A. Isichenko, N. Chauhan, D. Bose, J. Wang, P. D. Kunz, and D. J. Blumenthal, "Photonic integrated beam delivery for a rubidium 3D magneto-optical trap," Nat Commun **14**, 3080 (2023).
15. A. D. Ludlow, M. M. Boyd, J. Ye, E. Peik, and P. O. Schmidt, "Optical atomic clocks," Rev. Mod. Phys. **87**, 637–701 (2015).
16. C. D. Bruzewicz, J. Chiaverini, R. McConnell, and J. M. Sage, "Trapped-ion quantum computing: Progress and challenges," Applied Physics Reviews **6**, 021314 (2019).
17. J. Kitching, S. Knappe, and E. A. Donley, "Atomic Sensors – A Review," IEEE Sensors J. **11**, 1749–1758 (2011).

18. H. J. Metcalf and P. van der Straten, "Force on Two-Level Atoms," in *Laser Cooling and Trapping*, H. J. Metcalf and P. van der Straten, eds., Graduate Texts in Contemporary Physics (Springer New York, 1999), pp. 29–37.
19. V. Letchumanan, P. Gill, E. Riis, and A. G. Sinclair, "Optical Ramsey spectroscopy of a single trapped Sr + 88 ion," Phys. Rev. A **70**, 033419 (2004).
20. B. J. Bloom, T. L. Nicholson, J. R. Williams, S. L. Campbell, M. Bishof, X. Zhang, W. Zhang, S. L. Bromley, and J. Ye, "An optical lattice clock with accuracy and stability at the 10−18 level," Nature **506**, 71–75 (2014).
21. J. A. Boyd and T. Lahaye, "A basic introduction to ultrastable optical cavities for laser stabilization," (2023).
22. T. Bothwell, C. J. Kennedy, A. Aeppli, D. Kedar, J. M. Robinson, E. Oelker, A. Staron, and J. Ye, "Resolving the gravitational redshift across a millimetre-scale atomic sample," Nature **602**, 420–424 (2022).
23. K. Liu, N. Jin, H. Cheng, N. Chauhan, M. W. Puckett, K. D. Nelson, R. O. Behunin, R. O. Behunin, P. T. Rakich, and D. J. Blumenthal, "Ultralow 0.034 dB/m loss wafer-scale integrated photonics realizing 720 million Q and 380 μW threshold Brillouin lasing," Opt. Lett., OL **47**, 1855–1858 (2022).
24. M. W. Puckett, K. Liu, N. Chauhan, Q. Zhao, N. Jin, H. Cheng, J. Wu, R. O. Behunin, P. T. Rakich, K. D. Nelson, and D. J. Blumenthal, "422 Million intrinsic quality factor planar integrated all-waveguide resonator with sub-MHz linewidth," Nature Communications **12**, 934 (2021).
25. X. Liu, A. W. Bruch, Z. Gong, J. Lu, J. B. Surya, L. Zhang, J. Wang, J. Yan, and H. X. Tang, "Ultra-high-Q UV microring resonators based on a single-crystalline AlN platform," Optica, OPTICA **5**, 1279–1282 (2018).
26. C. Sorace-Agaskar, S. Bramhavar, D. Kharas, W. Loh, P. W. Juodawlkis, J. Chiaverini, and J. M. Sage, "Multi-layer integrated photonics from the ultraviolet to the infrared," in *Frontiers in Biological Detection: From Nanosensors to Systems X* (International Society for Optics and Photonics, 2018), Vol. 10510, p. 105100D.
27. B. Desiatov, A. Shams-Ansari, M. Zhang, C. Wang, and M. Lončar, "Ultra-low-loss integrated visible photonics using thin-film lithium niobate," Optica, OPTICA **6**, 380–384 (2019).
28. T. J. Morin, L. Chang, W. Jin, C. Li, J. Guo, H. Park, M. A. Tran, T. Komljenovic, and J. E. Bowers, "CMOS-foundry-based blue and violet photonics," Optica, OPTICA **8**, 755–756 (2021).
29. G. N. West, W. Loh, D. Kharas, C. Sorace-Agaskar, K. K. Mehta, J. Sage, J. Chiaverini, and R. J. Ram, "Low-loss integrated photonics for the blue and ultraviolet regime," APL Photonics **4**, 026101 (2019).
30. M. Sinclair, M. Sinclair, K. Gallacher, M. Sorel, J. C. Bayley, E. McBrearty, R. W. Millar, S. Hild, and D. J. Paul, "1.4 million Q factor Si_3N_4 micro-ring resonator at 780 nm wavelength for chip-scale atomic systems," Opt. Express, OE **28**, 4010–4020 (2020).
31. L. Stefan, M. Bernard, R. Guider, G. Pucker, L. Pavesi, and M. Ghulinyan, "Ultra-high-Q thin-silicon nitride strip-loaded ring resonators," Opt. Lett. **40**, 3316 (2015).
32. J. A. Rushton, M. Aldous, and M. D. Himsworth, "Contributed Review: The feasibility of a fully miniaturized magneto-optical trap for portable ultracold quantum technology," Review of Scientific Instruments **85**, 121501 (2014).

33. A. D. Ludlow, T. Zelevinsky, G. K. Campbell, S. Blatt, M. M. Boyd, M. H. G. de Miranda, M. J. Martin, J. W. Thomsen, S. M. Foreman, J. Ye, T. M. Fortier, J. E. Stalnaker, S. A. Diddams, Y. L. Coq, Z. W. Barber, N. Poli, N. D. Lemke, K. M. Beck, and C. W. Oates, "Sr Lattice Clock at 1 × 10–16 Fractional Uncertainty by Remote Optical Evaluation with a Ca Clock," Science **319**, 1805–1808 (2008).
34. A. D. Ludlow, "The Strontium Optical Lattice Clock: Optical Spectroscopy with Sub-Hertz Accuracy," 251 (n.d.).
35. S. M. Dickerson, J. M. Hogan, A. Sugarbaker, D. M. S. Johnson, and M. A. Kasevich, "Multiaxis Inertial Sensing with Long-Time Point Source Atom Interferometry," Phys. Rev. Lett. **111**, 083001 (2013).
36. J. Grotti, S. Koller, S. Vogt, S. Häfner, U. Sterr, C. Lisdat, H. Denker, C. Voigt, L. Timmen, A. Rolland, F. N. Baynes, H. S. Margolis, M. Zampaolo, P. Thoumany, M. Pizzocaro, B. Rauf, F. Bregolin, A. Tampellini, P. Barbieri, M. Zucco, G. A. Costanzo, C. Clivati, F. Levi, and D. Calonico, "Geodesy and metrology with a transportable optical clock," Nature Phys **14**, 437–441 (2018).
37. C. Lisdat, G. Grosche, N. Quintin, C. Shi, S. M. F. Raupach, C. Grebing, D. Nicolodi, F. Stefani, A. Al-Masoudi, S. Dörscher, S. Häfner, J.-L. Robyr, N. Chiodo, S. Bilicki, E. Bookjans, A. Koczwara, S. Koke, A. Kuhl, F. Wiotte, F. Meynadier, E. Camisard, M. Abgrall, M. Lours, T. Legero, H. Schnatz, U. Sterr, H. Denker, C. Chardonnet, Y. Le Coq, G. Santarelli, A. Amy-Klein, R. Le Targat, J. Lodewyck, O. Lopez, and P.-E. Pottie, "A clock network for geodesy and fundamental science," Nature Communications **7**, 12443 (2016).
38. P. Delva, A. Hees, and P. Wolf, "Clocks in Space for Tests of Fundamental Physics," Space Sci Rev **212**, 1385–1421 (2017).
39. A. Bassi, L. Cacciapuoti, S. Capozziello, S. Dell'Agnello, E. Diamanti, D. Giulini, L. Iess, P. Jetzer, S. K. Joshi, A. Landragin, C. L. Poncin-Lafitte, E. Rasel, A. Roura, C. Salomon, and H. Ulbricht, "A way forward for fundamental physics in space," npj Microgravity **8**, 1–15 (2022).
40. A. Corney, *Atomic and Laser Spectroscopy* (Oxford University Press, 1987).
41. M. Saffman, "Quantum computing with atomic qubits and Rydberg interactions: progress and challenges," J. Phys. B: At. Mol. Opt. Phys. **49**, 202001 (2016).
42. S. M. Clark, D. Lobser, M. Revelle, C. G. Yale, D. Bossert, A. D. Burch, M. N. Chow, C. W. Hogle, M. Ivory, J. Pehr, B. Salzbrenner, D. Stick, W. Sweatt, J. M. Wilson, E. Winrow, and P. Maunz, "Engineering the Quantum Scientific Computing Open User Testbed (QSCOUT): Design details and user guide," arXiv:2104.00759 [quant-ph] (2021).
43. D. P. DiVincenzo, "The Physical Implementation of Quantum Computation," Fortschritte der Physik **48**, 771–783 (2000).
44. J. I. Cirac and P. Zoller, "Quantum Computations with Cold Trapped Ions," Phys. Rev. Lett. **74**, 4091–4094 (1995).
45. T. Manovitz, Y. Shapira, L. Gazit, N. Akerman, and R. Ozeri, "Trapped-Ion Quantum Computer with Robust Entangling Gates and Quantum Coherent Feedback," PRX Quantum **3**, 010347 (2022).
46. T. M. Graham, Y. Song, J. Scott, C. Poole, L. Phuttitarn, K. Jooya, P. Eichler, X. Jiang, A. Marra, B. Grinkemeyer, M. Kwon, M. Ebert, J. Cherek, M. T. Lichtman, M. Gillette, J. Gilbert, D. Bowman, T. Ballance, C. Campbell, E. D. Dahl, O. Crawford, N.

S. Blunt, B. Rogers, T. Noel, and M. Saffman, "Multi-qubit entanglement and algorithms on a neutral-atom quantum computer," Nature **604**, 457–462 (2022).
47. G. J. Dick, "LOCAL OSCILLATOR INDUCED INSTABILITIES IN TRAPPED ION FREQUENCY STANDARDS," (n.d.).
48. S. Bramhavar, C. Sorace-Agaskar, D. Kharas, W. Loh, R. Maxson, G. N. West, R. Niffenegger, P. W. Juodawlkis, J. Chiaverini, and J. M. Sage, "A visible-light integrated photonic platform for atomic systems," in *Integrated Optics: Devices, Materials, and Technologies XXIII* (International Society for Optics and Photonics, 2019), Vol. 10921, p. 109211D.
49. R. J. Niffenegger, J. Stuart, C. Sorace-Agaskar, D. Kharas, S. Bramhavar, C. D. Bruzewicz, W. Loh, R. T. Maxson, R. McConnell, D. Reens, G. N. West, J. M. Sage, and J. Chiaverini, "Integrated multi-wavelength control of an ion qubit," Nature **586**, 538–542 (2020).
50. A. Mooradian, "Laser Linewidth," Physics Today **38**, 42–48 (1985).
51. S. Gundavarapu, "Sub-Hz Fundamental Linewidth Silicon Nitride Integrated Brillouin Lasers and Their Applications," UC Santa Barbara (2018).
52. G. M. Brodnik, "Precision Optical Phase Synchronization Over Fiber Links Using Spectrally Pure, Chip-," (n.d.).
53. C. Henry, "Theory of the linewidth of semiconductor lasers," IEEE Journal of Quantum Electronics **18**, 259–264 (1982).
54. D. W. Allan, "Time and Frequency (Time-Domain) Characterization, Estimation, and Prediction of Precision Clocks and Oscillators," IEEE Trans. Ultrason., Ferroelect., Freq. Contr. **34**, 647–654 (1987).
55. A. L. Schawlow and C. H. Townes, "Infrared and Optical Masers," Phys. Rev. **112**, 1940–1949 (1958).
56. D. W. Allan, D. A. Howe, F. L. Walls, and D. B. Sullivan, *Characterization of Clocks and Oscillators*, 0 ed. (National Bureau of Standards, 1990), p. NBS TN 1337.
57. G. D. Domenico, S. Schilt, and P. Thomann, "Simple approach to the relation between laser frequency noise and laser line-shape," Appl. Opt., AO **49**, 4801–4807 (2010).
58. J. Hall and M. Zhu, "An Introduction to Phase-Stable Optical Sources," Laser Manipulation of Atoms and Ions (1992).
59. K. Liu, N. Chauhan, J. Wang, A. Isichenko, G. M. Brodnik, P. A. Morton, R. O. Behunin, R. O. Behunin, S. B. Papp, S. B. Papp, and D. J. Blumenthal, "36 Hz integral linewidth laser based on a photonic integrated 4.0 m coil resonator," Optica, OPTICA **9**, 770–775 (2022).
60. A. D. Ludlow, X. Huang, M. Notcutt, T. Zanon-Willette, S. M. Foreman, M. M. Boyd, S. Blatt, and J. Ye, "Compact, thermal-noise-limited optical cavity for diode laser stabilization at 1×10^{-15}," Opt. Lett., OL **32**, 641–643 (2007).
61. T. Kessler, C. Hagemann, C. Grebing, T. Legero, U. Sterr, F. Riehle, M. J. Martin, L. Chen, and J. Ye, "A sub-40-mHz-linewidth laser based on a silicon single-crystal optical cavity," Nature Photon **6**, 687–692 (2012).
62. K. Numata, A. Kemery, and J. Camp, "Thermal-Noise Limit in the Frequency Stabilization of Lasers with Rigid Cavities," Phys. Rev. Lett. **93**, 250602 (2004).
63. M. L. Day, P. J. Low, B. White, R. Islam, and C. Senko, "Limits on atomic qubit control from laser noise," npj Quantum Inf **8**, 1–10 (2022).

64. H. Ball, W. D. Oliver, and M. J. Biercuk, "The role of master clock stability in quantum information processing," npj Quantum Inf **2**, 1–8 (2016).
65. J. M. Pino, J. M. Dreiling, C. Figgatt, J. P. Gaebler, S. A. Moses, M. S. Allman, C. H. Baldwin, M. Foss-Feig, D. Hayes, K. Mayer, C. Ryan-Anderson, and B. Neyenhuis, "Demonstration of the trapped-ion quantum CCD computer architecture," Nature **592**, 209–213 (2021).
66. C. W. Chou, A. L. Collopy, C. Kurz, Y. Lin, M. E. Harding, P. N. Plessow, T. Fortier, S. Diddams, D. Leibfried, and D. R. Leibrandt, "Frequency-comb spectroscopy on pure quantum states of a single molecular ion," Science **367**, 1458–1461 (2020).
67. Y. Lin, D. R. Leibrandt, D. Leibfried, and C. Chou, "Quantum entanglement between an atom and a molecule," Nature **581**, 273–277 (2020).
68. T. A. Huffman, G. M. Brodnik, C. Pinho, S. Gundavarapu, D. Baney, and D. J. Blumenthal, "Integrated Resonators in an Ultralow Loss Si3N4/SiO2Platform for Multifunction Applications," IEEE Journal of Selected Topics in Quantum Electronics **24**, 1–9 (2018).
69. N. Chauhan, D. Bose, M. Puckett, R. Moreira, K. Nelson, and D. J. Blumenthal, "Photonic Integrated Si3N4 Ultra-Large-Area Grating Waveguide MOT Interface for 3D Atomic Clock Laser Cooling," in *Conference on Lasers and Electro-Optics* (OSA, 2019), p. STu4O.3.
70. M. T. Hummon, S. Kang, D. G. Bopp, Q. Li, D. A. Westly, S. Kim, C. Fredrick, S. A. Diddams, K. Srinivasan, V. Aksyuk, and J. E. Kitching, "Photonic chip for laser stabilization to an atomic vapor with 10^{-11} instability," Optica **5**, 443–449 (2018).
71. C. Ropp, C. Ropp, A. Yulaev, A. Yulaev, D. Westly, G. Simelgor, and V. Aksyuk, "Meta-grating outcouplers for optimized beam shaping in the visible," Opt. Express, OE **29**, 14789–14798 (2021).
72. Y. Lin, C. Browning, R. B. Timens, D. H. Geuzebroek, C. G. H. Roeloffzen, D. Geskus, R. M. Oldenbeuving, R. G. Heideman, Y. Fan, K. J. Boller, J. Zhao, and L. P. Barry, "Narrow linewidth hybrid InP-TriPleX photonic integrated tunable laser based on silicon nitride micro-ring resonators," in *Optical Fiber Communication Conference* (OSA, 2018), p. Th2A.14.
73. M. A. Tran, D. Huang, J. Guo, T. Komljenovic, P. A. Morton, and J. E. Bowers, "Ring-Resonator Based Widely-Tunable Narrow-Linewidth Si/InP Integrated Lasers," IEEE Journal of Selected Topics in Quantum Electronics **26**, 1–14 (2020).
74. S. Gundavarapu, G. M. Brodnik, M. Puckett, T. Huffman, D. Bose, R. Behunin, J. Wu, T. Qiu, C. Pinho, N. Chauhan, J. Nohava, P. T. Rakich, K. D. Nelson, M. Salit, and D. J. Blumenthal, "Sub-hertz fundamental linewidth photonic integrated Brillouin laser," Nature Photon **13**, 60–67 (2019).
75. N. Chauhan, J. Wang, D. Bose, R. Moreira, and D. J. Blumenthal, "Ultra-Low Loss 698 nm and 450 nm Silicon Nitride Visible Wavelength Waveguides for Strontium Atomic Clock Applications," in *Conference on Lasers and Electro-Optics (2020), Paper STh1J.2* (Optical Society of America, 2020), p. STh1J.2.
76. A. Raza, S. Clemmen, P. Wuytens, M. de Goede, A. S. K. Tong, N. Le Thomas, C. Liu, J. Suntivich, A. G. Skirtach, S. M. Garcia-Blanco, D. J. Blumenthal, J. S. Wilkinson, and R. Baets, "High index contrast photonic platforms for on-chip Raman spectroscopy," Opt. Express **27**, 23067 (2019).

77. E. S. Hosseini, S. Yegnanarayanan, A. H. Atabaki, M. Soltani, and A. Adibi, "High Quality Planar Silicon Nitride Microdisk Resonators for Integrated Photonics in the VisibleWavelength Range," Opt. Express, OE **17**, 14543–14551 (2009).
78. M. Soltani, R. Soref, T. Palacios, and D. Englund, "AlGaN/AlN integrated photonics platform for the ultraviolet and visible spectral range," Opt. Express, OE **24**, 25415–25423 (2016).
79. Y. C. Cheng and W. D. Festwood, "Losses in tantalum pentoxide waveguides," JEM **3**, 37–50 (1974).
80. R. Fan, C.-L. Wu, Y.-Y. Lin, C.-Y. Liu, P.-S. Hwang, C.-W. Liu, J. Qiao, M.-H. Shih, Y.-J. Hung, Y.-J. Chiu, A.-K. Chu, and C.-K. Lee, "Visible to near-infrared octave spanning supercontinuum generation in tantalum pentoxide (Ta_2O_5) air-cladding waveguide," Opt. Lett., OL **44**, 1512–1515 (2019).
81. M. Belt, M. L. Davenport, J. E. Bowers, and D. J. Blumenthal, "Ultra-low-loss Ta_2O_5-core/SiO_2-clad planar waveguides on Si substrates," Optica, OPTICA **4**, 532–536 (2017).
82. A. Boes, B. Corcoran, L. Chang, J. Bowers, and A. Mitchell, "Status and Potential of Lithium Niobate on Insulator (LNOI) for Photonic Integrated Circuits," Laser & Photonics Reviews **12**, 1700256 (2018).
83. C. C. Evans, C. Liu, and J. Suntivich, "Low-loss titanium dioxide waveguides and resonators using a dielectric lift-off fabrication process," Opt. Express, OE **23**, 11160–11169 (2015).
84. D. G. Rabus and C. Sada, "Ring Resonators: Theory and Modeling," in *Integrated Ring Resonators: A Compendium*, D. G. Rabus and C. Sada, eds., Springer Series in Optical Sciences (Springer International Publishing, 2020), pp. 3–46.
85. R. Kitamura, L. Pilon, and M. Jonasz, "Optical constants of silica glass from extreme ultraviolet to far infrared at near room temperature," Appl. Opt. **46**, 8118 (2007).
86. J. D. Traylor Kruschwitz and W. T. Pawlewicz, "Optical and durability properties of infrared transmitting thin films," Appl. Opt. **36**, 2157 (1997).
87. J. Bauters, M. R. Heck, D. D. John, J. S. Barton, C. M. Bruinink, A. Leinse, R. Heideman, D. J. Blumenthal, and J. Bowers, "A Comparison of Approaches for Ultra-Low-Loss Waveguides," in *Optical Fiber Communication Conference* (OSA, 2012), p. OTu1I.3.
88. T. A. Huffman, G. M. Brodnik, C. Pinho, S. Gundavarapu, D. Baney, and D. J. Blumenthal, "Integrated Resonators in an Ultralow Loss Si3N4/SiO2 Platform for Multifunction Applications," IEEE Journal of Selected Topics in Quantum Electronics **24**, 1–9 (2018).
89. J. F. Bauters, M. J. R. Heck, D. Dai, J. S. Barton, D. J. Blumenthal, and J. E. Bowers, "Ultralow-Loss Planar $\hboxSi_3\hboxN_4$ Waveguide Polarizers," IEEE Photonics Journal **5**, 6600207–6600207 (2013).
90. M. Piels, J. F. Bauters, M. L. Davenport, M. J. R. Heck, and J. E. Bowers, "Low-Loss Silicon Nitride AWG Demultiplexer Heterogeneously Integrated With Hybrid III–V/Silicon Photodetectors," Journal of Lightwave Technology **32**, 817–823 (2014).
91. N. T. Otterstrom, S. Gertler, Y. Zhou, E. A. Kittlaus, R. O. Behunin, M. Gehl, A. L. Starbuck, C. M. Dallo, A. T. Pomerene, D. C. Trotter, A. L. Lentine, and P. T. Rakich, "Backscatter-Immune Injection-Locked Brillouin Laser in Silicon," Phys. Rev. Applied **14**, 044042 (2020).

92. T. Dai, A. Shen, G. Wang, Y. Wang, Y. Li, X. Jiang, and J. Yang, "Bandwidth and wavelength tunable optical passband filter based on silicon multiple microring resonators," Opt. Lett., OL **41**, 4807–4810 (2016).
93. W. D. Sacher and J. K. S. Poon, "Characteristics of Microring Resonators With Waveguide-Resonator Coupling Modulation," Journal of Lightwave Technology **27**, 3800–3811 (2009).
94. L. Chen, N. Sherwood-Droz, and M. Lipson, "Compact bandwidth-tunable microring resonators," Opt. Lett., OL **32**, 3361–3363 (2007).
95. H. Shoman, H. Jayatilleka, N. A. F. Jaeger, S. Shekhar, and L. Chrostowski, "Measuring on-chip waveguide losses using a single, two-point coupled microring resonator," Opt. Express, OE **28**, 10225–10238 (2020).
96. W. Jiang, Y. Zhang, Y. Guo, F. Zhu, and G. Yi, "Switchable and Flexible Comb Filter/Interleaver Based on Ring-Resonators With Tunable Couplers," IEEE Photonics Technology Letters **33**, 607–610 (2021).
97. B. Little, S. Chu, W. Chen, J. Hryniewicz, D. Gill, O. King, F. Johnson, R. Davidson, K. Donovan, W. Chen, and S. Grubb, "Tunable bandwidth microring resonator filters," in *2008 34th European Conference on Optical Communication* (2008), pp. 1–2.
98. A. Isichenko, N. Chauhan, K. Liu, M. W. Harrington, and D. J. Blumenthal, "Chip-Scale, Sub-Hz Fundamental Sub-kHz Integral Linewidth 780 nm Laser through Self-Injection-Locking a Fabry-Perot laser to an Ultra-High Q Integrated Resonator," (2023).
99. C. L. Degen, F. Reinhard, and P. Cappellaro, "Quantum sensing," Rev. Mod. Phys. **89**, 035002 (2017).
100. H. Fan, S. Kumar, J. Sedlacek, H. Kübler, S. Karimkashi, and J. P. Shaffer, "Atom based RF electric field sensing," J. Phys. B: At. Mol. Opt. Phys. **48**, 202001 (2015).
101. A. W. Young, W. J. Eckner, W. R. Milner, D. Kedar, M. A. Norcia, E. Oelker, N. Schine, J. Ye, and A. M. Kaufman, "Half-minute-scale atomic coherence and high relative stability in a tweezer clock," Nature **588**, 408–413 (2020).
102. A. Cygan, D. Lisak, P. Morzyński, M. Bober, M. Zawada, E. Pazderski, and R. Ciuryło, "Cavity mode-width spectroscopy with widely tunable ultra narrow laser," Opt. Express, OE **21**, 29744–29754 (2013).
103. A. Jadbabaie, N. H. Pilgram, J. Klos, S. Kotochigova, and N. R. Hutzler, "Enhanced molecular yield from a cryogenic buffer gas beam source via excited state chemistry," New J. Phys. (2020).
104. J. L. Bohn, A. M. Rey, and J. Ye, "Cold molecules: Progress in quantum engineering of chemistry and quantum matter," Science **357**, 1002–1010 (2017).
105. R. W. Fox, C. W. Oates, and L. W. Hollberg, "1. Stabilizing diode lasers to high-finesse cavities," in *Experimental Methods in the Physical Sciences*, R. D. van Zee and J. P. Looney, eds., Cavity-Enhanced Spectroscopies (Academic Press, 2003), Vol. 40, pp. 1–46.
106. T. L. Nicholson, S. L. Campbell, R. B. Hutson, G. E. Marti, B. J. Bloom, R. L. McNally, W. Zhang, M. D. Barrett, M. S. Safronova, G. F. Strouse, W. L. Tew, and J. Ye, "Systematic evaluation of an atomic clock at 2 × 10−18 total uncertainty," Nat Commun **6**, 6896 (2015).
107. D. J. Blumenthal, R. Heideman, D. Geuzebroek, A. Leinse, and C. Roeloffzen, "Silicon Nitride in Silicon Photonics," Proceedings of the IEEE **106**, 2209–2231 (2018).

108. A. Y. Liu and J. Bowers, "Photonic Integration With Epitaxial III–V on Silicon," IEEE Journal of Selected Topics in Quantum Electronics **24**, 1–12 (2018).
109. I. Bloch, "Quantum coherence and entanglement with ultracold atoms in optical lattices," Nature **453**, 1016–1022 (2008).
110. H. Levine, A. Keesling, A. Omran, H. Bernien, S. Schwartz, A. S. Zibrov, M. Endres, M. Greiner, V. Vuletić, and M. D. Lukin, "High-Fidelity Control and Entanglement of Rydberg-Atom Qubits," Phys. Rev. Lett. **121**, 123603 (2018).
111. N. R. Hutzler, "Polyatomic molecules as quantum sensors for fundamental physics," Quantum Sci. Technol. **5**, 044011 (2020).
112. T. Krawinkel, "Improved GNSS navigation with chip-scale atomic clocks," Veröffentlichungen der DGK, Reihe C, Dissertationen;823 (2018).
113. S. Ospelkaus, K.-K. Ni, D. Wang, M. H. G. de Miranda, B. Neyenhuis, G. Quéméner, P. S. Julienne, J. L. Bohn, D. S. Jin, and J. Ye, "Quantum-State Controlled Chemical Reactions of Ultracold Potassium-Rubidium Molecules," Science **327**, 853–857 (2010).
114. E. National Academies of Sciences, *Manipulating Quantum Systems: An Assessment of Atomic, Molecular, and Optical Physics in the United States* (2019).
115. P. Yu and N. R. Hutzler, "Probing Fundamental Symmetries of Deformed Nuclei in Symmetric Top Molecules," Phys. Rev. Lett. **126**, 023003 (2021).
116. M. Verma, A. M. Jayich, and A. C. Vutha, "Electron Electric Dipole Moment Searches Using Clock Transitions in Ultracold Molecules," Phys. Rev. Lett. **125**, 153201 (2020).
117. L. Anderegg, L. W. Cheuk, Y. Bao, S. Burchesky, W. Ketterle, K.-K. Ni, and J. M. Doyle, "An optical tweezer array of ultracold molecules," Science **365**, 1156–1158 (2019).
118. D. Mitra, N. B. Vilas, C. Hallas, L. Anderegg, B. L. Augenbraun, L. Baum, C. Miller, S. Raval, and J. M. Doyle, "Direct laser cooling of a symmetric top molecule," Science **369**, 1366–1369 (2020).
119. R. I. Woodward, E. J. R. Kelleher, S. V. Popov, and J. R. Taylor, "Stimulated Brillouin scattering of visible light in small-core photonic crystal fibers," Opt. Lett., OL **39**, 2330–2333 (2014).
120. D. R. Ponikvar and S. Ezekiel, "Stabilized single-frequency stimulated Brillouin fiber ring laser," Opt. Lett., OL **6**, 398–400 (1981).
121. S. P. Smith, F. Zarinetchi, and S. Ezekiel, "Narrow-linewidth stimulated Brillouin fiber laser and applications," Opt. Lett., OL **16**, 393–395 (1991).
122. F. Zarinetchi, S. P. Smith, and S. Ezekiel, "Stimulated Brillouin fiber-optic laser gyroscope," Opt. Lett., OL **16**, 229–231 (1991).
123. L. F. Stokes, M. Chodorow, and H. J. Shaw, "All-fiber stimulated Brillouin ring laser with submilliwatt pump threshold," Opt. Lett., OL **7**, 509–511 (1982).
124. Z. Bai, R. J. Williams, O. Kitzler, S. Sarang, D. J. Spence, Y. Wang, Z. Lu, and R. P. Mildren, "Diamond Brillouin laser in the visible," APL Photonics **5**, 031301 (2020).
125. S. Jiang, C. Guo, K. Che, Z. Luo, T. Du, H. Fu, H. Xu, and Z. Cai, "Visible Raman and Brillouin lasers from a microresonator/ZBLAN-fiber hybrid system," Photon. Res., PRJ **7**, 566–572 (2019).
126. W. Loh, J. Stuart, D. Reens, C. D. Bruzewicz, D. Braje, J. Chiaverini, P. W. Juodawlkis, J. M. Sage, and R. McConnell, "Operation of an optical atomic clock with a Brillouin laser subsystem," Nature **588**, 244–249 (2020).

127. P. T. Rakich, C. Reinke, R. Camacho, P. Davids, and Z. Wang, "Giant Enhancement of Stimulated Brillouin Scattering in the Subwavelength Limit," Phys. Rev. X **2**, 011008 (2012).
128. R. Pant, C. G. Poulton, D.-Y. Choi, H. Mcfarlane, S. Hile, E. Li, L. Thevenaz, B. Luther-Davies, S. J. Madden, and B. J. Eggleton, "On-chip stimulated Brillouin scattering," Opt. Express, OE **19**, 8285–8290 (2011).
129. C. G. Poulton, R. Pant, and B. J. Eggleton, "Acoustic confinement and stimulated Brillouin scattering in integrated optical waveguides," J. Opt. Soc. Am. B, JOSAB **30**, 2657–2664 (2013).
130. J. Li, H. Lee, T. Chen, and K. J. Vahala, "Characterization of a high coherence, Brillouin microcavity laser on silicon," Opt. Express, OE **20**, 20170–20180 (2012).
131. K. Y. Yang, D. Y. Oh, S. H. Lee, Q.-F. Yang, X. Yi, B. Shen, H. Wang, and K. Vahala, "Bridging ultrahigh- Q devices and photonic circuits," Nature Photonics **12**, 297–302 (2018).
132. B. J. Eggleton, C. G. Poulton, P. T. Rakich, M. J. Steel, and G. Bahl, "Brillouin integrated photonics," Nature Photonics **13**, 664–677 (2019).
133. F. Gyger, J. Liu, F. Yang, J. He, A. S. Raja, R. N. Wang, S. A. Bhave, T. J. Kippenberg, and L. Thévenaz, "Observation of Stimulated Brillouin Scattering in Silicon Nitride Integrated Waveguides," Phys. Rev. Lett. **124**, 013902 (2020).
134. K. Liu, M. W. Harrington, K. D. Nelson, R. O. Behunin, S. B. Papp, and D. J. Blumenthal, "Photonic integrated cascade-inhibited Brillouin laser with sub-100-mHz fundamental linewidth," in *Conference on Lasers and Electro-Optics* (Optica Publishing Group, 2022), p. SF2K.1.
135. G. M. Brodnik, M. W. Harrington, D. Bose, A. M. Netherton, W. Zhang, L. Stern, P. A. Morton, J. E. Bowers, S. B. Papp, S. B. Papp, and D. J. Blumenthal, "Chip-Scale, Optical-Frequency-Stabilized PLL for DSP-Free, Low-Power Coherent QAM in the DCI," in *Optical Fiber Communication Conference (OFC) 2020 (2020), Paper M3A.6* (Optical Society of America, 2020), p. M3A.6.
136. D. J. Blumenthal, I. Kabakova, P. T. Rakich, and K. Vahala, "Integrated Brillouin lasers and their applications," in *Semiconductors and Semimetals* (Elsevier, 2022), Vol. 110, pp. 107–180.
137. N. Akerman, N. Navon, S. Kotler, Y. Glickman, and R. Ozeri, "Universal gate-set for trapped-ion qubits using a narrow linewidth diode laser," New J. Phys. **17**, 113060 (2015).
138. N. Chauhan, A. Isichenko, K. Liu, and D. J. Blumenthal, "Visible 780 nm SBS laser with mW level threshold in an ultra-high 145 million Q integrated waveguide resonator," in *CLEO 2023 (2023), Paper SF1K.6* (Optica Publishing Group, 2023), p. SF1K.6.
139. R. O. Behunin, N. T. Otterstrom, P. T. Rakich, S. Gundavarapu, and D. J. Blumenthal, "Fundamental noise dynamics in cascaded-order Brillouin lasers," Phys. Rev. A **98**, 023832 (2018).
140. V. G. Kozlov, V. Bulović, P. E. Burrows, and S. R. Forrest, "Laser action in organic semiconductor waveguide and double-heterostructure devices," Nature **389**, 362–364 (1997).

141. B. S. Lee, M. Zhang, F. A. S. Barbosa, S. A. Miller, A. Mohanty, R. St-Gelais, and M. Lipson, "On-chip thermo-optic tuning of suspended microresonators," Opt. Express, OE **25**, 12109–12120 (2017).
142. J. Wang, K. Liu, Q. Zhao, A. Isichenko, R. Q. Rudy, and D. J. Blumenthal, "Fully symmetric controllable integrated three-resonator photonic molecule," arXiv:2105.10815 [physics] (2021).
143. P. A. Morton and M. J. Morton, "High-Power, Ultra-Low Noise Hybrid Lasers for Microwave Photonics and Optical Sensing," Journal of Lightwave Technology **36**, 5048–5057 (2018).
144. J. Li, H. Lee, and K. J. Vahala, "Microwave synthesizer using an on-chip Brillouin oscillator," Nat Commun **4**, 2097 (2013).
145. G. Zhang, J. Y. Haw, H. Cai, F. Xu, S. M. Assad, J. F. Fitzsimons, X. Zhou, Y. Zhang, S. Yu, J. Wu, W. Ser, L. C. Kwek, and A. Q. Liu, "An integrated silicon photonic chip platform for continuous-variable quantum key distribution," Nat. Photonics **13**, 839–842 (2019).
146. A. Orieux and E. Diamanti, "Recent advances on integrated quantum communications," J. Opt. **18**, 083002 (2016).
147. N. Gisin and R. Thew, "Quantum communication," Nature Photonics **1**, 165–171 (2007).
148. D. J. Blumenthal, H. Ballani, R. O. Behunin, J. E. Bowers, P. Costa, D. Lenoski, Paul. A. Morton, S. B. Papp, and P. T. Rakich, "Frequency-Stabilized Links for Coherent WDM Fiber Interconnects in the Datacenter," Journal of Lightwave Technology **38**, 3376–3386 (2020).
149. R. W. P. Drever, J. L. Hall, F. V. Kowalski, J. Hough, G. M. Ford, A. J. Munley, and H. Ward, "Laser phase and frequency stabilization using an optical resonator," Appl. Phys. B **31**, 97–105 (1983).
150. M. Notcutt, L.-S. Ma, A. D. Ludlow, S. M. Foreman, J. Ye, and J. L. Hall, "Contribution of thermal noise to frequency stability of rigid optical cavity via Hertz-linewidth lasers," Phys. Rev. A **73**, 031804 (2006).
151. J. Alnis, A. Schliesser, C. Y. Wang, J. Hofer, T. J. Kippenberg, and T. W. Hänsch, "Thermal-noise-limited crystalline whispering-gallery-mode resonator for laser stabilization," Phys. Rev. A **84**, 011804 (2011).
152. W. Liang, V. S. Ilchenko, D. Eliyahu, A. A. Savchenkov, A. B. Matsko, D. Seidel, and L. Maleki, "Ultralow noise miniature external cavity semiconductor laser," Nat Commun **6**, 7371 (2015).
153. W. Zhang, L. Stern, D. Carlson, D. Bopp, Z. Newman, S. Kang, J. Kitching, and S. B. Papp, "Ultranarrow Linewidth Photonic-Atomic Laser," Laser & Photonics Reviews **14**, 1900293 (2020).
154. J. Lim, A. A. Savchenkov, E. Dale, W. Liang, D. Eliyahu, V. Ilchenko, A. B. Matsko, L. Maleki, and C. W. Wong, "Chasing the thermodynamical noise limit in whispering-gallery-mode resonators for ultrastable laser frequency stabilization," Nat Commun **8**, 8 (2017).
155. K. Liu, J. H. Dallyn, G. M. Brodnik, A. Isichenko, M. W. Harrington, N. Chauhan, D. Bose, P. A. Morton, S. B. Papp, R. O. Behunin, and D. J. Blumenthal, "Photonic circuits for laser stabilization with integrated ultra-high Q and Brillouin laser resonators," APL Photonics **7**, 096104 (2022).

156. H. Lee, M.-G. Suh, T. Chen, J. Li, S. A. Diddams, and K. J. Vahala, "Spiral resonators for on-chip laser frequency stabilization," Nature Communications **4**, 2468 (2013).
157. C. A. McLemore, N. Jin, M. L. Kelleher, J. P. Hendrie, D. Mason, Y. Luo, D. Lee, P. Rakich, S. A. Diddams, and F. Quinlan, "Miniaturizing Ultrastable Electromagnetic Oscillators: Sub-${10}^{\ensuremath{-}14}$ Frequency Instability from a Centimeter-Scale Fabry-Perot Cavity," Phys. Rev. Applied **18**, 054054 (2022).
158. N. Jin, C. A. McLemore, D. Mason, J. P. Hendrie, Y. Luo, M. L. Kelleher, P. Kharel, F. Quinlan, S. A. Diddams, and P. T. Rakich, "Micro-fabricated mirrors with finesse exceeding one million," Optica, OPTICA **9**, 965–970 (2022).
159. N. Chauhan, K. Liu, A. Isichenko, J. Wang, H. Timmers, and D. J. Blumenthal, "Integrated 3.0 meter coil resonator for λ = 674 nm laser stabilization," in *Frontiers in Optics + Laser Science 2022 (FIO, LS) (2022), Paper FM1E.1* (Optica Publishing Group, 2022), p. FM1E.1.
160. P. Horak and W. H. Loh, "On the delayed self-heterodyne interferometric technique for determining the linewidth of fiber lasers," Opt. Express, OE **14**, 3923–3928 (2006).
161. T. P. Harty, D. T. C. Allcock, C. J. Ballance, L. Guidoni, H. A. Janacek, N. M. Linke, D. N. Stacey, and D. M. Lucas, "High-Fidelity Preparation, Gates, Memory, and Readout of a Trapped-Ion Quantum Bit," Phys. Rev. Lett. **113**, 220501 (2014).
162. S. A. Moses, C. H. Baldwin, M. S. Allman, R. Ancona, L. Ascarrunz, C. Barnes, J. Bartolotta, B. Bjork, P. Blanchard, M. Bohn, J. G. Bohnet, N. C. Brown, N. Q. Burdick, W. C. Burton, S. L. Campbell, J. P. Campora III, C. Carron, J. Chambers, J. W. Chen, Y. H. Chen, A. Chernoguzov, E. Chertkov, J. Colina, M. DeCross, J. M. Dreiling, C. T. Ertsgaard, J. Esposito, B. Estey, M. Fabrikant, C. Figgatt, C. Foltz, M. Foss-Feig, D. Francois, J. P. Gaebler, T. M. Gatterman, C. N. Gilbreth, J. Giles, E. Glynn, A. Hall, A. M. Hankin, A. Hansen, D. Hayes, B. Higashi, I. M. Hoffman, B. Horning, J. J. Hout, R. Jacobs, J. Johansen, T. Klein, P. Lauria, P. Lee, D. Liefer, S. T. Lu, D. Lucchetti, A. Malm, M. Matheny, B. Mathewson, K. Mayer, D. B. Miller, M. Mills, B. Neyenhuis, L. Nugent, S. Olson, J. Parks, G. N. Price, Z. Price, M. Pugh, A. Ransford, A. P. Reed, C. Roman, M. Rowe, C. Ryan-Anderson, S. Sanders, J. Sedlacek, P. Shevchuk, P. Siegfried, T. Skripka, B. Spaun, R. T. Sprenkle, R. P. Stutz, M. Swallows, R. I. Tobey, A. Tran, T. Tran, E. Vogt, C. Volin, J. Walker, A. M. Zolot, and J. M. Pino, "A Race Track Trapped-Ion Quantum Processor," (2023).
163. H. Wenzel, B. Arar, A. Maaßdorf, J. Fricke, D. Martin, C. Zink, M. Schiemangk, A. Wicht, M. Weyers, and A. Knigge, "Distributed Bragg reflector lasers emitting between 696 and 712 nm," Electronics Letters **58**, 908–910 (2022).
164. B. Desiatov, A. Shams-Ansari, M. Zhang, C. Wang, and M. Lončar, "Ultra-low-loss integrated visible photonics using thin-film lithium niobate," Optica, OPTICA **6**, 380–384 (2019).
165. A. Ludlow, "The Strontium Optical Lattice Clock: Optical Spectroscopy with Sub-Hertz Accuracy," **40**, OPC.10 (2009).
166. Q. Zhao, M. W. Harrington, A. Isichenko, K. Liu, R. O. Behunin, R. O. Behunin, S. B. Papp, P. T. Rakich, C. W. Hoyt, C. Fertig, and D. J. Blumenthal, "Integrated reference cavity with dual-mode optical thermometry for frequency correction," Optica, OPTICA **8**, 1481–1487 (2021).
167. C. S. Adams and E. Riis, "Laser cooling and trapping of neutral atoms," Progress in Quantum Electronics **21**, 1–79 (1997).

168. P. D. Lett, P. S. Julienne, and W. D. Phillips, "Photoassociative Spectroscopy of Laser-Cooled Atoms," Annual Review of Physical Chemistry **46**, 423–452 (1995).
169. W. Li, I. Mourachko, M. W. Noel, and T. F. Gallagher, "Millimeter-wave spectroscopy of cold Rb Rydberg atoms in a magneto-optical trap: Quantum defects of the ns, np, and nd series," Phys. Rev. A **67**, 052502 (2003).
170. C. N. Cohen-Tannoudji, "Manipulating atoms with photons," Rev. Mod. Phys. **70**, 13 (1998).
171. H. J. Metcalf and P. van der Straten, "Optical Traps for Neutral Atoms," in *Laser Cooling and Trapping*, H. J. Metcalf and P. van der Straten, eds., Graduate Texts in Contemporary Physics (Springer New York, 1999), pp. 149–164.
172. S. Chu, "The manipulation of neutral particles," Rev. Mod. Phys. **70**, 22 (1998).
173. K. I. Lee, J. A. Kim, H. R. Noh, and W. Jhe, "Single-beam atom trap in a pyramidal and conical hollow mirror," Opt. Lett. **21**, 1177 (1996).
174. J. M. Kohel, J. Ramirez-Serrano, R. J. Thompson, L. Maleki, J. L. Bliss, and K. G. Libbrecht, "Generation of an intense cold-atom beam from a pyramidal magneto-optical trap: experiment and simulation," J. Opt. Soc. Am. B, JOSAB **20**, 1161–1168 (2003).
175. S. Kim, D. A. Westly, B. J. Roxworthy, Q. Li, A. Yulaev, K. Srinivasan, and V. A. Aksyuk, "Photonic waveguide mode to free-space Gaussian beam extreme mode converter," Light Sci Appl **7**, 72 (2018).
176. M. T. Hummon, S. Kang, D. G. Bopp, Q. Li, D. A. Westly, S. Kim, C. Fredrick, S. A. Diddams, K. Srinivasan, V. Aksyuk, and J. E. Kitching, "Photonic chip for laser stabilization to an atomic vapor with 10^{-11} instability," Optica **5**, 443–449 (2018).
177. Z. L. Newman, V. Maurice, T. Drake, J. R. Stone, T. C. Briles, D. T. Spencer, C. Fredrick, Q. Li, D. Westly, B. R. Ilic, B. Shen, M.-G. Suh, K. Y. Yang, C. Johnson, D. M. S. Johnson, L. Hollberg, K. J. Vahala, K. Srinivasan, S. A. Diddams, J. Kitching, S. B. Papp, and M. T. Hummon, "Architecture for the photonic integration of an optical atomic clock," Optica, OPTICA **6**, 680–685 (2019).
178. S. Jammi, A. R. Ferdinand, W. Zhu, G. Spektor, Z. Newman, J. Song, O. Koksal, Z. Wang, W. Lunden, D. Sheredy, P. Patel, A. Rakholia, T. C. Briles, M. Boyd, A. Agrawal, and S. Papp, "Alignment-free Sr MOT with integrated metasurfaces for a compact Sr optical clock," in *CLEO 2023 (2023), Paper SW4O.2* (Optica Publishing Group, 2023), p. SW4O.2.
179. L. Chen, C.-J. Huang, X.-B. Xu, Z.-T. Lu, Z.-B. Wang, G.-J. Chen, J.-Z. Zhang, H. X. Tang, C.-H. Dong, W. Liu, G.-Y. Xiang, G.-C. Guo, and C.-L. Zou, "Planar Integrated Magneto Optical Trap," arXiv:2107.07367 [physics] (2021).
180. J. P. McGilligan, P. F. Griffin, R. Elvin, S. J. Ingleby, E. Riis, and A. S. Arnold, "Grating chips for quantum technologies," Sci Rep **7**, 384 (2017).
181. M. W. Puckett and N. A. Krueger, "Broadband, ultrahigh efficiency fiber-to-chip coupling via multilayer nanophotonics," Appl. Opt., AO **60**, 4340–4344 (2021).
182. A. Isichenko, N. Chauhan, K. Liu, M. W. Harrington, and D. J. Blumenthal, "Chip-Scale, Sub-Hz Fundamental Sub-kHz Integral Linewidth 780 nm Laser through Self-Injection-Locking a Fabry-Pérot laser to an Ultra-High Q Integrated Resonator," (n.d.).
183. A. M. Bishop and A. L. Gaeta, "Narrow linewidth semiconductor lasers based on nonlinear self-injection locking," (2023).

184. C. Xiang, W. Jin, O. Terra, B. Dong, H. Wang, L. Wu, J. Guo, T. J. Morin, E. Hughes, J. Peters, Q.-X. Ji, A. Feshali, M. Paniccia, K. J. Vahala, and J. E. Bowers, "3D integration enables ultralow-noise isolator-free lasers in silicon photonics," Nature **620**, 78–85 (2023).